

BERND RIEDMULLER

Activation barriers in gas-surface reactions

Activation barriers in gas—surface reactions

PROEFSCHRIFT

TER VERKRIJGING VAN

DE GRAAD VAN DOCTOR AAN DE UNIVERSITEIT LEIDEN,

OP GEZAG VAN DE RECTOR MAGNIFICUS DR. D.D. BREIMER,

HOOGLERAAR IN DE FACULTEIT DER WISKUNDE EN

NATUURWETENSCHAPPEN EN DIE DER GENEESKUNDE,

VOLGENS BESLUIT VAN HET COLLEGE VOOR PROMOTIES

TE VERDEDIGEN OP DONDERDAG 22 MAART 2001

TE KLOKKE 14.15 UUR

DOOR

BERND RIEDMÜLLER

GEBOREN TE LAUPHEIM IN 1971

Promotiecommissie

1e promotor: Prof. Dr. A. W. Kleyn
2e promotor: Prof. Dr. R. A. van Santen
referent: Dr. B. E. Nieuwenhuys
Overige leden: Prof. Dr. J. W. M. Frenken

Prof. Dr H. J. M. de Groot

Dr. G. J. Kroes

Dr. H. P. C. E. Kuipers

Omslag: Illya Cerjak

The work described in this thesis was performed at the FOM Institute for Atomic and Molecular Physics, Kruislaan 407, 1098 SJ Amsterdam and was made possible by financial support from the *Nederlandse Organisatie voor Wetenschappelijk Onderzoek* NWO (Dutch Organization for Scientific Research).

'the activity of intelligence could be without will' ${\it `PHILOSOPHY\,OF\,MIND'} \\ G.W.F.~HEGEL$

This thesis is based on the following papers:

Chapter 2 B. Riedmüller, and I. M. Ciobîcă, D. C. Papageorgopoulos, F. Frechard, B. Berenbak, A. W. Kleyn and R. A. van Santen,
CO adsorption on H saturated Ru(0001), submitted to Journal of Chemical Physics.

Chapter 3 B. Riedmüller, I. M. Ciobîcă, D. C. Papageorgopoulos, B. Berenbak, R. A. van Santen, A. W. Kleyn,

The dynamic interaction of CO with Ru(0001) in the presence of adsorbed CO and hydrogen, Surf. Sci. **465**, 347 (2000)

Chapter 4 B. Riedmüller, D. C. Papageorgopoulos, B. Berenbak, R. A. van Santen, A. W. Kleyn,

'Magic' size island formation of CO coadsorbed with H on Ru(0001), in preparation

Chapter 5 B. Riedmüller and A.W. Kleyn, *A compact molecular beam line*, in preparation

Chapter 6 B. Riedmüller, A. T. Gee, C. Mormiche, A.W. Kleyn and B. E. Hayden, *Dissociative adsorption of methane on Pt(533)*, in preparation

Contents

1	Intr	oduction	1
	1.1	The importance of heterogeneous catalysis	1
	1.2	Mechanistic aspects of gas–surface reactions	2
	1.3	Molecular beams:	
		An appropriate experimental tool	8
	1.4	Critical remarks on the surface science approach	11
	1.5	This thesis	12
2	co	adsorption on H saturated Ru(0001)	15
	2.1	Introduction	16
	2.2	Methods	17
		2.2.1 Theoretical method and surface model	17
		2.2.2 Experiments	18
	2.3	Results and discussion	18
		2.3.1 Calculations	18
		2.3.2 Experiments	25
	2.4	Conclusion	27
3	The	dynamic interaction of CO with Ru(0001) in the presence of adsorbed CO and	
	Н		29
	3.1	Introduction	30
	3.2	Experimental	32
	3.3	Results and Discussion	33
		3.3.1 Initial sticking coefficient for CO on Ru(0001)	33
		3.3.2 CO scattering from Ru(0001)	35
		3.3.3 CO scattering from a completely CO–covered surface	39
		3.3.4 CO and argon scattering from $Ru(0001)(1\times1)H$	40
	3.4	Conclusion	45
4	'Ma	gic' island formation of CO coadsorbed with H on Ru(0001)	47
	4.1	Introduction	
	4.2	Experimental	
	4.3	Results and Discussion	
		4 3 1 Thermal desorption	

		4.3.2 Thermal energy He–atom scattering	54
	4.4	Conclusion and summary	63
5	A co	npact molecular beam line	65
	5.1	Introduction	66
	5.2	Design criteria	67
	5.3	Implementation and Performance	70
		5.3.1 Molecular beam line	70
		5.3.2 Beam detection and TOF–techniques	77
		5.3.3 Thermal desorption facilities	78
		5.3.4 Performance test of K&W and TDS–facilities	81
		5.3.5 TOF calibration and beam energies	84
	5.4	Conclusion and summary	87
6	Dicc	ciative adsorption of methane on Pt(533)	89
U	D199	clative adjoint of memane on re(200)	0,
U	6.1	Introduction	90
U		•	
U	6.1	Introduction	90
U	6.1 6.2	Introduction	90 91 93
	6.1 6.2 6.3	Introduction	90 91 93
Su	6.1 6.2 6.3 6.4 mma	Introduction	90 91 93 100
Su Zu	6.1 6.2 6.3 6.4 mma	Introduction	90 91 93 100 111

Chapter 1

Introduction

1.1 The importance of heterogeneous catalysis

The functioning of industrial nations is based on a constantly growing economy because national prosperity is essential for stable democracies. This economic growth has resulted in a constant increase in energy consumption over the last century. The main energy resource still consists of crude oil which is converted into gasoline or fuel oil. The catalytic conversion and modification of crude oil is essential for both providing an environmentally reconcilable consumption of this resource and for the performance of combustion engines or furnaces. Practically all these processes involve heterogeneous catalysis. For the sake of a clean combustion, crude oil is separated into fractions by distillation which are subsequently processed and purified. For example, the purification processes remove undesired content like sulfur and nitrogen because their oxidation products emerging during combustion lead to polluting products. For instance, NO $_{x}$ contributes to ozone layer depletion and SO $_{x}$ causes acid rain. Nitrogen and sulfur are chemically extracted by hydrotreatment steps which are performed over a heterogeneous catalyst.

The primary objective of these catalysts is to enhance the reaction rate and to yield the desired products at a high selectivity. To do so, the catalyst has to reduce the activation energy of the rate limiting step. Consequently, reactions that would usually take an unimaginably long time, can proceed on a short time scale. By this means, the dilemma of disadvantageous thermodynamic conditions resulting from kinetic considerations can be circumvented. For instance, if an exothermic reaction has a high activation barrier, one is tempted to conduct the reaction at high temperatures because otherwise the reaction rate will be negligible. However, at high temperatures thermodynamics will favor the decay of the product which leads to a very low yield. In this case, the use of an appropriate catalyst is vital. Furthermore, the mismatch between reasonable rate and high yield also affects the product distribution. Especially if processes are complex and large molecules are involved, many side reactions occur leading to undesired products. 'The higher the reaction temperature the lower the selectivity' can be considered as a rule-of-thumb. Therefore, to achieve a high selectivity a catalyst should only lower the activation barrier of the reaction leading to the desired product.

The choice for a certain catalyst for a catalytic conversion is not only determined by the reaction itself but also by the industrial process. For example, heterogeneous catalysts are used

2 Chapter one

for the production of bulk chemicals because the solid catalyst materials are unmixable with products or educts. This facilitates the separation of products and catalyst material, especially if gaseous products and/or educts are involved. Consequently, the reaction can be performed under continuous flow conditions which permits the scaling up of production processes to achieve high rates. This advantage of heterogeneous catalysis is of exceptional importance because it allows the production of gasoline, fuel oil and other bulk chemicals on a large scale which is essential to provide sufficient bulk chemicals to satisfy the vast demands of the world market. Note that the world total oil consumption in the years 2000 to 2005 was estimated to increase from 76.8 to 84.7 million barrels per day [1]!

Refining crude oil is just one example of a large scale catalytic process, others include the synthesis of ammonia, methanol, polyethylene, polypropylene, styrene, ethene oxide and many more. Most of these bulk chemicals are utilized as intermediates for other chemical processes. For example, the oxidation of ammonium is used to produce nitrates which form the basis of modern fertilizers. The processing of ethene oxide leads to a whole variety of products like glycol ethers, polyurethans or poly(ethylene glycols) which can be found in many consumer goods such as foils, bottles, plasticizers, adhesives, detergents etc. The same holds for methanol which can be considered as a major bulk chemical with an annual production volume of 21.8 million tons (2000) [2]. Methanol is converted to various aldehydes, acids, ethers, olefines etc. Syntheses and refinements of these chemicals have one process feature in common. During their production they have been in contact at least once with a catalyst, mostly a heterogeneous one.

As a consequence of the large scale production of bulk chemicals, minor improvements of catalytic processes have potentially large impacts on the profit margin of companies. Within the perspective of companies the quality criteria of catalysts are not only activity and selectivity. Long term stability, easy handling and even in some case mechanical stability also play crucial roles. Moreover, the performance of the catalyst has to fit into the energy balance of the whole industrial plant. Exothermic reactions e.g. have to run at temperatures above 100° C because otherwise the excess heat cannot be converted into steam providing energy for other processes. Thereby the total energy efficiency can reach values as high as 90%. This economic reasoning was and still is the motivation to search for a complete understanding of heterogeneous catalytic reactions and to optimize existing processes.

1.2 Mechanistic aspects of gas-surface reactions

The first step in every heterogeneous catalytic reaction is the adsorption of reacting species on the active phase of the catalyst which consists mostly of metal particles. There intra-molecular bonds are broken or weakened. Subsequently the adsorbed species react with each other or with gas phase species. This generally occurs in consecutive steps until the desired product is reached which desorbs afterwards. The role of the catalyst is to reduce the activation energy of the rate limiting reaction step. In the literature, heterogeneous catalytic reactions are treated by two mechanisms, the Langmuir–Hinshelwood (LH) [3,4] or the Eley–Rideal (ER) [5,6] mechanism (see Fig. 1.1). In the first case (LH), the actual product formation occurs via a reaction of two or more adsorbed species followed by desorption of the product. Both adsorbed species are in thermal equilibrium with the surface. Therefore the reaction is initiated by the thermal energy provided by the surface. Contrary to the LH, in the ER–mechanism, a new chemical bond is created by a direct collision between a gas–phase molecule/atom with an adsorbed species. Once formed,

Introduction 3

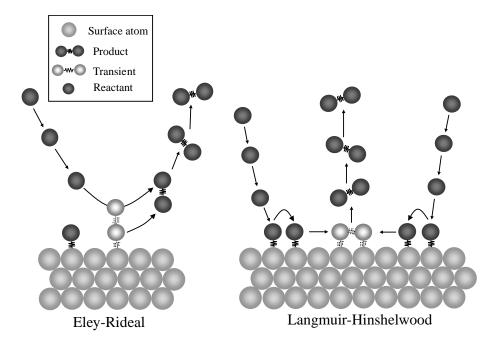


Figure 1.1: Graphic illustration of the Eley–Rideal (ER see left panel) and the Langmuir–Hinselwood (LH see right panel) mechanism. While in an ER–reaction an adsorbed species reacts by a direct collision with a gas–phase species, reactions proceeding via a LH mechanism reactants are equilibrated to the surface prior to reaction.

the product desorbs instantaneously. If the reaction is activated, the energy required to overcome the barrier emerges from the translational and/or internal energy of the impinging molecule/atom. In catalytic research, results are discussed primarily in terms of the LH-mechanism. The ERmechanism is proposed less frequently and has often led to serious dispute among scientists; its actual proof has emerged only slowly [7-10]. The controversy of a strict discrimination between the two models based on classical descriptions of quantum mechanical problems has recently been reconciled by quantum calculations and molecular beam experiments. Harris et al. [11] have demonstrated that a strict discrimination between the two mechanisms is scientifically not vindicated. In contrast, a combination of both mechanisms is required for a correct description of the total reaction mechanism. Furthermore, the contribution of each mechanism to the total reaction is also dependent on the experimental conditions. For instance a particle can be trapped in a metastable state which means that it only partially accommodates to the surface. An interesting consequence of this behavior is that a metastable intermediate is created with such a short life time that it cannot be isolated in a static experiment. Coexistence of both mechanisms has also been retrieved in quantum mechanical calculations. The results of Stampfl et al. [12] reveal different barrier heights for the LH- and ER-mechanisms for the CO oxidation on Ru(0001).

Both mechanisms are valuable because they form the basic approaches for rate equation models. From fits to experimental data, one cannot only determine the significance of one or the other

4 Chapter one

mechanism but, in addition, from the temperature dependence of the reaction rate barrier heights and preexponential factors can be deduced. Both quantities allow the description of the reaction mechanism of the rate limiting step in further detail. Since the experimental determination of preexponential factors is often afflicted with errors the interpretation of this quantity is often not unambiguous. 'Unusually' high or low preexponential factors are frequently rationalized in terms of various ad hoc assumptions concerning the localization and delocalization of transition states and reactants [13]. However, care should be taken upon this way of interpretation because the method of deriving preexponentials assumes that they are temperature independent which might not be always guaranteed [14]. More attention is generally paid to the barrier height which is discussed as an energy required to stretch or break a chemical bond. The common understanding of catalytic activity is that the energetically unfavorable gas-phase transition state is stabilized by the catalyst material which results in a lowering of the gas-phase activation energy. On a microscopic basis, this idea is often pursued by implementing a one dimensional reaction coordinate. Consequently, the activation energy is considered as the only parameter which discriminates between successful and unsuccessful events with the measure being the energy. In reality, this model fails in many cases because it does not account for the other dimensions involved in a surface reaction. Generally, every barrier is composed of various individual barriers because molecules experience slightly different interactions at e.g. different adsorption or impact sites. Another insufficiency of these models is that energy is treated as an 'unspecified' very general quantity which implies that the presence of sufficient energy will automatically force the molecule to cross the barrier. The fact that the energy has to be introduced into a specific reaction coordinate e.g. the intra-molecular bond of the adsorbate is disregarded.

On a more detailed microscopic basis the breaking or the formation of bonds can be understood as the movement of a molecule or molecular fragment on the potential energy surface (PES), which describes all molecule surface interactions and all inter-atomic interactions of the adsorbate. Driven by its translational and internal energy a molecule might move along a certain reaction coordinate which leads to e.g. dissociation. To a first approximation, this process is successful only if the molecule possesses sufficient energy to overcome the barrier. However, due to the multi-dimensionality of the PES the process is more complex: dissociation occurs only if the available energy can be used to cross the barrier along the reaction coordinate. This process is determined by the PES and in particular by the shape of the barrier. Therefore, even if there is excess energy in a molecule, it might still not dissociate. For instance, when dealing with gas surface reactions, one observes for some systems that the probability for dissociative chemisorption is enhanced by vibrational energy whilst for others energy placed into the vibrational coordinate of the molecule is without effect [15]. These observations are in analogy with the concept of gas phase propensity rules introduced by Polanyi [16]. Vibrational enhancement is indicative for a 'late' barrier which means that the saddle point of the barrier lies close to the exit channel. In contrast, vibrational energy can be completely ineffictive if the saddle point of the barrier lies close to the entrance channel.

In summary, the dynamics of molecule surface interactions are complex. If one aims for complete understanding, the knowledge of the PES is indispensable. The only way to accomplish this is by time intensive quantum calculations which presently still cannot include all dimensions relevant to model every single interaction involved. On the other hand, if some basic tendencies or trends of the PES are known, a microscopic model of a reaction step can be already derived. In this context, I will introduce some very pictorial models which illustrate the dynamic interaction

Introduction 5

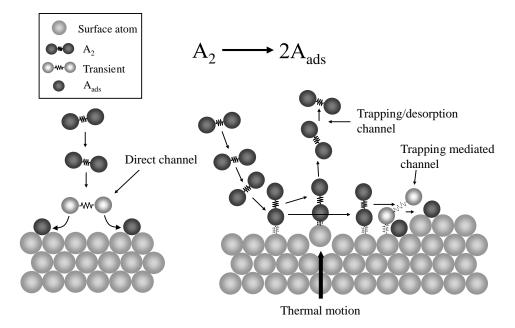


Figure 1.2: Graphic illustration of the 'direct' (left) and surface mediated (right) reaction channel for dissociative adsorption. Left panel: The notation 'direct' implies that a reactant dissociates during the collision with the surface atoms. Right panel: In surface mediated reactions the molecule is first thermally equilibrated to the surface. The molecularly adsorbed species diffuses to an active site followed by dissociation or is released to gas phase by the thermal energy of the surface.

between molecules and surfaces. Since almost every heterogeneous catalytic reaction starts with the breaking of chemical bonds, I will mainly focus on the dynamics of dissociative adsorption because in most catalytic processes reaction sequences are initiated by adsorption and dissociation of reactants. Note that this reaction step is often the rate limiting step. Most dissociative chemisorption processes on bare metal surfaces can be divided into two basic mechanisms. Both mechanisms, the direct and the trapping-mediated are pictorially viewed in Fig. 1.2. In the direct mechanism, a molecule impinging from gas-phase dissociates upon impact with the surface. The dissociation is 'direct' because the chemical bond is broken during the collision of the molecule with the surface atoms. In most cases this process is activated because it involves the cleavage of a chemical bond. Consequently, this reaction channel dominates at high translational energy of the impinging molecule. The second mechanism is the trapping-mediated channel which consists of two or more reaction steps. By an inelastic collision with the surface atoms, the impinging molecule dissipates sufficient energy to become trapped in a shallow physisorption or weak chemisorption well. Initiated by the thermal motion the surface atoms, the molecule diffuses until it finds a reactive site such as a step edge which promotes dissociation. Since the attraction between adsorbate and surface can be weak the molecule has a finite residence time at the surface, and desorption may occur before dissociation.

To obtain a better insight into the dynamics of dissociative chemisorption, both mechanisms

6 Chapter one

are illustrated on the basis of interaction potentials (see Fig. 1.3). The x-axis and y-axis denote the reaction coordinate and the potential energy respectively, both in arbitrary units. For the sake of simplicity a one-dimensional reaction coordinate is chosen. Although, it is an oversimplification it is very instructive and an good starting point for a more complex description. Furthermore, the gas phase energy of the molecule is treated as being of purely translational nature. Failures emerging from these oversimplifications will be pointed out below.

The left hand side of Fig. 1.3 shows the general trends of an interaction potential describing the trapping mediated channel. The first interaction is similar to the 'reflection' event of the direct channel (right hand side of Fig. 1.2). A gas phase molecule with translational energy lower than the energy required to pass the barrier collides with the repulsive wall of the activation barrier. Depending on the efficiency of energy exchange with the surface, the molecule might be trapped in the shallow physisorption well or reflected. The energy necessary to break the intra-molecular bond or to cross the activation barrier has to be provided by the thermal motion of the surface atoms. This is a very crucial mechanistic aspect of this model because the emergence of this channel is controlled by surface temperature. To state it more precisely, the ratio between activation and physisorption energy determines amongst others the reaction rate because of two competing reactions. At a constant surface temperature, the residence time of the trapped molecule is limited by the depth of the physisorption well and height of the activation barrier. Therefore, if the barrier is high and the well depth small (typical for physisorbed systems), molecules desorb rather than react. Moreover, dissociation can also be suppressed by another interaction mechanism which is not obvious from Fig. 1.3. As mentioned above, dissociation proceeds via a molecularly adsorbed intermediate. However, we did not consider the trapping efficiency into the physisorbed state. The probability to trap into this state is not only governed by the gas-surface interaction potential but also by the energy transfer characteristics. In first approximation, if the incident energy of a molecule impinging perpendicularly to the surface plane exceeds the physisorption well depths, the molecule is scattered back into the gas phase. Note that a more detailed description of molecule surface-collisions is given in chapter 3. As a result of this behavior, the surface concentration of the precursor vanishes above a certain translational threshold energy which, strictly speaking, leads to a *energetic poisoning* of the trapping mediated reaction channel.

The right hand side of Fig. 1.3 shows the energetic pathway for a direct channel. This reaction channel is very straightforward in that a molecule dissociates by directly introducing its translational energy into the reaction coordinate. Therefore, the dissociation probability is directly correlated with the barrier height and translational energy. This reaction channel generally prevails and is the only existing reaction mechanism for systems with high barriers combined with shallow physisorption wells because it is impossible to keep the molecule on the surface sufficiently long and provide enough thermal energy (high surface temperature) to pass the activation barrier at the same time. Generally, a strict separation between the two channels is inappropriate. As can be seen from Fig. 1.3, in the case of a trapping–mediated mechanism, the barrier can also be traversed by energetic molecules (direct channel). A very advantageous aspect of this one–dimensional model is that the energy exchange between gas phase molecules and surfaces can be understood quite pictorially. In the case of the direct channel, translational energy is converted into potential energy which is required to stretch the chemical bond illustrated in Fig 1.3 as a spring and later to break it. Astonishingly, dissociative chemisorption of various diatomics or polyatomics such as H_2 , CH_4 or N_2 on metal surfaces can be understood in

Introduction 7

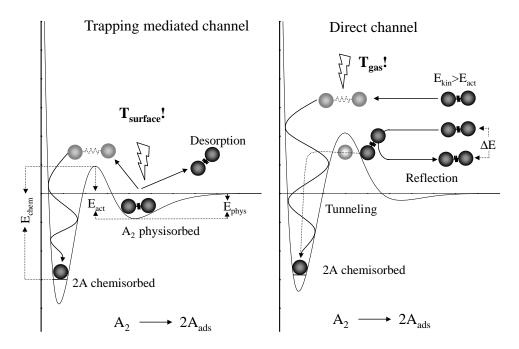


Figure 1.3: Instructive one dimensional potentials for trapping mediated (left) and direct (right) dissociation. Left panel: Thermal energy provided from the surface leads to two reaction paths. Either the molecule traverses the activation barrier and dissociates or the molecule simply desorbs. Right panel: If the mechanism is 'direct', kinetic and/or internal energy of the molecules can be regarded as the energy source to overcome the activation barrier. In the case of light atoms, dissociation can also occur by tunneling through the barrier. If the incident energy is below the barrier height, the impinging molecule is inelastically scattered from the repulsive wall originating from the activation barrier.

terms of this simplistic classical model. These interaction systems show that basically only the normal component of the molecular momentum can be introduced into the reaction coordinate which means that the surface can be considered as perfectly flat. However, these one dimensional models completely fail if energy is introduced into molecular vibrations because the description of vibrational motion requires an additional dimension. As vibrations have to be treated quantum mechanically, the energy content of the vibrational mode has to be corrected for the zero point energies of the molecule and the dissociated products [15]. As already mentioned above, depending on the precise shape of the multi–dimensional barrier, in some cases vibrational energy cannot be converted into the reaction coordinate and is therefore ineffective for enhancing dissociative chemisorption.

The multi-dimensionality of the PES results from the number of relevant degrees of freedom. Therefore, the efficiency of the conversion of energy into the reaction coordinate is determined by the following aspects. First, one has to consider the atomic structure of the surface as not every adsorption site is equivalently active or unreactive. Secondly, because we are dealing with at least a diatomic molecule, rotational and vibrational energy of molecules might play an important

8 Chapter one

role. In addition, molecules impinging from the gas phase onto a surface have an orientational distribution. Therefore, other pathways on the PES are traversed because the molecule has to be reoriented to attain the optimum geometry for dissociation and different barrier heights are probed. Furthermore, quantum mechanical features such as tunneling (indicated on the right hand side of Fig 1.3) should also be considered. Especially if one deals with light masses such as hydrogen, there is always a certain probability that dissociation occurs via tunneling through the barrier [17].

1.3 Molecular beams:

An appropriate experimental tool

Studying the underlying mechanistic aspects of surface reactions experimentally demands welldefined reaction conditions because of the complexity and diversity of molecule-surface interactions; this requires the control of gas-phase as well as surface parameters individually. For instance, as evident from the previous section, already the experimental distinction between a direct and a trapping mediated mechanism requires at least that gas and surface temperature can be manipulated independently because the key difference between the two channels is their different probability of dissociative chemisorption dependent on gas and surface temperature. Experimentally, one has to prevent the establishment of thermodynamic equilibrium between surface and gas phase. This can be achieved by working at gas densities sufficiently low to ensure that no molecule-molecule collisions occur because then no heat exchange can proceed. If one aims for more microscopic details, the situation becomes even more complex. For example, the characterization of a direct channel requires well-defined impact conditions because dissociation occurs throughout the collision. As the efficiency of energy conversion into the reaction coordinate depends on the translational energy, vibrational-rotational mode, orientation and location of impact on the surface, the ideal experiment for studying these different contributions would be to prepare oriented gas-phase molecules in a stationary quantum state and direct them with a well-defined and variable monochromatic energy onto a specific site of a surface. However, site selective impact is virtually impossible but by the use of single crystalline surfaces which can be prepared by standard surface science techniques in ultra high vacuum (UHV) the relative number of different impact sites can be limited. Vibrational and rotational excitations can be controlled by laser pumping. Molecules can be oriented by basically three techniques which apply to molecules with a large dipole, with an unpaired electron spin or to molecules which can be dissociated photochemically [18, 19]. Unfortunately, due to the requirement of these molecular properties the techniques are limited to very few molecules. More general and universal is the preparation of molecules with a defined and variable translational energy and direction by means of molecular beam techniques.

A molecular beam is an ensemble of molecules which travels at a thermal velocity along a pre-defined axis. Experimentally, a beam of molecules can only exist if the background pressure and the pressure in the beam are sufficiently low to prevent molecule-molecule collisions because otherwise molecules would scatter away from their initial direction. As a result, the beam looses its uniformity and at a computable distance away from the source the beam disappears. Moreover, the absence of collisions is crucial because only in that case do molecules remain in the initial energy state in which they were created or prepared. This feature is important if mole-

Introduction 9

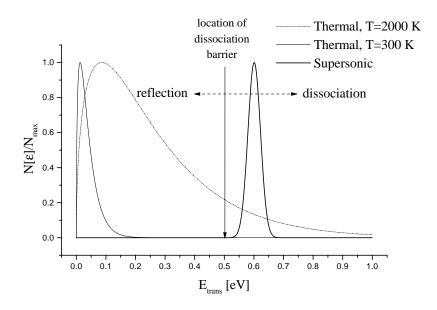


Figure 1.4: A comparison between energy distributions obtained from effusive and supersonic sources. The vertical solid arrow denotes the location of an activation barrier to dissociation. To achieve a dissociation probability of 10% a thermal source has to be heated to 2000 K.

cules are excited by e.g. laser light prior to the interaction with the surface. Molecular beams can be produced by expanding gas through a small orifice (also referred to as a nozzle) into vacuum. Depending on the expansion conditions, an effusive or supersonic beam is obtained. In the first case, the expansion pressure is chosen so low that the mean free path of the molecule is much larger than the diameter of the orifice. Microscopically, the probability that a molecule traverses the orifice is related to the probability that it collides with the area of the orifice. The velocities of the emerging molecules can be described by a Maxwell-Boltzmann distribution with the source temperature characterizing the shape of the distribution. These energy distributions are inadequate for examining activation barriers for two reasons. First, the energy dispersion of these distributions is too large to perform energy-resolved measurement. Second, to achieve a reasonable fraction of energetically high molecules, a source temperature is required where molecules of interest undergo cracking into radicals before reaching the surface or react with the source. This is illustrated in Fig. 1.4 which shows the energy distribution of an effusive source at 2000 K (solid line) and 300 K (dotted line). A fictitious activation barrier height is indicated by a vertical arrow centered around 0.5 eV. This value is not exaggerated for an activated process. For the sake of simplicity, let us consider a direct reaction channel with a single barrier height, where only translational energy E_{trans} is relevant for crossing the activation barrier. Consequently, all molecules with an energy higher than 0.5 eV dissociate whereas surface collisions with lower energy lead to reflection as indicated by the dashed arrows. The fraction of dissociatively adsorbing molecules is given by the integral from E_{trans} =0.5 eV to infinity. Two Maxwell-Boltzmann distributions illustrate the effect of the source temperature on the dissociation probability. Operating

10 Chapter one

the effusive source at room temperature (300 K) the probability of dissociation is effectively zero ($< 2 \times 10^{-6}$ %). This example nicely illustrates why in many surface science studies performed under UHV conditions no or little catalytic activity can be observed. Due to the low pressure ($< 10^{-6}$ mbar) and the cold gas usually introduced into the vacuum by a leak valve (300 K), the impingement rate of molecules with a translational energy above the barrier height is negligibly small. To achieve a dissociation probability of only 10% under these conditions the source temperature has to be increased to 2000 K. Note that under realistic catalytic conditions the pressure provides an impingement rate which is at least 9 orders of magnitude higher than under UHV conditions.

Higher translational energies at moderate source temperatures and sharp energy distributions can be achieved by high pressure expansion. This requires a critical pressure behind the nozzle to ensure that the mean free path of the molecule is much shorter than the nozzle diameter. Under these conditions, the flow becomes hydrodynamic, which means that the gas molecules are literally pushed through the orifice accompanied by many molecule–molecule collisions. The resulting beam is therefore more focused and approximately two orders of magnitude more intense than an effusive one [20]. Since the gas expansion proceeds adiabatically, which means that the enthalpy of the random motions of the molecules is converted to direct mass flow, the gas or gas mixture cools off. Because all streamlines originate from the nozzle, the enthalpy at the source defines a constant which determines the expansion. As the gas expands, enthalpy is transferred into flow velocity and the gas cools down. This cooling results in a narrowing of the velocity distribution of the emerging molecules. Depending on the cooling efficiency, which is influenced by the stagnation pressure, the shape of the nozzle and the gas mixture, fairly narrow energy distributions can be obtained which are very suitable for experiments. The average energy is slightly higher than that of an effusive source and can be approximated as:

$$E_{mean} \approx RT \frac{\gamma}{\gamma - 1} \tag{1.1}$$

where γ is the heat capacity ratio C_p/C_v , T the nozzle temperature and R the gas constant [19,21]. An advantageous side effect of high pressure expansion (also referred to as supersonic or free–jet expansion) is that due to the numerous collisions -typically in the order of 100-1000 during the expansion- the rotational modes of the molecules are cooled quite efficiently which can lead to extremely small rotational temperatures [19]. Contrary to rotations, the vibrations cool less efficiently and therefore survive the expansion. In some cases, the vibrational temperature of the beam corresponds reasonably well to the source temperature and the influence of vibrationally excited molecules can be studied. Moreover, highly energetic beams can be produced by seeding techniques. By mixing a small percentage of the probe gas in a lighter carrier gas such as He or H_2 the probe gas can be accelerated because, during the expansion, the light gas will drag the heavy component. In this way translational energies up to a few eV can be reached. Alternatively, by the same principle fast molecules can be slowed down by heavier ones. The velocity distribution of a supersonic beam can be described by a so–called shifted Maxwell–Boltzmann distribution S(v) which has been derived empirically [22, 23]:

$$S(v) \sim v^3 \exp(-\left[\frac{v - v_{\beta}}{v_{\alpha}}\right]) \tag{1.2}$$

where ν_{β} is the flow velocity and ν_{α} is a measure for the velocity spread. An example of such a distribution is depicted in Fig. 1.4 as a bold line. The plot clearly shows the advantages for the

Introduction 11

application of supersonic beams in surface reaction studies. By seeding techniques, expansion conditions can be chosen for which all molecules possess sufficient translational energy to be able to pass the activation barrier. These properties of supersonic or free–jet expansions are the basis for many gas–phase surface experiments, e.g. in the easiest case one can simply determine the activation energy of a direct channel by measuring the probability of dissociative chemisorption as a function of translational energy. The characterization of such a channel can be specified and a better microscopic understanding can be gained if molecules are oriented or prepared in certain vibrational and rotational states. Furthermore, the capability of tuning the translational energy of molecules means that energy resolved scattering experiments can be performed, which provide detailed insight into energy exchange mechanism with the surface atoms. In this way one can also study the interactions of the non–reacting molecules. Knowledge of these interactions contributes to the understanding of the PES, the attractive and repulsive parts in this case (see also chapter 3).

In summary, molecular beam techniques are a powerful tool to study gas—surface reactions because they allow to direct a beam with narrow energy spread onto a surface under well defined conditions. By this technique, experiments can be carried out where gas and surface temperature can be adjusted independently. This is indispensable to discern between different reaction channels. Technical details and extension of the technique concerning vibrational—rotational pumping and molecular orientation will be given in chapter 5.

1.4 Critical remarks on the surface science approach

Even though molecular beam techniques give the impression that processes relevant to high temperature catalysis can be simulated in a well-defined and controlled way, there are several critical aspects which have to be carefully reviewed before conclusions derived from surface science experiments are transferred to real catalytic processes.

Working with single crystalline surfaces, UHV—conditions are necessary to keep the surfaces free from unwanted adsorbates. Moreover, due to the necessity to decouple gas and surface temperature and due to the fact that a free molecular flow requires a low background pressure the maximum beam intensity is determined by technical restrictions such as pumping efficiencies. As a consequence, there is a difference of at least 9 orders of magnitude in the impingement rate between a surface science experiment and a catalytic process. This problem is known as the pressure gap. Certainly, molecular beam techniques attempt to bridge this gap by providing molecules with sufficiently high translational energy. Unfortunately, this covers only one part of the problem, because in many catalytic reactions a certain steady state concentration of reactants is required to allow them to react which each other. Suppose a catalytic reaction contains a reaction step which proceeds via a surface mediated channel, then the product formation will be inhibited under UHV conditions because only small steady state concentration can be achieved. Hence, for this reason these catalytic reactions cannot be simulated and/or investigated under UHV conditions.

The reason why studies on single crystalline surfaces are so appealing is evident. Catalytic reactions usually occur on fine dispersed metal particles situated in the pores of an amorphous, mostly oxidic support. Therefore the reactants and intermediates providing insight into the mechanism are screened by the surrounding support and difficult to access by experimental techniques. Moreover, as the interesting part of a heterogeneous reaction proceeds at gas—metal interface

12 Chapter one

surface sensitive techniques are needed which are able to discriminate between surface and bulk information. Since many surface sensitive techniques are based on the detection of electrons, high vacuum is indispensable. On the other hand, the complexity of a realistic catalyst complicates studies if one aims for fundamental aspects, because there are too many unknown or hardly defined quantities like e.g. surface structure and composition. This makes it extremely difficult to identify the active sites and their concentrations. Consequently, there are many different reactions and reaction mechanisms proceeding simultaneously and measured activation energies or frequency factors are the result of an averaging over numerous microscopic events. Clearly, from this a detailed microscopic picture cannot be derived because these systems inherently lack a precise description. Solving this problem by using a single crystalline surface creates other problems which are also referred to as material and structure gap. The recurring question which is addressed to all single crystal studies which claim catalytic relevance is how well a single crystal can describe a industrial catalyst. The basic idea behind the use of single crystals is that the small metal particles of a real catalyst do exhibit similar or the same crystalline faces and electronic structures. By an ad hoc assumption it is claimed that the pure metallic phase is active and responsible for the catalytic effect. This argumentation is doubtful because the influence of e.g. support materials or metal particle size are known to affect the catalytic activity quite drastically. Moreover, due to the repetitive structure over a large range ($\approx 1000\,\text{ Å}$) reactions on single crystalline surfaces sometimes give rise to behavior which might not be relevant to catalysis at all. In essence, the dilemma of studying mechanistic aspects of heterogeneous reactions is that realistic systems are too complex and the reaction conditions are too ill-defined to unravel the underlying microscopic details. However, research on single crystals is very instructive for a detailed understanding of the reaction mechanisms but in many cases this type of research lacks the proof of being relevant to related catalytic processes. The aim of surface science should therefore not be to solve problems occuring in catalytic processes, but to reveal fundamental aspects of how surface reactions proceed and provide universal models which can be applied or can find their appliance in the world of catalysis.

1.5 This thesis

The thesis 'Activation barriers in gas surface reactions' highlights different aspects of activation barriers in gas-surface reactions. Emphasis is put on combining experimental results with theoretical simulations and technical innovations. This thesis is structured as follows:

Chapter 1 introduces fundamental models which provide a basic understanding of gas-surface reactions. The relevance of heterogeneous catalysis and the necessity to understand catalytic processes on microscopic scale is accentuated. In addition, the applicability of our experimental approach to solve problems in applied catalysis is discussed.

Chapter 2 reports about the activated CO adsorption on a hydrogen saturated Ru(0001) surface. The presence of a barrier to non–dissociative adsorption could be identified experimentally and theoretically 1. A surprising feature of this gas surface interaction is that the activation barrier arises not due to the breaking of a chemical bond but by Pauli repulsion prevailing initially when CO approaches the surface. Both molecular and site specific adsorption occurs

¹collaborative study, calculations were carried out by I. M. Ciobîcă and F. Frechard in the group of R. A. van Santen

Introduction 13

Chapter 3 deals with the same system as chapter 2 but focuses mainly on the repulsive CO surface interactions. Hydrogen adsorption smears out the effect of corrugation of the clean Ru(0001) surface. Scattered CO molecules follow the trends of a hard cube model with very little energy exchange to the surface

- Chapter 4 is about CO island formation in a hydrogen overlayer. Initially 'magic' islands of 7 molecules form. Since CO adsorption on the hydrogen covered surface is kinetically hindered, CO gas adsorption occurs preferentially on top or along the edges of the islands. As the size of the 'magic' island is increased by one molecule at a time the symmetry of the hexagonal island is broken which leads to a less stable configuration. By a slow 2D–evaporation with a long time constant indicating an activated process, stability can be regained. However, if the impinging flux of molecules is sufficiently high larger islands start to grow because then the growth rate exceeds the rate of evaporation.
- Chapter 5 introduces a new type of molecular beam apparatus designed to operate with three different gas inlets and nozzles. By this means, dosing sequences with highly reactive gas are possible maintaining an ultra compact design. In combination with standard UHV–techniques and the capability to operate in a laser laboratory, this UHV–apparatus provides facilities to study molecule surface interactions under a broad scope of experimental techniques.
- Chapter 6 describes the influence of (100)–steps on the dissociative adsorption of methane on Pt(533). Measurements of the initial dissociation probability reveal two reaction channels. One is identical to the reaction channel on Pt(111) with a barrier height of approximately 750 to 800 meV. This channel can be attributed to methane dissociation on the (111)–terraces of the Pt(533) surface. Methane molecules dissociating on the (100)–step experience a barrier height which is reduced by 250 to 280 meV illustrating that steps are more active in cleaving the C–H bond.

14 Chapter two

Chapter 2

CO adsorption on H saturated Ru(0001)

The interaction of CO with the $Ru(0001)(1\times1)H$ surface has been studied by DFT periodic calculations and molecular beam techniques. The hydrogen (1×1) phase induces an activation barrier for CO adsorption with a minimum barrier height of 25 kJ.mol $^{-1}$. The barrier originates from the initial repulsive interaction between the CO -4σ and the Ru $-d_{3z^2-r^2}$ orbitals. Coadsorbed H also reduces the CO adsorption energy considerably and enhances the site preference of CO. On a Ru(0001)(1×1)H surface, CO adsorbs exclusively on the atop position.

16 Chapter two

2.1 Introduction

The coadsorption of hydrogen and carbon monoxide on the close–packed Ru(0001) surface is particularly interesting because of its relevance to the Fischer–Tropsch synthesis and the methanation reaction [24–26]. While CO and H_2 adsorption on the ruthenium surface has been studied quite extensively over the past decades, little information is available for the hydrogen carbon monoxide coadsorption system on Ru(0001).

The saturation fractional coverage of dissociatively chemisorbed molecular hydrogen is one adatom per Ru(0001) unit cell [27]. While at low surface coverages H resides in the fcc-threefold hollow sites, at saturation coverage H was found to occupy a site of slightly reduced symmetry. This is presumably due to either a shift of the hydrogen adatom towards the bridge position or a reconstruction of the ruthenium surface [28]. Recent DFT-GGA calculations revealed that the adsorption energy below 1 ML hardly varies with coverage. H can be adsorbed up to ≈ 1.5 ML [29] with a small decrease in adsorption energy. Above 1.5 ML the adsorption energy becomes very small and tends to zero at 2 ML.

The CO on Ru(0001) adsorption system has been studied widely [30, 31]. CO is known to adsorb non-dissociatively [30] in the upright position, with the C end facing the surface [32]. The adsorption is non-activated and a precursor model including two intrinsic and one extrinsic precursor has been proposed [33]. The adsorption energy varies with coverage from 160 to 175 kJ.mol⁻¹ [34] in the 0 to 0.33 ML coverage regime. The preferred site is the atop site for coverages up to $\theta = 0.33$ [31]. Note that in this paper adsorption energies are presented with inverse sign. In this respect, a lower energy means a more weakly bound species and vice versa. CO adsorption and dissociation on transition metals has been investigated quite extensively on a theoretical basis by applying various computational methods. Delbecq et al. investigated CO and NO adsorption on Pd(100), Pd(111), Pd₃Mn(100) and Pd₃Mn(111) using extended Hückel [35] and DFT [36, 37] methods. The bridge and the threefold hollow sites are preferred for CO adsorption on bare Pd surfaces. On alloy surfaces, CO adsorption is generally weaker. LDA calculations were carried out by Eichler et al. [38] to examine the CO adsorption behavior on a Rh(100) surface. The bridge position is the most stable adsorption site for CO at all coverages. The ratio between CO molecules adsorbed at the bridge and the atop sites is not constant with the coverage. The difference between the adsorption energies for the bridge and atop positions shows a minimum at half coverage. At high coverage CO, forms a pseudo-hexagonal overlayer with $p(4\sqrt{2} \times \sqrt{2})$ periodicity. Morikawa et al. reported DFT calculations on CO decomposition on Ni(111) and Pt(111), the LDA results are corrected with GGA [39]. The Pt surface is found to be less active, in agreement with experimental results. In the transition state a very long C-O bond (2.0 Å) is observed with the C atom being adsorbed in a three–fold site, while the O atom is in a bridge site. Large scale DFT calculations are used by Hammer et al. to investigate the interaction of CO with stepped and reconstructed Pt surfaces [40]. The adsorption energy on the steps is 70 kJ.mol⁻¹ higher than on the flat terraces. A systematic study of the adsorption of CO on the Pt(100), Pt(110) and Pt(111) is presented by Curulla et al. using HF ab initio cluster models [41]. The geometries and vibrational frequencies are invariant with the cluster size. However, the adsorption energies are very sensitive to the cluster size. The bonding interaction is dominated by the π -backdonation, although the σ -donation plays a significant role. A database of DFT GGA calculations of the chemisorption energies of CO over hexagonal compact surfaces of Ni, Cu, Ru, Pd, Ag, Pt, Au and Cu₃Pt is provided by Hammer et al. [42]. The smallest adsorption energies are found for Au(111) and Ag(111), the highest one is obtained for Ru(0001).

PROBING ATTRACTION 17

CO coadsorption with atomic O on Ru(0001) has been studied by Stampfl et al. using DFT [12, 43]. The oxidation rate of CO is enhanced at high coverages of atomic O because of a weakening of the O–Ru bonds. At low coverage both CO and atomic O are strongly bound and this inhibits CO_2 formation. The coadsorption of O and CO leads to various stable situations. Atomic oxygen resides primarily in threefold hollow sides. At low oxygen coverages, CO induces a restructuring of the O–overlayer to maintain its favorite atop position. Upon increasing the O–coverage, this position is not accessible anymore and CO has to adsorb in the hcp site. Furthermore, when CO approaches the surface a barrier of 30 kJ.mol $^{-1}$ has to be overcome. The oxidation reaction occurs on a (1×1) O phase and can proceed via two channels, namely the Eley–Rideal and the Langmuir–Hinshelwood mechanisms in which the latter one dominates. Wang et al. also reported a study of CO coadsorption with atomic O on Ru(0001) focusing on the tilting of CO [44]. The DFT calculations have been performed with a cluster model. The interaction between CO and O can be described as a field–induced chemistry: the charged atomic oxygen creates a local electrostatic field along the CO adsorption site which modifies the metal–carbon and the C–O bonds, resulting in a tilt of the molecule.

The coadsorption of H and CO has been studied by Peebles et al. [45]. They showed experimentally that the CO sticking probability drops with increasing deuterium coverage, meaning that deuterium acts as a site blocker for CO adsorption. There was no evidence for a chemical reaction between H and CO at 100 K and no additional thermal desorption states appear in the TDS. A strong repulsive interaction between the deuterium atoms and carbon monoxide was also found. Further evidences for this observation were provided by Mak et al. [46], who determined the H diffusion coefficients as a function of preadsorbed CO coverage (θ_{CO} =0-0.2 ML) at T=260 K with LITD. They found a H exclusion radius which is in the order of the van der Waals radius of the CO molecule.

However, even on a fully deuterium saturated surface, considerable amounts of CO, up to 20% of the CO saturation coverage, could be adsorbed [45]. Since the D–CO interaction is repulsive in the mixed overlayer and deuterium blocks adsorption sites, an interesting question is, how a gas phase CO molecule adsorbs in the H overlayer.

In the current study, molecular beam experiments and DFT calculations have been carried out to provide a better insight into the dynamic process of coadsorption. Experiments and theoretical predictions agree that CO adsorption in a H saturated overlayer is an activated process.

2.2 Methods

2.2.1 Theoretical method and surface model

The quantum chemical study was performed using the VASP [47,48] code which allows periodic DFT calculations with pseudopotentials and a plane wave basis set. The approach implemented in the program is based on a generalized gradient approximation with the Perdew–Wang 91 functional [49]. The Methfessel and Paxton's smearing method [50] (σ =0.2 eV) is applied to the electron distribution. The free energy is the variational quantity and the energy is extrapolated for σ = 0.0. The interactions between the ions and the electrons are described by ultrasoft pseudopotentials (US–PP), introduced by Vanderbilt [51] and provided by Kresse and Hafner [52].

We used 4 slab layers with 5 vacuum layers in between in a (2×2) supercell to describe the surface. Adsorption on both sides with an inversion center prevents the generation of dipole—

18 Chapter two

dipole interactions between the supercells. The k-points sampling was generated following the Monkhorst-Pack procedure with a $5 \times 5 \times 1$ mesh. The cut-off energy for the plane waves basis set is 400.0 eV. The coordinates of all atoms were fully optimized. All the parameters (the k-points mesh, the number of metal and vacuum layers, etc.) were tested and carefully selected [53].

2.2.2 Experiments

The experimental setup used in this study has been described in more detail elsewhere [54,55]. Briefly, the system consists of a three–stage differentially pumped molecular beam line attached to a UHV chamber equipped with a low energy electron diffraction (LEED) system, an ion sputter gun and a residual gas analyser. The Ruthenium crystal used was cut and polished to within 0.1° and cleaned by consecutive argon sputtering treatments. Residual carbon was removed by annealing the crystal in oxygen. The surface quality was checked by LEED and by the Debye–Waller analysis of the thermal helium reflectivity which extrapolated to I/I $_0$ =1 at 0 K, where I $_0$ is the incident He–beam intensity indicating a perfectly flat surface. H overlayers were prepared by background dosing 2.5×10^{-7} mbar hydrogen for 10 min at 100 K (150 L).

The translational energy of the beam was varied by using different seeding mixtures of CO in helium and heating the alumina nozzle (300–1100 K). The translational energy of the beam was derived from the TOF distributions which were fitted to shifted Maxwell–Boltzmann distributions. Corrections for triggering time delay, flight time through the QMS and the finite slit width of the chopper have been taken into account. Sticking probabilities larger than 5% were determined using the adsorption reflection technique developed by King and Wells (K&W) [56, 57]. Smaller sticking coefficients were determined from taking the initial slope of the CO uptake (measured by TPD) against beam exposure.

2.3 Results and discussion

2.3.1 Calculations

For the bare Ru(0001) surface the CO adsorption energy (atop) [58] is about 185 kJ.mol $^{-1}$ for 0.33 ML and 173 kJ.mol $^{-1}$ for 0.25 ML. The adsorption energies of CO in the hollow hcp site (one Ru atom from the second layer under the three fold hollow site) is 173 kJ.mol $^{-1}$ for both coverages. The other sites (fcc and the bridge) present smaller adsorption energies (165 kJ.mol $^{-1}$ for fcc and 157 kJ.mol $^{-1}$ for bridge in 2 × 2 and 163 kJ.mol $^{-1}$ for $\sqrt{3} \times \sqrt{3}$). Allowing the CO molecule to tilt will increase the adsorption energy by 6 kJ.mol $^{-1}$ for the atop and the bridge sites ($\theta_{tilt} \approx 3^{\circ}$). In the case of the hcp and fcc sites no changes are observed. The O–end adsorption of CO is not possible in any site, since the CO molecule is repelled from the surface. These results are in good agreement with experimental results [34].

The fully covered H Ru(0001) surface was simulated in a 2×2 supercell, with 4 slab layers, where 4 H atoms were placed on each surface. At coverages below 100%, fcc–sites (no Ru atom of the second layer underneath the threefold hollow site) are slightly more attractive, but the difference between one H atom adsorbed in a hcp or a fcc site is very small with 3.0 kJ.mol⁻¹ at 25% coverage [53] and 4.5 kJ.mol⁻¹ at 100% coverage.

PROBING ATTRACTION 19

	CO atop	CO hcp	CO atop	CO hcp	CO atop	CO fcc
	(no H)	(no H)	+ 4H fcc	+ 4H fcc	+ 4H hcp	+ 4H hcp
Eads	173.3	173.0	45.1	-6.2	74.6	9.8
С-О	1.17	1.19	1.16	1.19	1.16	1.19
Ru–C	1.90	2.15	1.89	2.17	1.87	2.17

Table 2.1: The adsorption energies $E_{\rm ads}$ (in kJ.mol⁻¹) of CO adsorbed on Ru(0001) and H saturated Ru(0001). Adsorption energies for various adsorption geometries and the corresponding bond lengths (in Å) for the Ru–C and the C–O bonds are also listed.

The incoming CO, from the gas phase, has two possible sites for adsorption on the two fully H covered Ru(0001) surfaces, namely the atop position and the threefold hollow site. This leads to four possible adsorption geometries because of the two $(1 \times 1)H$ phases. Results of the adsorption energies and the corresponding bond lengths are displayed in Table 2.1. While CO adsorption in the remaining threefold hollow sites is either weak or not stable at all, only CO adsorbed at the atop sites results in reasonable adsorption energies. The difference between the two atop adsorption energies of the different hydrogenated Ru(0001) surfaces can be explained in terms of their relative stability: the surface with H atoms adsorbed in fcc sites is 18 kJ.mol⁻¹ more stable. If CO is adsorbed at the atop site, the three neighbouring H atoms slightly shift (see Fig. 2.1, top). For H adsorbed in the fcc (hcp) site, two Ru-H bonds of 1.83 (1.83) Å and one of 1.87 (1.86)Å are formed. One H will be not affected because of the symmetries, the respective values for the Ru-H bond lengths are 1.89 Å for H fcc and 1.88 Å for H hcp. In the case that CO is adsorbed in the three-fold hollow sites, three H atoms will undergo a noticeable displacement away from CO (see Fig. 2.1, bottom) as can be seen from the calculated H bond lengths. If CO is adsorbed hcp (fcc) and 4 H adsorbed fcc (hcp) two Ru-H bonds are 2.22 Å (2.16 Å), one 1.63 Å (1.65 Å) for the three shifted H atoms and 1.89 Å (1.88 Å) for the other H atom. Table 2.1 summarizes the C-O and C-Ru bond lengths for the bare and H saturated Ru(0001).

If 4 H are coadsorbed (fcc) to a $Ru(0001)(2\times2)CO$ (atop) the interaction energy decreases drastically (see table 2.1) from 173.3 to 45.1 kJ.mol⁻¹. For the same H overlayer, adsorption of CO in the empty remaining hcp site is weakly repulsive. The CO interaction becomes more attractive if H is moved from the fcc to less favorable hcp sites. If CO is adsorbed atop, the interaction energy increases about 29.5 kJ.mol⁻¹. However, the total adsorption energy including the 4 H atoms differs only by 11.5 kJ.mol⁻¹. The CO interaction is generally stronger if H resides in the less stable hcp site. This can be seen from the small attractive interaction energy when CO is adsorbed in the fcc site.

The adsorption state for CO in a threefold hollow site is destabilized compared to the atop position due to steric hindrance. As discussed later, H and CO sharing a metal atom experience a repulsive interaction which forces the H atom away from the CO molecule. The higher adsorption energy for atop CO can be explained in terms of different H overlayer stabilities. The steric hindrance is less pronounced if CO is in the atop position because the H atoms can move toward bridge sites. If CO resides in the hcp site the H atoms are forced toward the less stable atop sites. Note that the adsorption energy for H atop is 9 kJ.mol⁻¹ while for H bridge it is 41 kJ.mol⁻¹ [29]. Furthermore, if CO resides in threefold sites the H atoms on the surface are more compressed (Fig. 2.1, top and bottom) as the CO–H distance can only be increased at the expenses of significant repulsive interaction between the H atoms. In conclusion, the atop sites

20 Chapter two

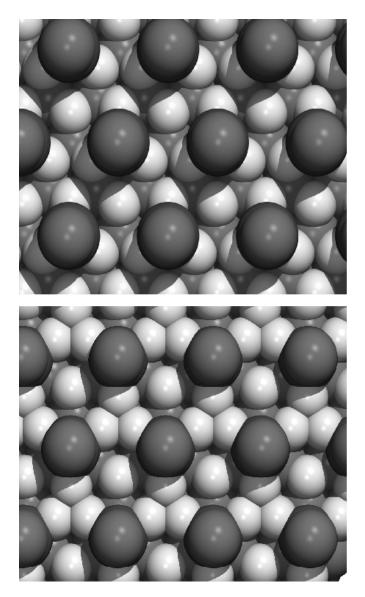


Figure 2.1: The topology of CO adsorbed on a hydrogenated Ru(0001) surface. The top part shows CO molecules adsorbed at the atop sites (25% coverage) together with 4 H atoms adsorbed in fcc sites (100% coverage). The bottom part shows the topology of CO molecules adsorbed in the hcp site (25% coverage) together with H atoms adsorbed on fcc sites (100% coverage).

PROBING ATTRACTION 21

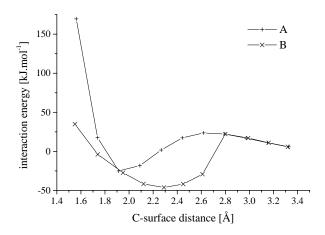


Figure 2.2: The calculated potential energy surface for CO adsorption on a H covered Ru(0001) surface (100%). (A) CO atop + 4H fcc without relaxation of the surface, (B) CO atop + 4H fcc with relaxation of the surface. The y axis denotes the interaction energy in kJ.mol $^{-1}$. The x axis denotes the distance in Å from the C atom of the CO molecule to the surface (i.e. the plane is defined by the three Ru atoms which remain in position).

are the preferred sites for CO adsorption on the hydrogenated Ru(0001) surface.

We now focus on the dynamics of the adsorption. On the bare ruthenium surface CO adsorption is known to be non-activated [59, 60] (see also Chapter 3). To investigate the reaction path, some points on the potential energy surface were chosen by fixing the distance between the carbon atom and the surface plane (practically, the z coordinate of the C atom was not allowed to change). The transition state was refined by performing a quasi newton optimization of the geometry based on the forces and not the energy. Two situations were considered during the CO approach:

- Adiabatic reaction: The CO motion is slow enough to allow the metal surface to relax.
- Non-adiabatic reaction: The CO motion is so fast that the metal atoms cannot relax and the positions of the surface metal atoms are frozen while the H atoms are free.

For the sake of simplicity, we only present results of the 'CO atop + 4H fcc' system because of its experimental relevance. Note that H resides preferentially in fcc sites [28]. Results of the calculation for the hcp systems are almost identical, except for the different adsorption energy.

During all the calculations, CO remained always perpendicular with respect to the surface plane and above its adsorption site. For both approaches (adiabatic and non-adiabatic), a similar barrier of approximately 25 kJ.mol⁻¹ is found (see Fig. 2.2). The major difference between the two different situations (e.g. the adiabatic and non-adiabatic cases) is that, in the case where the CO approaches slowly, the Ru atom underneath the CO molecule can move upwards to initiate the bond. This vertical displacement of the Ru atom is about 0.4 Å for H adsorbed in an fcc site



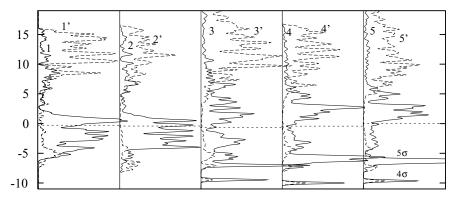


Figure 2.3: The DOS diagrams of the Ru s and Ru $d_{3z^2-r^2}$ atomic orbitals. Solid lines denote DOS of Ru $d_{3z^2-r^2}$ orbitals (labeled #), dashed ones DOS of the Ru s orbitals (labeled with #'). The following situations have been calculated: (1,1') the bare surface; (2,2') surface with 4 H atoms (fcc, 100%); (3,3') Ru(0001)(2×2)CO; (4,4') coadsorption of 4 H and CO on a 'frozen' surface; (5,5') same situation as (4,4') but the surface is allow to relax. The y axis denotes the energy in eV. The x axis is in arbitrary units. The Fermi level was set to 0.0 eV for the CO + 4 H fcc systems. For the other systems the lowest energy level was adjusted to the corresponding level of the CO + 4 H fcc system.

at the minimum of the potential energy surface. This displacement is, however, much larger near the transition state (TS) being 0.7 Å.

Surprisingly, the barriers for the 'frozen' and 'relaxed' surfaces coincide despite the rather different geometries of the transition states (TS). Contrary to the transition states, a clear energy difference is observed for the two minima of the interaction potential. In case of the 'frozen' surface the minimum lies closer to the surface plane and exhibits a much shallower chemisorption well which indicates that most of the CO–adsorption energy is gained from the upwards movement of the Ru–atom. If the surface is 'frozen', the H–bonds are additionally weakened to minimize the energy. The main difficulty to describe the adiabatic adsorption path (curve B figure 2.2) is that on the left side of the TS the Ru atom moves upwards to initiate the CO bond. After the bond is formed the 'Ru-CO complex' moves downwards until the minimum of the system is reached. A better description of the adiabatic path would need at least a two dimensional potential energy surface which would show a very curved path until the TS is reached.

For the 'CO atop + 4 H fcc' system the transition state has also been investigated with the "nudged elastic band" method of Jónsson [61–63]. The same barrier height was found.

As CO is allowed to reach optimum geometry during the calculation, the calculated barrier height should tend to its minimum value. The influence of the C–O bond orientation with respect to the surface normal has been checked by tilting the CO molecule in the transition state. For each calculation, the z coordinate of the C atom and the x and y coordinates of O are frozen once the molecule is tilted. The differences are rather small for angles between 0° and 35° .

The projected DOS diagrams (Fig. 2.3, 2.4, 2.5) for the CO adsorption on the bare and hydrogenated Ru(0001) surfaces bring us to the following conclusions about the quantum chemical

PROBING ATTRACTION 23

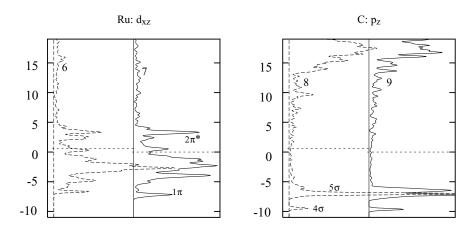


Figure 2.4: The DOS diagrams for Ru- d_{xz} (left panel) and C- p_z (right panel) atomic orbitals. Dashed lines denote calculations for CO adsorbed on atop sites; solid ones denote DOS diagrams after H was added to all fcc sites available. (6) DOS of Ru- d_{xz} orbital of the Ru-atom to which CO binds, (7) same orbital but with all fcc sites occupied by H, (8) DOS of C- p_z orbital, (9) after addition of H (fcc). The y axis denotes the energy in eV. The x axis is in arbitrary units. The Fermi level was set to 0.0 eV for the CO + 4 H fcc systems. For the other systems the lowest energy level was adjusted to the corresponding level of the CO + 4 H fcc system.

basis for activated adsorption and destabilization of CO by the hydrogen atoms.

Let us first consider the σ type interactions between the CO 4σ and 5σ and Ru on the clean surface. The downwards shift of 5σ and the broadening of the metal d-band agree with the conventional picture of a bonding occupied 5σ type surface orbital and partially occupied antibonding 5d type orbitals (see Fig. 2.3 and Fig. 2.4, panels 3 and 6).

The π type interaction for the CO 1π and $2\pi^*$ with Ru on the clean surface is significant (see Fig. 2.4 and 2.5, panels 6 and 10). The d-band broadening indicates a small bonding component under the Fermi level (ε_F). The increased distance between the maxima of the $2\pi^*$ and 1π densities, compared to a free CO molecule, agrees with the antibonding nature of the $2\pi^*$ interaction above ε_F . The adsorption of CO on a bare Ru(0001) surface is not activated, as two opposite phenomena occur simultaneously: the 5σ -Ru- $d_{3z^2-r^2}$ interaction is close to a 4 electron interaction which should give, at the beginning, two filled levels, bonding and antibonding, resulting in a repulsion. Only when the interaction is strong enough to push the antibonding level above ε_F is the system stabilized. At the same time, the CO- 5σ -Ru-s interaction is similar to a two electrons interaction (Ru-s is almost empty) which is bonding along the whole adsorption path and compensates the barrier arising from the 5σ -Ru- $d_{3z^2-r^2}$ antibonding component. The Ru- p_z behaves like the Ru-s but its influence is smaller.

In the presence of only adsorbed H, the metal $d_{3z^2-r^2}$ orbital band is narrower. Indeed, the bottom of the $d_{3z^2-r^2}$ band is bonding for the Ru atoms and mixed with the s band. Once H is adsorbed, the s band interacts mainly with the H atoms (Fig. 2.3 and 2.5, panel 2, 12, the PDOS 12 is similar to the PDOS for H atoms adsorbed without CO, the only noticeable difference is the absence of the tiny peak around -7.5 eV). The s band is essentially involved in bonding with H and is stabilized, while the $d_{3z^2-r^2}$ band is destabilized and narrower. The other components of

24 Chapter two

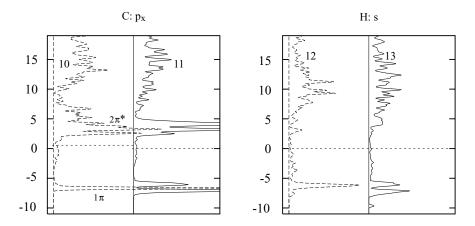


Figure 2.5: The DOS diagrams of the C- p_x (left panel) and H-s (right panel) atomic orbitals. (10) DOS of C- p_x orbital for CO adsorbed atop, (11) same orbital but with H coadsorbed in all fcc sites available, (12) DOS of H-s orbital of the H atom perfectly situated in a fcc site (13) DOS of H-s orbital of the H atoms which shifted towards the bridge sites due to the lateral repulsion. The y-axis denotes the energy in eV. The x-axis is in arbitrary units. Fermi level was set to 0.0 eV for the CO + 4 H fcc systems. For the other systems the lowest energy level was adjusted to the corresponding level of the CO + 4 H fcc system.

the *d* band (not shown) are directly involved in the Ru–H bond and consequently give an extra peak at the maximum of the H PDOS.

For the H/CO coadsorption system on the Ru(0001) surface, we see a small effect on the 4σ but a more distinct effect on the 5σ interaction (Fig. 2.4, panels 8 and 9). One has to remember that CO attracts the Ru atom, resulting in a movement along the surface normal. This is a direct consequence of the Ru–Ru bond weakening which is induced by the CO and H bonding. With H and CO coadsorbed, the middle of the $d_{3z^2-r^2}$ is significantly depleted, compared to H or CO adsorbed separately (Fig. 2.3, panel 2,3 and 4), and the $d_{3z^2-r^2}$ band is either part of bonding levels with H and CO or the related antibonding levels above ε_F . The effects of the coadsorption are less pronounced for the other components of the d band (figure 2.4, panels 6), as the interactions of the CO π orbitals are weaker.

A very small change is seen for the interaction with the $CO-2\pi^*$ orbitals, but a larger difference on the interaction with the 1π . The 1π projected orbital shows clear splitting (Fig. 2.5, panels 10 and 11) due to a direct interaction with the H-s levels. This interaction is bonding as the other H atom (not bound to Ru-CO) has only the upper component (Fig. 2.5, panels 11 and 12) and direct as the d band is not involved (Fig. 2.3 and 2.4, panels 4 and 6). The 5σ is also split but this is due to the coupling of the 5σ and 1π orbitals via the Ru-s H-s levels.

In summary, two points are of importance:

1. On the bare surface, CO adsorption is non-activated. The presence of H results in a activation barrier. This is a consequence of H and CO competing for the s electrons of the Ru atom. The interaction between the s orbital of the Ru atom and the CO-5 σ orbital is always bonding. If H is adsorbed this interaction decreases and can not compensate for the

PROBING ATTRACTION 25

repulsive interaction arising from the 4 electron type interaction of the CO-4 σ orbital with the doubly occupied Ru- $d_{3r^2-r^2}$ orbital.

2. The CO adsorption energy decreases drastically when H is coadsorbed. This can be understood in terms of bond order conservation. The coordination number of Ru increase with coadsorbed H. The Ru atom relaxes upwards, which results in a Ru–Ru bond weakening which is induced by the bonds formed with the H atoms and the CO molecules. For the frozen surface, the weakening of the Ru–H bonds illustrates the competition between CO and H for bonding via the Ru-s orbital. The direct interaction between CO and H seems not to be repulsive as the common levels are stabilized.

2.3.2 Experiments

The dependency of the initial sticking probability, So, on incident translational energy for the clean and H covered surface is given in Fig. 2.6. Both measurements were taken at normal incidence angle, and at a surface temperature of 273 K for the clean and 100 K for the H covered surface. The dynamics of adsorption on the clean surface are described in more detail elsewhere [60] (see also Chapter 3). In the low energy regime between 0.08 and 30 kJ.mol⁻¹, the sticking coefficient on the clean surface remains constant at approximately 0.95, and extrapolates to unity for zero incident energy. This is entirely consistent with a non-activated process in the presence of a deep chemisorption well and has also been observed for CO on Pt(111) [64], Ir(110) [65] and Ni(111) [66]. Upon increasing the incident energy, S₀ decreases gradually with incident energy to 0.82 at 100 kJ.mol⁻¹. The minor changes in sticking probability in the high energy regime is a consequence of the deep chemisorption well, determined to be around 170 kJ.mol⁻¹, depending on the conditions as discussed in the preceding section, where steric effects and impact sites do not play a significant role. The results for S_0 on the clean surface are in qualitative agreement with those presented by Kneitz et al. [67]. Covering the surface with H (150 L) at 100 K leads to a completely different scenario. For low incident energies (< 24 kJ.mol⁻¹) the sticking coefficient remains at a constant value below 0.02. The surface is almost completely passivated for CO adsorption as is evident from the calculations. Similar results have been obtained by Peebles et al. [45], who studied the relative initial sticking coefficient for thermal CO as a function of deuterium coverage. Their relative sticking coefficient decreases linearly with increasing deuterium coverage, and agrees qualitatively well with our results at the H saturation limit. At incident energies between 24 kJ.mol⁻¹ and 100 kJ.mol⁻¹, S₀ scales linearly with translational energy. Above 100 kJ.mol⁻¹, S₀ approaches a constant value of 0.1. The tendency of the sticking probability curve clearly shows that an activated adsorption process is involved. The CO molecule has to overcome a barrier in order to chemisorb. Similar observations have also been made for NO on the H covered Ru(0001) [68] surface.

In the low energy regime, however, the sticking coefficient does not drop to zero but stays constant at a value below 0.02. This clearly indicates an additional non–activated process which can be attributed to sticking at defect sites in the H overlayer. Evidence for this assertion is given in Fig. 2.7.

In order to determine the quality of the H overlayer we have measured the initial sticking probability of a thermal CO beam as a function of hydrogen exposure. The CO sticking coefficient decreases from 0.06 to 0.017 when increasing the hydrogen exposure from 20 L to 150 L at a surface temperature of 100 K. The solid line is to guide the eye. The measurement clearly

26 Chapter two

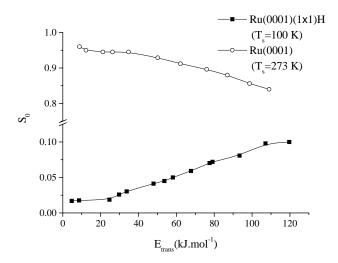


Figure 2.6: The initial sticking coefficient S_0 of CO on clean and H saturated Ru(0001) at normal incident angle as a function of translational energy. The measurements were performed at T_s =273 K for the clean and T_s =100K for the H covered surface respectively.

shows that there is a relation between reactivity and the completeness of the adsorbed overlayer. The differences between the integrated areas under the H desorption peaks are very small, especially for exposure above 50 L, and within the detection limit of our experimental setup(\approx 5% of a ML). The CO sticking curve versus hydrogen exposure clearly shows that the initial sticking probability has not converged yet. Unfortunately, further increase in the hydrogen exposure leads to background adsorption of CO from the residual background gas in the chamber. Therefore, all values of S₀ for CO on the Ru(0001)(1×1)H surface presented here, are with respect to hydrogen exposures of 150 L. Note that thermal fluctuations in the H overlayer could also play a role. Unfortunately, with the experimental tools available, it is not possible to characterize these sites more precisely.

With this in mind, we can estimate the onset of the activated reaction channel by subtracting the defect induced offset, and fitting a line through the linear regime of the sticking curve (see Fig. 2.6). From the intersection with the *x*-axis, we obtain a value for the minimum barrier height in the order of 23 ± 3 kJ.mol⁻¹, which is in good agreement with the calculations (see also Fig. 2.2). As the majority of the unity cell is passivated, the maximum sticking coefficient expected should be low. Due to the repulsive O-end interaction, a considerable amount of molecules will be reflected. Approximately 50% of the molecules should impinge with an orientation where the C-end is closer to the surface than the O-end. Surprisingly, the activation barrier appears to be very broad, with a mean barrier height of 65 kJ.mol⁻¹ and a width of 20 kJ.mol⁻¹, which indicates a broad distribution of barrier heights over the unit cell and possibly also over the different molecular orientations. This result suggests that the minimum energy entrance channel appears to be very narrow, and additional energy is needed if the molecule is slightly laterally displaced with respect to the atop position. This could also imply, that at higher translational energies the precise impacts positions become less relevant and that sites other than the atop po-

PROBING ATTRACTION 27

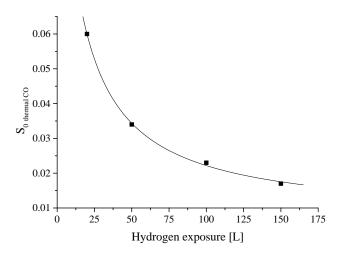


Figure 2.7: The initial sticking coefficient, S_0 , of thermal CO on a Ru(0001)(1×1)H surface at T_s =100 K plotted as a function of hydrogen exposure.

sition might also lead to adsorption. The energy dependence of the sticking coefficient has the typical characteristics of a direct channel. Because of its relatively broad width, it resembles the direct dissociative reaction channel of molecules. In addition, the absence of an enhancement in the sticking coefficient for very low incident energies suggests that a trapping mediated channel is improbable, or not relevant, at the experimental temperature.

2.4 Conclusion

Contrary to the adsorption of CO on a bare Ru(0001) surface, CO adsorption on H covered Ru(0001) surface is an activated process, with the lowest barrier being 25 kJ.mol $^{-1}$ as found by DFT. This value was experimentally verified. Moreover, experiments revealed an additional non–activated reaction channel, which is due to CO adsorption at defects and possibly due to fluctuation of H–atoms within the H overlayer. At high H coverages (1 H per 1 Ru), CO adsorbs preferentially atop because this geometry allows a maximum CO–H distance which is advantageous with respect to the CO–H repulsion. When CO is adsorbed in a hollow site, its σ levels interact with the same Ru levels as H: the in-phase combination of d and s orbitals which corresponds to the bottom (bonding between Ru) of the d–s band. With CO atop, the competition is reduced to the Ru s band. Also, when CO is hollow, the neighboring hydrogens tend to move to atop sites, as two of their three bonds are weakened, while with CO atop only one Ru–H bond is reduced with the H atoms moving to an in–between hollow–bridge site.

Differences in the interaction of CO with the bare and hydrogenated Ru(0001) surface are basically due to changes in the interaction between 4σ , 5σ molecular orbitals of CO and the $d_{3r^2-r^2}$, s and p_z orbitals of the Ru atom. If H is present on the surface, the bond between 5σ -

28 Chapter two

CO and the s orbital of Ru is weakened and the $d_{3z^2-r^2}$ - 4σ repulsion induces a barrier for CO adsorption. As CO and H interact with the lower levels of the d-s band, the Ru atom dramatically moves outwards by 0.4 Å, reflecting the strong weakening of the Ru–Ru surface bonds. The reaction coordinate of CO adsorption on a hydrogenated Ru(0001) surface is dominated by the vertical motion of the metal atom and the need to minimize the CO–H repulsions. This leads to a strongly localized interaction. There is an excellent agreement between theory and experiment concerning the supporting data for the molecular adsorption of CO on a hydrogenated Ru(0001) surface.

Chapter 3

The dynamic interaction of CO with Ru(0001) in the presence of adsorbed CO and H

This study deals with the dynamic interaction of CO with the bare Ru(0001), the fully H and the fully CO covered ruthenium surface. Molecular beam techniques are applied to investigate the potential energy surface of the ruthenium CO interaction and the chemically modified surfaces. The clean surface shows all properties of a deep uniform chemisorption well with a strong rotational anisotropy. The strong chemically attractive interaction can be diminished by CO adsorption which leads to zero sticking even at translational energies as high as 1.2 eV. The angular distribution shows a substantial broadening compared to the clean surface. As recently shown, in the case of preadsorbed H, CO adsorption turns into an activated process with the atop position being the only available adsorption site. Scattering CO molecules from the H–covered surface leads to very narrow angular distributions. The collisions are mainly quasi-elastic.

3.1 Introduction

Bond making and bond breaking on metal surfaces is a big issue in the world of heterogeneous catalysis. This can be, for instance, a simple non-activated adsorption process of a molecule in which a chemical bond is formed when a gas phase molecule approaches the surface. The actual formation of the chemical bond stands at the end of the adsorption process and is preceded by a complex interaction mechanism between molecule and surface with attractive as well as repulsive forces. These forces are described in the so-called potential energy surface (PES) which summarizes all interactions between the surface atoms and molecules involved in the system. While the attraction originates from the energy gain due to the formation of the new bond, the repelling forces can be of electrostatic nature or by Pauli repulsion which occurs when bonding and anti-bonding states become fully occupied. In the latter case, the molecules might also undergo dissociation. Obviously, in a gas phase surface experiment, the interactions between molecule and surface are different for each individual molecule, as every molecule probes different parts of the PES and consequently experiences different forces.

The situation is getting more complex if one allows the surface to reach thermodynamic equilibrium with the gas phase or if other gas phase species are present, because then, the PES changes locally and additional interactions with preadsorbed molecules have to be taken into account.

To illustrate this effect, we have studied the dynamic interaction of CO with the close packed Ru(0001) surface and two extreme cases, namely that with either CO or H saturated surface. This system is particularly interesting due to its catalytic relevance of Ruthenium being a good Fischer-Tropsch catalyst [24–26]. The results are discussed in the terms of a simple classical concept for particle molecule interaction described in the following paragraph.

Molecular beam techniques are a powerful tool to contribute to the understanding of the gas-surface interaction potential because the trajectory of the backscattered molecules or atoms as well as the initial sticking probability are determined by the shape of this potential and the energy exchange between particle and surface. The interaction potential between molecules or atoms consists of attractive and repulsive contributions. In the simplest case, the combination of the two gives rise to a single attractive well and a single repulsive wall. The two contrary interactions influence the trajectory of the impinging particle. This can be illustrated in a simplistic classical picture. If a molecule or atom approaches a surface, e.g. under grazing incident angle, it will be first refracted by the attractive well, which means that its trajectory bends towards the surface normal by increasing its perpendicular momentum. Note, that dependent on the initial angle of incidence θ_i , the translational energy E_i and the magnitude of the well depth, the actual impact parameters differ from the experimentally chosen parameters. The collision with the repulsive wall leads to energy transfer to the surface. This is generally believed to proceed via phonon excitations. Depending on the magnitude of the energy exchange, the molecule or atom either traps in the attractive well or scatters back into the gas phase with a certain energy loss. The actual collision process can be described within two classical limits. One is the hard cube model [69], where only perpendicular momentum can be transferred to the surface. The repulsive wall appears to be perfectly flat for the impinging gas particle, which results in parallel momentum conservation. In this case, the initial sticking coefficient versus incident energy scales consequently with normal energy $(E_n = E_i cos^2(\theta_i))$ instead of total energy (E_i) . The other, the binary collision model, originates from gas-phase scattering and can be understood as a collision between two spherical particles. For both models, one has to assign an effective

mass for the surface, which can be considerably larger than the mass of a single surface atom. The effective surface mass can be understood as the average amount of surface mass involved in the collision. Both models have shown their validity in surface scattering experiments. Classical trajectory calculations on noble gas atoms interacting with metal surfaces have shown a smooth transition from hard cube scattering to binary collisions occurring with increasing incident energy of the impinging particle [70]. These observations can be explained in terms of the ability of more energetic atoms to penetrate the surface to a larger extent. In this case, fewer surface atoms contribute to the repulsion at the turning point leading to a lower effective surface mass. The gas particles start to 'see' the lateral corrugation of the surface structure. The properties of the repulsive wall are therefore dependent on the interaction potential and effective surface mass which in addition changes with incident energy, angle and the surface atom mass. From this, it becomes evident, that the energy exchange of a molecule or atom with a surface is determined by the effective surface mass 'seen' by the impinging particle, the lower the effective surface mass, the higher the energy transfer will be. Note, that the concept of the effective surface is very pictorial. In reality, a collision of a gas phase particle with a surface leads to a coupled motion of numerous surface atoms which is determined by the forces between them. The received energy is then redistributed to surface and bulk via phonons.

The gas-surface interaction is getting more complex if one deals with hetero-nuclear diatomic molecules for example. In this case, the potential energy surface also changes with molecular orientation. As a consequence, the energy-transfer mechanisms are enriched by rotational and vibrational excitations. In summary, the interaction of a molecule or atom with a surface depends on the phonon spectrum of the surface, the masses of gas and surface atom, the attractive well depth and the potential shape which determine the force exerted.

CO is known to adsorb molecularly on Ru(0001) with the C-end attached to the surface [71]. It resides preferentially on the atop position up to a coverage of θ_{CO} =0.33. The adsorption energies for the bridge position and the threefold hollow site differ barely from the atop adsorption site however, indicating a very low diffusion barrier height [58]. At this coverage a $(\sqrt{3} \times \sqrt{3})R30^{\circ}$ superstructure is observed [72]. At CO coverages above $\theta_{CO} \ge 0.3$ the CO overlayers show a complex behavior. Dependent on surface temperature and coverage, various superstructures have been observed using LEED [73–76]. The structure at saturation coverage $(\theta_{CO}$ =0.67) has been described as "hexagonal incommensurate" [77].

The dynamics of CO adsorption from the gas phase has been studied by Kneitz et al. [67]. At normal incidence the initial sticking probability decreases from almost unity to 0.6 on increasing the translational energy to 2 eV.

Molecular hydrogen chemisorbs dissociatively with a saturation fractional coverage, which corresponds to one adatom per Ru(0001) unit cell [27] (1 Ml). While at low surface coverages H resides in the fcc-threefold hollow sites, at saturation coverage, H was found to occupy a site of slightly reduced symmetry, which is presumably due to either a shift of the H adatom towards the bridge position or a reconstruction of the ruthenium surface [28]. From literature it is also known, that the clean ruthenium surface relaxes about 2% by inward contraction, which is relieved by H adsorption [74, 78].

The coadsorption of deuterium and carbon monoxide has been studied by Peebles et al. [45]. They have shown that the CO sticking probability drops with increasing deuterium coverage, meaning that deuterium acts as a site blocker for CO adsorption. No evidence was found for a chemical reaction between H and CO at 100 K. In addition, no further thermal desorption

states appear in the TPD: only the H desorption peak shifts to lower surface temperature as an indication of a strong repulsive interaction between the coadsorbates. Further evidence for this repulsion was provided by Mak et al. [46], who determined the H diffusion coefficients as a function of preadsorbed CO coverage (θ_{CO} =0-0.2) at T=260 K with laser induced thermal desorption (LITD). They found a H exclusion radius in the order of the van der Waals radius of the CO molecule. Helium reflectivity measurements [79] suggest that at low surface temperature (100 K) and low CO and high H coverages, isolated CO molecules are encircled by H atoms. These measurements are in good agreement with the results of Wang et al. [80]. Their infrared data and DFT- calculations on clusters suggest that the coadsorbates avoid each other until a single CO molecule becomes surrounded by H atoms. Despite the repulsive interaction, even on a fully deuterium saturated surface, considerable amounts of CO, up to 20% of the CO saturation can be adsorbed [45].

3.2 Experimental

The experiments were performed in a UHV system attached to a three stage differentially pumped molecular beam line which has been described elsewhere [54,55]. Briefly, the main chamber is pumped by a 500 ls⁻¹ turbomolecular pump and is equipped with low electron energy diffraction (LEED), auger electron spectrometer, an ion sputter gun and two quadrupole mass spectrometers. One mass spectrometer is differentially pumped and can be rotated around the chamber axis. This is used to measure velocity and intensity distributions of particles scattered from the surface.

The sample is mounted along the chamber axis on a three-axis goniometer described in more detail elsewhere [54] which allows all relevant impact parameters such as incident angle and azimuthal angle to be changed. Furthermore, the sample can be tilted with respect to the chamber axis to measure out-of-plane scattering. Heating is provided by radiation and electron bombardement via a tungsten filament at the back of the sample and temperature is measured by a C-type thermocouple.

The molecular beam is generated by supersonic expansion through an $80~\mu m$ ceramic nozzle. The energy of the beam was controlled by seeding carbon monoxide in hydrogen, helium or argon and heating the nozzle between 300 and 1100 K. The beam is modulated with a mechanical chopper prior to its entrance in the UHV chamber. The modulation frequencies of the chopper are typically 480 Hz for a 0.5% and 240 Hz for a 50% duty cycle chopper. The energies of the molecular beams can be determined by measuring the time of flight distributions. The measured TOF-spectra have to be corrected for triggering time delay effects and the time of flight through the QMS and fitted to shifted Maxwell-Boltzmann distributions convoluted over the finite chopper slit width [81].

The ruthenium crystal was cut and polished to within 0.1° of the (0001) crystal plane. The crystal was cleaned by argon-ion-bombardement and repeatedly flashing to 1500 K in 2×10^{-8} mbar oxygen. The remaining oxygen was removed by heating the sample to 1600 K. The surface quality was checked by LEED and by the Debye-Waller analysis of the thermal helium reflectivity which extrapolated to I/I_0 =1.0 at 0 K, with I being the reflected intensity and I_0 the incident intensity of the beam.

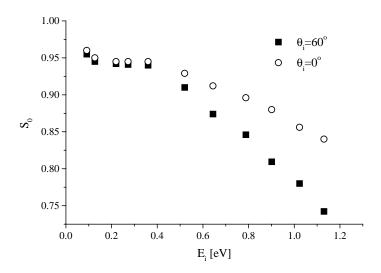


Figure 3.1: Dependence of the initial sticking probability on translational energy for CO on Ru(0001) at 0° (squares) and 60° (circles) incidence angle at a surface temperature of 273 K.

3.3 Results and Discussion

Molecular beam techniques were used to study the dynamic interaction of CO molecules with basal (0001) Ru, the (1×1)H [28] and the fully CO saturated Ru surface. Sticking coefficients were measured using the well-known technique developed by King & Wells [56, 57]. All CO-scattering measurements were made using a molecular beam with a very low intensity to ensure that the coverage build–up for low surface temperatures or the steady–state coverage for higher temperatures was very low. Thus, CO-CO interaction can be excluded. The adsorption of CO usually occurs on Ru(0001) in the molecular form. However, there is evidence from TPD measurements that carbon monoxide undergoes dissociation under high–pressure and high–temperature conditions [82] leading to a high–temperature TPD species around 800 K. Nevertheless, under our experimental conditions no indication was found of dissociative CO adsorption for incident energies up to 1.2 eV based on these observations.

3.3.1 Initial sticking coefficient for CO on Ru(0001)

Figure 3.1 shows the initial chemisorption probabilities S_0 for CO on Ru(0001) in an energy range from 0.045 eV to 1.2 eV at a surface temperature of 273 K and two different angles of incidence. Results for angles between the two, 0° and 60° , were intermediate between the two curves. The sticking coefficient decreases slowly with increasing incident energy for both different angles. For low energies no angular dependency is visible whereas at energies above 0.4 eV the sticking coefficient drops faster for the more grazing incidence (60°) . The results are in qualitative good agreement with those obtained by Kneitz et al. [67] for a surface temperature of 85 K. However, a slightly steeper drop in S_0 was observed in the low energy regime in their

case. Similar results have been observed for CO on Ni(100) [83], Ir(110) [65], Pt(111) [64] and NO on Pt(111) [84]. By extrapolating the energy back to E_i =0, the sticking coefficient reaches approximately unity, meaning that there is no activation barrier involved. This observation has also been made by Pfnür et al. [59] who have measured CO sticking probabilities as a function of surface temperature and surface coverage. From our measurement, we computed the initial sticking probability for a thermal CO beam to be around S_0 =0.93. This value is higher than the value previously published by Pfür et al. [59] ($S_0 \approx 0.7$) but in very good agreement with other recently published results [67]. However in that study, absolute sticking coefficient were determined by work function changes upon CO adsorption having a thermal energy distribution. As already pointed out by Kneitz et al. [67] the absolute values for S_0 from this indirect method came out too low.

Recent DFT quantum calculations [58] have shown that the chemisorption well is almost uniform over the whole unit cell. The adsorption energy varies only about 15% around its maximum value of 1.7eV for CO adsorbed on the atop site. The impinging CO molecule experiences an almost uniform potential well over the whole unit cell. Therefore, there will be no strong lateral dependence of the well depth and the sticking coefficient will be dominated by the energy transfer characteristics of the different sites.

Interestingly, the drop of the initial sticking probability versus energy is much smoother for Ru(0001) than for Pt(111) [64] or Ir(110) [65]. For those metals a decrease of 50% of S_0 has been observed around 1 eV. In order to understand this observation, one has to consider the mechanism of gas phase surface interaction as a function of the impinging molecule energy. At energies above 1eV a considerable amount of surface corrugation is probed, meaning that the turning point of the molecule is shifted towards the surface plane. In other words, the effective surface mass the molecule experiences decreases and reaches a value which can become even smaller than that of one single surface atom [85]. Taking this into account, one can make a crude estimation. The criterion for a molecule to stick, is that the energy transfer to the surface exceeds the energy before acceleration by the potential well. Ignoring the internal degrees of freedom, it can be easily shown that the critical escape energy $E_{\rm c}$ is given by:

$$E_c = \frac{4\mu}{(1-\mu)^2} V_0 \tag{3.1}$$

where μ is the molecule mass divided by the effective surface mass and V_0 is the well depth. The model predicts for a given mass ratio μ a step function for the sticking versus energy with the edge located at E_c . Applying the formula, one can make a comparison between Ru and Pt for instance. As a net result, the critical escape energy should be 3.6 times higher for CO on Ru (V_0 =1.62 eV, $\frac{m_{CO}}{m_{Ru}} = \frac{28}{101}$, E_c =3.62 eV) than for Pt ((V_0 =1.3 eV, $\frac{m_{CO}}{m_{Pt}} = \frac{28}{195}$, E_c =1.01 eV). Clearly, the simplistic model overestimates reality, but it can give some indication for the smoother decrease of S_0 due to the lighter effective surface mass. So far, we have treated the surface atoms as having a cube like shape. Taking lateral corrugation into account one would expect a rounding of the step function centered at E_c with $S_0[E_c] \approx 0.5$ because of collisions with bridge and threefold hollow sites having a higher effective surface mass [85].

In the low energy regime ($E_i < 0.4$) no angular dependency is visible. The sticking coefficient remains constant over the whole energy range. Because of the strong attractive interaction, the CO molecules approaching the surface will be bent towards the surface normal. This refraction has also been seen in classical trajectory calculations [64]. As a consequence, varying the angle

of incidence will not significantly change the impact parameter. Since, the molecules are slow, the interaction time with the surface will be long enough to accommodate the translational energy in the potential well. At higher incident energies a small dependency on θ_i occurs. This is a consequence of two effects. Increasing the translational energy lessens the influence of the refraction of the molecule due to the chemisorption well on one hand, on the other hand the lateral corrugation increases, and in addition the effective surface mass decreases. Due to lateral corrugation, the conversion of parallel to perpendicular momentum, and vice versa, becomes possible. One or the other mechanism prevails, depending on the lateral corrugation, incident energy and well depth. As a net result, the angular dependency of S_0 will be small compared to hard cube scattering and S_0 scales with total rather than with normal energy.

Assuming lateral corrugation for the high energy regime ($E_1 \approx 1 eV$) is a reasonable assumption so far and is consistent with the observations on the other metal surfaces mentioned above. However, our simple explanation lacks the differences in the potential well for a C-end and O-end interaction of the molecule. For the CO-Ru(0001) system, DFT-quantum calculations [58] have shown, that the oxygen Ruthenium interaction is purely repulsive. The repulsion is so strong that during the energy minimization of the calculation the molecule was shifted several Å away from the surface plane. This leads to a strong rotational corrugation of the potential energy surface. Classical trajectory calculations on Pt(111) [64] have shown that the anisotropy of the CO molecule leads to an additional rounding of the sticking versus energy curve in the low energy regime and a tailing in the high energy regime. Nevertheless, as shown in the calculations, the overall sticking probability does not seem to be dominated by the presence of non reactive and reactive orientations. Pictorially, this can be understood as follows. Due to the strong attractive interaction of the C-end and the strong repulsive one for the O-end interaction the molecule can reorient quite easily either when entering the chemisorption well or during the first interaction with the repulsive wall. This is in good agreement with the experimental results and the trajectory calculations for the CO [64] and NO/Pt(111) [84] systems, because the initial sticking probabilities extrapolate to unity for zero translational energy in all cases. The unexpected high sticking coefficient in the low energy regime illustrates, that reorientation has to be accomplished quite easily and the sticking shows basically the trends of the energy exchange characteristics. It has been shown [86] by statistical analysis of trajectories for the NO/Pt(111) system, that due to the complex interactions in most of the collisions, complete randomization of the translational energy occurs which leads to an overall high sticking coefficient. It is therefore difficult to access direct information on the strength of the rotational anisotropy from sticking measurements alone. More interpretable information can be gained by measuring the energy transfer or, even better, the rotational state distribution of backscattered molecules.

3.3.2 CO scattering from Ru(0001)

In order to obtain a better understanding of the dynamic interaction between CO molecules and the Ru(0001) surface, one also has to consider the backscattered molecules, the ones which have managed to escape from the chemisorption well. Due to the high sticking coefficients in the low energy regime, experiments were limited to energies above 0.8 eV. As already mentioned above, in that energy regime a strong effect of the lateral corrugation is to be expected. Figure 3.2 shows angular distributions of CO scattered from the bare Ruthenium surface at 273 K and at 550 K as a function of the outgoing angle and CO scattered from the CO–saturated surface which will be discussed in the following section. CO impinges along the close packed $\langle 11\bar{2}0 \rangle$ azimuth as

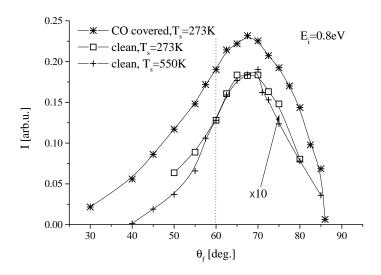


Figure 3.2: Angular–resolved flux distribution of CO–molecules scattered from clean and fully CO saturated Ru(0001) at 60° incidence angle. In the case of the clean surface, two different surface temperatures have been applied, 273 K (squares) and 550 K (crosses). The first one has a CO-surface residence time longer than the measuring time, the second a CO-residence time in the μ s-regime. The fluxes of both distributions have been multiplied by a factor 10.

determined by LEED. The solid lines are to guide the eye. The incident energy was 0.8 eV and the angle of incidence 60°. In the TOF-measurements a single peak appears for the low-temperature experiments whereas at higher temperatures (depicted in figure 3.3) a second peak appears which is due to trapping desorption from the deep chemisorption well. Note, that in the construction of the angular flux distribution only the directly inelastically backscattered molecules are taken into account. The contribution to the angular width and the properties of the molecules that undergo trapping desorption will not be considered in this paper. Comparing the angular distribution from the clean surface at 273 K with the one at 550 K, one finds a striking similarity between the two distributions. The backscattered flux and the width of the distribution almost coincide. This observation is in good agreement with the results from Pfnür [59] et al. who have shown that the initial sticking probability is independent from surface temperature. The absence of a profound surface temperature effect, which should affect the shape of the angular distribution is due to the choice of the high incident energy. At this energy, the thermal motion of the surface atoms is slow compared to the motion of the molecules. Therefore, the molecules probe a pseudo-static surface, where certain surface atoms appear to be vertically and laterally displaced according to their phonon amplitudes. Working at temperatures well above 0 K leads to a loss of structural information. Consequently, the angular distributions broaden and the structural information is lost. The maximum of the angular distribution is shifted towards the superspecular direction, indicating that parallel momentum is retained or badly accommodated throughout the collision. In addition, the deep potential well refracts the escaping molecule towards the surface plane. The angular distribution is asymmetrically broadened towards the subspecular direction and exhibits

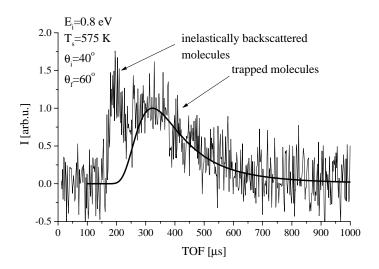


Figure 3.3: Typical TOF spectrum of hyperthermal CO–molecules with a translational energy of 0.8 eV scattered from Ru(0001) at a surface temperature of 575 K. The first peak can be assigned to inelastically backscattered CO molecules, the second peak is due to trapping desorption. The solid line corresponds to a Maxwell-Boltzmann distribution fitted to the experimental data.

a broad tail. There are two possibilities for a molecule to undergo subspecular scattering, the one being a small impact parameter with a surface atom at grazing incidence, the other one being due to multiple collisions, where the energy of the molecule is redistributed in each collision, so that the initial impact condition become less important. From the measured data here, we cannot discern between these two channels. The distributions are surprisingly narrow with a full width at half maximum (FWHM) of approximately 22° . Note, that the widths for a reactive system like NO/Pt(111) [84,87] and an unreactive system like NO/Ag(111) [88] for similar scattering conditions are 36° and 28° respectively. The results are somehow puzzling. Since it is obvious that there is a strong attractive interaction due to the deep chemisorption well, one would expect a broader width of the angular distribution on one hand. On the other hand, the asymmetry of angular distribution is typical for a strong attractively interacting system.

More insight into the scattering mechanism can be gained by the energy transfer characteristics of the molecule with the surface. Figure 3.4a shows the energy transfer behavior of the clean surface at two different incident angles and two different surface temperatures. For an incoming angle of 40° , the energy transfer is almost independent of the outgoing angle and clearly higher than for the more grazing incident angle at 60° . Changing the surface temperature and keeping the angle of incidence fixed, leads to very similar results. Note that for the low surface temperature, sticking is the dominating effect. Therefore, the CO exposure was kept extremely small to avoid CO build—up on the surface (< 3% ML). The results for 40° incident angle suggest a strong interaction between molecules and surface including multiple collisions. For the more grazing incident angle, energy conversion seems to be less efficient. Molecules reflected in the specular direction lose only about 10–20% of their incident translational energy. When scattering in

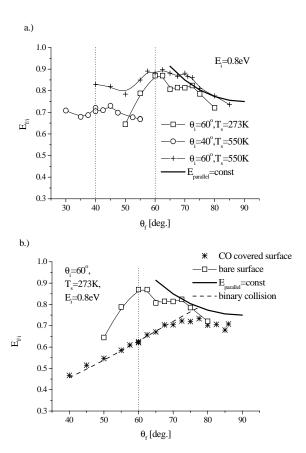


Figure 3.4: Energy–transfer characteristics for CO–molecules scattered from clean and CO–covered Ru(0001). Plotted are the ratios between final ($E_{\rm f}$) and incident ($E_{\rm i}$ =0.8 eV) mean translational energy as a function of outgoing angle. The solid lines through the data points are to guide the eye only, the dotted lines indicate the specular scattering angles and the thick line is a result of the hard sphere scattering formula. For the clean surface (upper panel) two different angles of incidence (40° (circles) and 60° (squares,crosses)) and two surface temperatures (273 K (squares), 550 K (crosses)) are displayed. The energy–transfer behaviour of the CO–covered surface (asterisk) (60° , 273 K) is depicted in the lower panel. The dashed line is a fit through the data points using the hard sphere scattering formula with the only fit parameter being the effective surface mass ($M_{\rm eff}$ =2.2 $m_{\rm CO}$). For comparison, the results from the clean surface (squares) are replotted.

the superspecular direction, the energy transfer almost follows the tendency of parallel momentum conservation. This behavior might suggest that in the superspecular regime, the scattering proceeds via a single, rather than by multiple collision. The surface appears very stiff for the molecules. Note, that parallel momentum conservation is observed in hard cube scattering [69], where only perpendicular momentum can be dissipated.

Resonance-enhanced multiphoton ionization (REMPI) measurements for CO scattering from Ni(111) [89] and NO scattering from Pt(111) [90] have shown that only one rotational rainbow occurs. This rainbow was attributed to O-end interactions with the surface. Wiskerke et al. [91] demonstrated by means of classical trajectory calculations that N-end collisions with surfaces lead to rotational trapping followed by either chemisorption or reemergence due to multiple collisions. Note, that multiple collisions smear out the angular dependency of the energy transfer curve and broaden the angular distribution because the re-emergence angle becomes decoupled from the actual impact in the unit cell. The results strongly suggest that the superspecular scattering for grazing incidence is due to the rotational anisotropy of the molecule. In other words, backscattered CO molecules seem to have not 'seen' the deep chemisorption well. Choosing a small angle of incidence basically means that less surface corrugation is probed, and a larger amount of parallel momentum has to be accommodated or redistributed in order to stick. This enhances the probability for a molecule to emerge after a single collision. This argumentation also holds for the measurements at 40° incoming angle. There, more corrugation is probed due to the larger perpendicular momentum which allows for a more efficient energy exchange or enhanced energy scrambling through multiple collisions. In summary, the energy-resolved measurements show that in the high-energy regime, parallel momentum accommodation is the kev to chemisorption. Comparing these results to the sticking measurements, we find a good agreement. At higher incident angles, this process is less efficient and the emerging molecules consequently have a higher translational energy.

3.3.3 CO scattering from a completely CO-covered surface

Scattering CO molecules from a fully CO saturated surface leads to a very similar angular distribution compared to the clean surface (see Fig. 3.2). The angle of incidence (60°) as well as the translational energy (0.8 eV) are identical to the measurement on the clean surface at 273 K. While the position and shape of the scattering distribution remain almost the same, an increase in the scattered flux and a broader width are observed (32°). The lobe of the angular distribution is shifted slightly to low exit angles. Predosing ¹³CO followed by a high energy exposure of ¹²CO does not lead to any isotope exchange, even for energies up to 1.2 eV. Thus, the system behaves in an inert manner, and there is no displacement, as measured by TPD.

To understand the shape of the angular distribution, one has to consider the modifications of the potential energy surface made upon CO adsorption. Switching from a deep chemisorption to a weak physisorption well modifies the lateral corrugation and the rotational anisotropy of the surface drastically. Since the incident energy is large compared to the well depth, refraction can be neglected. Keeping this in mind, one should be able to compare the results in this study with those from NO on Ag(111) [88] or CO on Ag(111) [92, 93]. The interaction potential between silver and nitrogen oxide is known to be weak with a well depth of 220 meV. Scattering NO from Ag(111) at 60° incoming angle and a translational energy of 1.1 eV leads to a very sharp angular distribution with a width of approximately 15°, which is substantially narrower than that for CO on CO–covered ruthenium. A good explanation for this difference may be that the lateral

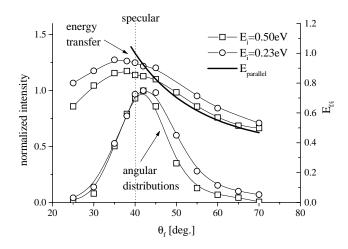
corrugation of a metal surface is smaller due to the delocalized electron band structure. In other words, the repulsive part of the potential energy surface is poorly structured over the unit cell at these incident energies. In contrast, in the case of a CO-overlayer, there is a considerable amount of localized charge, for example, in the oxygen lone pairs. This should lead to a very laterally corrugated potential energy surface. Experimental evidence is given by the broadening of the angular distribution by $10^{\rm o}$ compared to the clean surface, which indicates this increase in lateral corrugation.

Clearly, this effect should also manifest itself in the energy transfer. The energy transfer measurement is depicted in Fig. 3.4b. The molecules experience much softer collisions and the energy transfer drops steeply in the subspecular regime. Note, that we are dealing with equal masses which favours maximum energy transfer. No trapping desorption could be observed in the TOF spectra. Fig. 3.4 also shows two limiting cases of energy—loss mechanisms, one being the conservation of parallel momentum and the other a binary collision model for a effective surface mass of $2.2 \cdot m_{\text{CO}}$. The tendency of the energy transfer towards the binary collision model is in good agreement with a strong lateral corrugation. Classical trajectory calculations and scattering experiments of Argon on Ag(111) [70] have shown that in the first approximation, a smooth transition from hard cube scattering to binary collisions occurs when increasing the incident energy. At energies above 10 eV, the single surface atoms become visible in the energy—transfer mechanism. Depending on the precise nature of the corrugation strength, this smooth transition can also occur at a lower energy. In combination with the angular distribution, the results suggest that we are dealing with a very laterally corrugated potential energy surface.

3.3.4 CO and argon scattering from $Ru(0001)(1\times1)H$

The previous section has shown that a compact overlayer of CO molecules can change the scattering dynamics quite drastically. The collisions between the adsorbed and gas–phase CO molecules appear to be very soft, so the overall amount of energy transferred to the adsorbed overlayer and the underlying ruthenium surface is very high. The situation can be changed radically by adsorbing a monolayer of atomic hydrogen. $(1\times1)H$ overlayers were prepared by background dosing hydrogen. The completeness of the H overlayer was checked by monitoring reflected helium intensity at specular angle until a constant value was reached. It appeared that a dose of 150 Langmuir $(1L=10^{-6} \, \text{Torr} \cdot \text{s})$ was sufficient to saturate the surface.

The adsorption dynamics of CO on the H saturated surface have been discussed in detail elsewhere [94] (see Chapter 2). Briefly, CO adsorption is an activated process with an average barrier height of 0.65 eV and a width of 0.2 eV. For low incoming beam energies, the surface is passivated for CO adsorption. DFT calculations predict a very strong site dependence for CO sticking, namely the atop site with CO attached with the C-end to a ruthenium atom. In addition, surface relaxation is necessary to chemisorb the molecule. In the adsorbed state, the underlying ruthenium atom has to shift about 0.4 Å upwards to make the CO –metal bond. The maximum initial sticking coefficient is about 10% for an incoming translational energy of 1.2 eV. All scattering experiments presented here were done in the monolayer H regime and the zero coverage limit of CO. Fig. 3.5 shows normalized angular distributions and energy transfer curves at incident angles of 40° and 60° for three different energies. The surface temperature was kept at 140 K. For both angles of incidence, the angular distributions are sharp and shifted towards the superspecular direction. Increasing the incident translational energy leads to a decrease in the FWHM (full width at half maximum). For the highest energy (0.80 eV) the narrowest distribu-



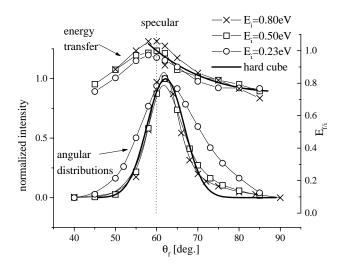


Figure 3.5: Energy transfer behaviour for CO scattered from the $Ru(0001)(1\times1)H$ surface at 140 K. Both the backscattered flux normalized to unity and the energy ratios (E_f/E_i) are plotted in one panel. The thick lines hold for hard cube scattering, the dotted lines mark the specular scattering angle. The upper panel shows results for 40° incidence angle for 0.50 (squares) and 0.23 eV (circles) incoming translational energies, the lower panel for 60° and 0.80 (×), 0.50 (squares) and 0.23 eV (circles). The bold angular distribution is the result of a hard cube model fit for 0.8 eV and 60° angle of incidence.

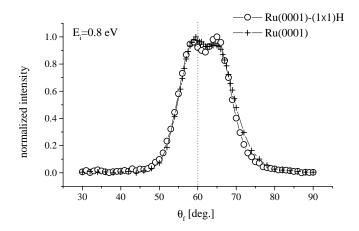


Figure 3.6: Angular distribution for Ar scattered from the clean (+) and H (\circ) covered Ru(0001) surface at 140 K with an incident energy of 0.8 eV and and 60° incident angle. The backscattered flux is normalized to one. The solid lines are to guide the eye and the dotted line marks the specular scattering angle.

tion with a FWHM=8° is obtained. Note that the width is not corrected for the spread of the incident beam, which is in the order of 2°. Similar results for scattering and sticking have been observed for NO on Ru(0001) [68]. Due to the almost completely inert surface, the majority of the backscattered molecules probe the repulsive parts of the unit cell. The others might interact with the chemisorption well, which leads to either sticking or re–emergence, depending on the energy transfer to the surface. The fraction of the backscattered molecules which have 'seen' the chemisorption will be small and contribute to only slightly to the angular distribution.

For comparison, argon has been scattered from the clean and the H-covered surface under identical conditions (E_i =0.8 eV, θ_i =60°, T_s =140 K). Argon has been chosen because of its weak attractive interaction with the ruthenium surface ($\approx 60 \text{ meV}$) [95]. Therefore, the trajectories of the argon atoms are hardly affected by the attractive part of the potential since well depth is negligible compared to the incident energy. Consequently, the interaction between atom and surface is dominated by the repulsive part of the potential. This also holds for the H-covered surface, which is slightly more attractive than the clean one (7 %) [96]. In order to avoid adsorption of hydrogen and carbon monoxide from residual gas during the scattering experiment, especially for the clean surface, only small angular fractions of the distribution have been measured at one time; afterwards, the crystal was flashed, and cooled down, and the following fraction was measured. The results are depicted in Fig. 3.6. The angular distributions for the clean and H-covered surface almost coincide. They are both very sharp with a total width of approximately 15° and show a double peak structure. The width of each individual peak is very narrow ($\approx 8^{\circ}$) and in the order of the single peak observed for CO. The results are somehow astonishing, because the double peak-like angular distributions are usually observed when surface structure becomes visible for the impinging atoms and can be attributed to rainbow scattering [97]. Surprisingly, the argon

atoms are able to probe the lateral structure of the surfaces, even though one would not expect a strongly corrugated PES when dealing with a close packed surface. The precise nature of the argon–ruthenium potential will be discussed elsewhere [98]. More importantly, the experimental results indicate that for an inert gas such as argon, the Ar–Ru interaction hardly changes upon H adsorption. The potential appears to be unchanged, and H seems to be invisible for the impinging energetic argon atoms.

In order to clarify this, we will use our easy concept to explain the experimental observations. As already mentioned in Section 3.1, the trajectories of the impinging molecules or atoms are influenced by the attractive well depth, the mass ratios of impinging atom/molecule and target atom (μ), the phonons and the shape of the potential. The attractive physisorption well for argon and clean and H–covered ruthenium are very shallow and hardly differ from each other [96]. The additional mass introduced by H adsorption, one hydrogen atom per ruthenium atom, can be neglected. However, the effective surface mass might be changed by the repulsive part of the potential. Note, that the repulsion determines with how many surface atoms the argon interacts or in other words, how close the argon atom can approach the surface before it is repelled.

Let us now focus on the phonons. One measure for the stiffness of a surface is the surface Debye temperature because it implies the force constants between surface atoms. This only holds if the energy transfer proceeds via multiple phonon excitations, otherwise the energy transfer is quantized and determined by the coupling of the impinging atom to the phonons. Because of the high incident energy and the heavy argon or CO mass, this is a reasonable assumption. The surface Debye temperatures for the two different surfaces have been determined by Schlichting et al. [95]. They found a slight increase for the H–covered surface. Irrespective of that, Braun et al. [99] showed by means of helium atom scattering that the phonon dispersion curve hardly changes upon H adsorption. They conclude therefrom that the surface Debye temperature must be very similar.

The last undetermined quantity in our discussion so far is the potential. Menzel et al. [96] measured the sticking coefficients for argon on the clean and H–covered surface. From their results, they derived two argon potentials by applying a quantum mechanical model [100], which uses a Morse potential for the interaction. The only unknown quantity in the model is the range parameter, which, together with the well depth determines the shape of the potential. All other parameters entering in the model have been experimentally determined apart from the effective surface mass, which has been set slightly higher than the mass of a single ruthenium atom (finite size effect) but kept constant for both surfaces.

The two potentials differ only slightly in well depth and Debye temperature. This is in good agreement with our experimental results for the argon scattering. The two different surfaces are basically indistinguishable for the energetic argon atoms. Note that because of the high kinetic energy, the shallow physisorption wells will be indiscernible.

Three parameters change when scattering CO from Ru(0001)(1×1)H, namely, the well depth, the mass ratio, μ , and the potential. For CO, a physisorption state on the H–covered surface is unknown, and if it exists, it will be small compared to the incident energy anyway. Since CO is lighter than argon, one would expect the mass ratio to decrease assuming a constant surface effective mass. While for argon, the effective surface mass seems to be unaltered by the adsorbed H atoms, for CO, this quantity will remain unknown, and we defer the discussion to the end of this section. Note that the effective surface mass is coupled to the repulsive part of the potential, which determines with how many surface atoms the molecule interacts.

It is obvious that the major difference of the interactions between CO and the clean and H-covered surface must be the potential. As mentioned above, because of the $(1 \times 1)H$ superstructure, the sticking coefficient drops drastically, an activation barrier evolves, and the lateral corrugation disappears.

Recent density-of-states (DOS) calculations [94] (see also Chapter 2) revealed that the CO surface bond is controlled by the interaction of the 5σ with the $d_{3z^2-r^2}$, p_z and s orbitals of the Ru atom. If H is adsorbed, the repulsive interaction between the CO 4σ and Ru $d_{3z^2-r^2}$ induces the activation barrier.

Together with this barrier, the bridge and threefold hollow site, which do not have an attractive component in the interaction potential yield the repulsive wall from which CO scatters. As seen by the narrow angular distribution, the repulsive part of the potential is very uniform for the measured incoming energies and angles. For the given scattering conditions, the surface turns into a molecular mirror. In contrast to argon, CO does not 'see' the lateral corrugation of the surface. One possible explanation could be that due to the different shape of a diatomic molecule compared to a rare gas atom the rainbow structure might smear out. However, the angular distribution is much narrower for CO than for argon.

The modification of the repulsive potential due to H adsorption should also affect the energy transfer mechanism depicted in Fig. 3.5. For both incident angles, the energy transfer is almost independent of incident energy. The overall energy loss is much lower compared to the CO-covered surface. In the superspecular regime, the energy transfer follows the trend of parallel momentum conservation represented in Fig. 3.5 as a solid line. This behaviour is a consequence of the uniform potential energy surface and can be attributed to hard cube scattering. To illustrate this we have fitted the scattering data of 60° incident angle and 0.8 eV translational energy with the hard cube model. The well depth, the only unknown quantity entering the fit, was set to zero and the effective surface mass $(m_{\rm eff})$ was used as a fit parameter. The fit yields a fairly large value for $m_{\rm eff} \approx 600$ amu. Due to the simplicity of the model, this value can only be considered qualitatively, but it indicates that a large number of surface atoms contribute to the repulsion at the turning point.

Fig. 3.7 shows the interaction potentials of CO with the H-covered and argon with the clean Ru(0001) surface. Both potentials were calculated for the atop site by density functional theory (DFT), the CO one with the C-end facing the surface. For details of the calculations refer, to Ref. [94] or Chapter 2 for CO and Ref. [98] for Ar. A fairly similar theoretical method has also been applied by Stampfl et al. [12] to unravel the reaction mechanisms of CO oxidation on an oxygen-covered Ru(0001) surface. The x-axis denotes the distances between the cores of the carbon or argon and the nearest ruthenium atom. The CO potential allows three interaction mechanisms. If translational energies above the barrier height are applied, the molecule either adsorbs or is backscattered from the repulsive wall of the chemisorption well. For energies below the activation barrier, the molecule is reflected from the repulsive wall of the barrier. Both repulsive walls, which are spatially separated by approximately 1 Å, define a classical turning point for the molecule. As mentioned earlier, this is the only reaction path which leads to sticking. Clearly, when probing parts of the unit cell other than the atop site, no attraction will be present. Since all angular distributions with energies above as well as below the barrier height indicate a uniform potential energy surface, one can consider the repulsive wall of the barrier as a limiting wall for the whole unit cell. If one compares the CO with the argon potential, the calculations show that the classical turning point of the argon atoms lies closer to the surface than the CO

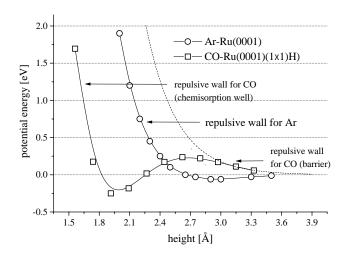


Figure 3.7: Computed interaction potentials of CO and Ar with the atop site. The Ar potential is calculated for the bare ruthenium surface, the CO for the H–covered surface. The x-axis denotes the distance between the cores of the nearest surface atom and the cores of the carbon or argon atom. The solid lines are to guide the eye. The dashed line indicates the repulsive wall of the activation barrier.

turning point. As a consequence, the CO molecules probe a higher effective surface mass and probe less of the lateral corrugation.

3.4 Conclusion

The dynamic interaction of CO with the Ru(0001) surface changes drastically with adsorbed gases. On the clean surface, sticking and scattering are dominated by the deep chemisorption well. As a consequence, the initial sticking coefficient for low incident energies reaches unity and drops almost independently from the angle of incidence with translational energy. The trajectory of the backscattered CO molecules is strongly influenced by the strong lateral corrugation of the potential energy surface and the rotational anisotropy of the molecule, which results in an asymmetrical angular distribution with a long tail towards the subspecular direction. Both interactions also manifest themselves in the energy exchange with the surface, illustrating that due to the strong attractive forces, the experimentally chosen impact conditions become less relevant. Saturating the surface with CO from a thermal source passivates the surface completely for highly energetic molecules. The modified surface exhibits a strong lateral corrugation, and backscattered molecules experience very soft collisions. In contrast, a completely H–covered surface turns CO adsorption into a site–selective activated process with CO atop being the only possible adsorption site. The repulsive part of the surface appears to be extremely flat and stiff. The CO molecules are scattered quasi-elastically which indicates an early classical turning point.

Chapter 4

'Magic' island formation of CO coadsorbed with H on Ru(0001)

The mutual interaction between carbon monoxide and hydrogen coadsorbed on Ru(0001) has been studied by thermal desorption spectroscopy and thermal He atom scattering (TEAS). At 250 K, the hydrogen of a fully hydrogenated Ru surface is displaced by CO. During displacement CO segregates into islands already at very low coverages. At a low exposure pressure (1.5 \times 10⁻⁹ mbar) small islands with a 'magic' size of 7 molecules are formed, whilst higher exposure pressures (2 \times 10⁻⁸ mbar) lead to larger islands. This behavior is in contradiction with the basic concept of island growth introduced by Venables [101].

4.1 Introduction

The system of molecularly adsorbed carbon monoxide and atomically adsorbed hydrogen coadsorbed on single crystalline metal surfaces is fascinating to study because the mutual interactions between the two species give rise to interesting phenomena. While under high pressure conditions on transition metals, chemical reactions such as the formation of alkanes or alcohols occur [24-26], in UHV only little reactivity is found. Especially on closed packed surfaces the interaction between CO_{ads} and H_{ads} can be considered as non-reactive. This inert behavior of an otherwise active catalyst occurs because it is impossible in UHV to thermally introduce sufficient activation energy without desorbing the reactants. Nevertheless, understanding the surface processes under non-reactive conditions can provide valuable information of adsorbate-adsorbate and adsorbate-surface interactions. The CO + H coadsorbed system is complex because the mutual interaction between CO_{ads} and H_{ads} introduces new surface processes or modifies existing ones. First of all, adsorbates compete for adsorption sites which leads to e.g. site blocking or to precursor adsorption. Once adsorbed, the mutual interactions are the driving forces and e.g overlayer mixing, segregation, island compression, coadsorbate-induced site change and/or displacement might occur. Care should be taken in interpreting experimental observations because the combination of the relatively weak mutual interactions and the strong molecule/atom surface interactions gives rise to many metastable adlayers, accessible by appropriate choice of experimental procedures and conditions. This is mainly due to diffusion limitations of adsorbed CO ads or H_{ads} combined with a variety of stable adsorption geometries. Therefore, surface structure and composition can be controlled by varying the surface temperature and by different exposure methods. The different time constants of the adsorption and the overlayer rearrangement processes determine which metastable state will be reached. In this regard, we have investigated the coadsorption of CO on hydrogenated Ru(0001) in situ by thermal helium atom scattering (TEAS) and thermal desorption spectroscopy (TDS). We will demonstrate that small variations of experimental conditions can have a large impact on the structure of the coadsorbed overlayer.

CO adsorbs non-dissociatively on Ru(0001) with the C-end attached to the surface [71]. Non-activated adsorption has been found experimentally by various methods and authors [59, 60, 67]. Up to a coverage of $\theta_{\rm CO}$ =0.33, the atop position is the preferred adsorption site. In the low coverage regime, quantum calculations indicate only a minor variation in adsorption energies between atop and threefold hollow sites. However, the bridge position is energetically less favorable, but still very stable. Due to the small difference in adsorption energy, a very low diffusion barrier height can be assumed [58]. While at surface temperatures below 150 K and $\theta_{\rm CO} \leq 0.18$, randomly adsorbed CO molecules (lattice gas) are in equilibrium with ($\sqrt{3}$ × $\sqrt{3}$)R30° [72] islands, an increase in surface temperature results in an order–disorder transition which can be reversed by a coverage increase (a phase diagram is given in Ref. [77]). The corresponding lateral interactions are a strong nearest neighbor repulsion (0.19 eV) and a weak next nearest neighbor attraction [34,73] (0.26 eV). At CO coverages above $\theta \ge 0.33$, the CO overlayers show a complex behavior. Dependent on surface temperature and coverage, various superstructures have been observed by LEED [73–76]. The structure at saturation coverage $(\theta_{\rm CO}=0.67)$ has been described as "hexagonal incommensurate" [77]. The binding energy ranges from 1.75 to 1.10 eV [34] with increasing coverage.

Hydrogen chemisorbs dissociatively, with a saturation fractional coverage of $\theta_H = 1$ [27]. Atomic hydrogen resides preferentially in the fcc-threefold hollow sites at all coverages, as found by quantum calculations [29]. From the literature it is also known [74,78], that the clean Ruthe-

nium surface relaxes about 2% due to inward contraction, which is relieved by hydrogen adsorption. This is in contradiction with the results from Shi et al. [28] in which they suggested that the adsorbed atomic hydrogen occupies a site of slightly reduced symmetry at $\theta_H = 1$. The symmetry reduction has been attributed to either a shift of the hydrogen adatom towards the bridge position or a reconstruction of the ruthenium surface. The hydrogen desorption energy decreases, with increasing coverage, from 1.2 eV to 0.9 eV.

The coadsorption of deuterium and carbon monoxide has been studied by Peebles et al. [45]. They have shown that deuterium acts as a site blocker for CO adsorption. No evidence was found of chemical reactions between D and CO at 100 K, and no novel thermal desorption states were observed in the TDS. The only difference was a slight shift to lower desorption temperatures, which was attributed to a strong repulsive interaction between the coadsorbates. This observation was supported by Mak et al. [46], who determined the H diffusion coefficients as a function of preadsorbed CO coverage ($\theta_{\rm CO}$ =0-0.2), at T=260 K using laser induced thermal desorption (LITD). Refilling curves indicate a decrease in the H diffusion coefficient with increasing CO coverage. Furthermore, a H exclusion radius for CO was determined from experimental data and found to be in the order of the van der Waals radius of the CO molecule. In the temperature range between 260–280 K, adsorbing hydrogen ($\theta_{\rm H} \approx 0.3$) prior to CO induces the formation of $(\sqrt{3} \times \sqrt{3})$ R30° islands [46]. In contrast, He–scattering measurements [79] suggest that at a low surface temperature (100 K), for low CO and high H coverages, isolated CO molecules are surrounded by hydrogen atoms. These measurements are in good agreement with the results of Wang et al. [80]. Their infrared data and DFT-calculations of CO on metal clusters suggest that the coadsorbates avoid each other until a single CO molecule becomes surrounded by hydrogen atoms. A combination of quantum calculations and experiments recently conducted by us [94] (see also Chapter 2), reveal that a fully H covered surface imposes an activation barrier on CO adsorption. Atop adsorption sites which are still attractive for CO molecules, are no longer accessible for molecules with thermal energy.

4.2 Experimental

The experimental setup used in this study has been described in more detail elsewhere [54, 55]. Briefly, the system consists of a three stage differentially pumped molecular beam line attached to an ultra high vacuum chamber equipped with a low energy electron diffraction (LEED) system, an ion sputter gun and a residual gas analyser. The ruthenium crystal was cut and polished to within 0.1° and cleaned by consecutive argon sputtering treatments. Residual carbon was removed by annealing the crystal in oxygen. The surface quality was checked by LEED and by the Debye–Waller analysis of the thermal helium reflectivity which extrapolated to I/I_0 =1 at 0 K, where I_0 is the incident He-intensity indicating a perfectly flat and clean surface. All Hereflectivity measurements were performed with a thermal beam under 60° incident angle with the detector at the specular position. The beam was modulated by a 50% chopper with a frequency of 475 Hz. The intensities of the reflected beams were determined from the time integrals of reflected He pulses measured with a multichannel scaler. To improve the signal to noise ratio, depending on the exposure time, between 200 and 1000 pulses were averaged which yield time resolutions of the reflectivity between 0.42 s and 2.1 s. Hydrogen overlayers were prepared at the temperature of the experiment (250 K) by backfilling the chamber with a constant H₂ pressure of typically 3×10^{-7} mbar for 5 min (≈ 75 L (L=Langmuir)). The resulting H overlayer was stable

on the time scale of the experiment. Afterwards, the helium beam was exposed to the H saturated surface and CO was introduced into the vacuum chamber by a leak valve. Additionally, the CO partial pressure was monitored by a quadrupole mass spectrometer to correct the reflectivity of the helium beam for fluctuations in the CO exposure and to correlate the He-reflectivity versus time measurement with the start of the CO exposure. The maximum CO exposure pressure was kept sufficiently low (0.015 Ls⁻¹) to maintain adequate time resolution. The maximum CO uptake was less than 0.1% of a monolayer per measured time interval on the H covered surface, with the maximum sticking coefficient determined to be 5%. Initial sticking probabilities were measured using the adsorption reflection technique developed by King and Wells (K&W) [56,57, 102]. Coverages of carbon monoxide and hydrogen were obtained by time integrals of thermal desorption spectra with respect to their values for saturation coverage. Absolute coverages were obtained by correction with the saturation values know from literature [27, 73, 75]. The heating rate was 2 Ks⁻¹.

4.3 Results and Discussion

The mutual interaction between CO and H adsorbed on Ru(0001) at 250 K has been studied by thermal desorption spectroscopy and thermal energy helium scattering to investigate the dynamic interaction between the two adsorbed species.

4.3.1 Thermal desorption

A plot of CO-uptake on the H saturated Ru(0001) surface is given in Fig. 4.1, as constructed from thermal desorption spectra taken immediately after exposing the hydrogenated Ru-surface to CO. As already observed by Peebles et al. [45] and Mak et al. [46], the TDS-spectra of the mixed overlayers do not exhibit additional desorption states, and hydrogen desorption peaks shift to lower temperatures with increasing CO coverage. Both coverages, CO and H are plotted normalized to their saturation coverages at the experimental temperature of 250 K and as a function of CO exposure. The open symbols denote coverage ratios for a constant CO dosing pressure of 2×10^{-8} mbar. In the case of the solid symbols, the CO-pressure was varied between 1.5×10^{-9} mbar and 5×10^{-8} mbar. The plot clearly shows that CO adsorption triggers hydrogen desorption. Interestingly, the CO coverage initially increases at a much slower rate with CO exposure than the H coverage decreases. After a CO exposure of 6 L, the H coverage is reduced to about 30% of its initial value whereas the CO coverage has reached only 50% of its maximum value. Further CO exposure leads to a slow displacement of the remaining H until, after 23 L, all H is desorbed and the surface is saturated with CO.

From the literature, it is known that displacement usually occurs if the adsorption state of the replaced species is weakened due to laterally repulsive interactions through the formation of either a compressed segregated, a mixed compressed segregated or a mixed structure [103]. These structures might not be stable at the experimental temperature and consequently the more weakly bound component desorbs. Examples for H displacement induced by CO adsorption are Rh(111) [104], Pd(111) [105] or Rh(100) [106]. In all these cases the simple intuitive argumentation, that the more strongly bound species displaces the weakly bound species one holds. This seems to be also valid for Ru(0001), if one compares the adsorption and desorption energies for CO and H. The adsorption energy of CO has been experimentally derived from thermal

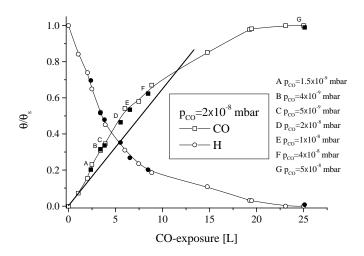


Figure 4.1: Uptake curve for CO on a H saturated Ru(0001) surface at 250 K. CO (squares) and H (circles) coverages are normalized to their saturation coverages. Open symbols indicate measurements with an CO–exposure pressure of 2×10^{-8} mbar. Solid symbols represent measurements where the exposure pressure was varied between 5×10^{-8} mbar and 1.5×10^{-9} mbar

desorption and quasi–equilibrium data [34]. It varies from 1.75 eV to 1.10 eV with increasing coverage. Recent quantum calculations have revealed the binding energies of the different adsorption sites [29, 58, 107]. Theory predicts a preference for CO to reside atop or in a threefold hollow site. Both binding energies are in the order of the experimentally determined adsorption energies. As expected, H is more weakly bound to the ruthenium surface. Desorption energies have been determined from isosteres and an almost linear decrease from 1.2 to 0.90 eV per hydrogen molecule has been found with increasing H coverage (0 < $\theta_{\rm H} \le 1$) [108].

By replotting the data of Fig. 4.1 as H versus CO coverage, one can determine the average number of hydrogen atoms displaced by a single CO molecule as a function of CO coverage (Fig. 4.2 upper panel). The maximum CO and H coverages have been set to $\theta_{CO} = 0.67$ [73, 75] and $\theta_{H} = 1$ [27] as reported in the literature. Up to 0.30 ML CO, the amount of adsorbed H decreases linearly with CO coverage. The slope of a linear fit through the data points yields the stoichiometric displacement coefficient $d_{c}[\theta_{CO} < 0.35] \approx 2.2 \pm 0.15$. The value of approximately two indicates that one adsorbed CO molecule displaces two hydrogen atoms on average which then desorb molecularly. Above 0.35 ML CO the remaining H is displaced less efficiently and approximately two CO molecules are necessary to desorb a hydrogen molecule. From theoretical work [29,58], it is known that the coadsorption of CO and H leads to less and less stable adlayers when the H:CO–ratio is increased together with the total coverage. For a ratio of 4:1, with a corresponding total coverage of 1.25 ML, the CO–H repulsion is so large that a very low adsorption energy is obtained (0.45 eV); this is a good example of a metastable system. From the total energy balance [29,58], it becomes evident that only little thermal energy is necessary to desorb H. Once the total coverage is below 1 ML, much more energetically stable adlayers are

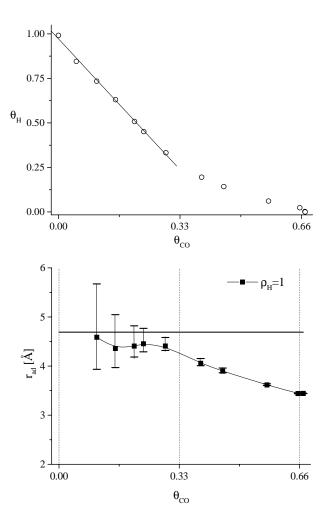


Figure 4.2: Upper panel: The H coverage plotted versus CO coverage. An initial displacement efficiency is derived from the slope of a linear fit through the first 7 data points. One CO molecule displaces two H_{ads}. Lower panel: The average adsorbate–adsorbate distance plotted versus CO–coverage. The solid line denotes the average CO–CO distance in an ordered $(\sqrt{3}\times\sqrt{3})R30^{o}$ structure

formed. These calculations are in good agreement with our experimental results and explain the decreasing displacement coefficient.

From the initial slope of the uptake curve (Fig. 4.1) one can estimate an initial sticking probability for CO on the H covered Ru surface and this is found to be $S_0 = 0.05 \pm 0.02$. Note that we have only taken the first two data points. This value has been independently confirmed by a K&W-measurement with a thermal CO beam at normal incidence. The initial sticking probability is surprisingly high, considering that it has been shown experimentally [94], as well as theoretically [94], that a fully H saturated surface at 100 K is completely inert towards thermal CO (see also Chapter 2). Nevertheless, defects and thermal fluctuations lead to a finite sticking coefficient of $\approx 2\%$ at low temperature conditions. This value is very sensitive to the quality of the prepared H overlayer. Defects or vacancies can considerably increase the initial sticking probability. Based on these observations, two reaction channels have been proposed; an activated one, which can be attributed to molecules with sufficiently high kinetic energy, and a non-activated one, which is due to chemisorption at defect or vacancies sites. Due to the choice of the higher surface temperature in this study, the slightly higher sticking probability observed here seems to be not too unreasonable.

The initially higher displacement efficiency, of one CO against two H, has some interesting consequences on the coverage dependence of the CO chemisorption probability, and this can been seen from the CO-uptake curve (see Fig. 4.1). Up to an exposure of 5 L CO, the slope of the uptake curve rises. In comparison, the initial sticking coefficient determined by K&W is indicated by a straight line in Fig. 4.1. The surface is becoming more reactive, until approximately half of CO saturation coverage is reached. Since it is known that H acts as a site blocker for CO [45], it is evident that additional CO adsorption sites must have been created during the displacement process. One can argue that the repulsive interaction between CO and H leads to a large H exclusion radius for CO, creating CO adsorption sites. This means that the adsorption of gas phase CO occurs preferentially in the vicinity of already adsorbed CO molecules.

An average adsorbate–adsorbate distance can be estimated by determining a CO–density ρ_{CO} with respect to the non–blocked unit cells and this is given by:

$$\rho_{CO} = \frac{n_{CO}}{n_{units} - \rho_H n_H} \tag{4.1}$$

where $n_{\rm CO}$, $n_{\rm H}$, $n_{\rm units}$ are the number of adsorbed CO molecules, H atoms and the total number of unit cells on the surface. $\rho_{\rm H}$ is the site blocking factor, which denotes the number of unit cells blocked by a single hydrogen atom. This mathematical formalism can be understood pictorially as a spatial separation of H and CO into patches assuming a constant H density. The calculated CO–density denotes basically the fraction of CO molecules per non–H occupied unit cells. This allows a direct comparison with the H–free surface. Dividing numerator and denominator of formula 4.1 by $n_{\rm unit}$ yields:

$$\rho_{CO} = \frac{\theta_{CO}}{1 - \rho_H \theta_H} \tag{4.2}$$

The only unknown quantity in this formulation is the site blocking factor, which has to be estimated. As has already been mentioned above, the coadsorption of CO and H on the ruthenium surface leads to thermodynamically less stable structures as the H coverage increases. At a total coverage of 1.25 ML ($\theta_{\rm H}=1,\theta_{\rm CO}=0.25$) the calculated CO adsorption energy is very low, $\Delta H_{\rm ads}\approx 0.45$ eV. With a typical preexponential between $10^{13}-10^{16}$ s⁻¹ for CO and $T_{\rm s}=250$ K, the mean surface residence time would be too low to obtain a stable total coverage of 1.25 ML.

Therefore, the lower limit for the site blocking factor $\rho_{\rm H_{lower}}$ must clearly exceed 0.8. For the upper limit, a value of 1 seems to be reasonable because large CO adsorption energies have been found for 0.25 ML CO coadsorbed with 0.75 ML H. Nevertheless, we have chosen an error bar for the upper limit of 10% ($\rho_{\rm Hupper}=1.1$) and calculated the values for $\rho_{\rm H}=1$. The CO-density can be converted into an average adsorbate-adsorbate distance $r_{\rm ad}$, if one assumes maximum spacing between two adsorbates. Note that the CO nearest neighbor interaction is also repulsive [34, 73]. The distance $r_{\rm ad}$ can be expressed in terms of the Ru lattice constant d_1 as:

$$r_{ad} = \frac{d_l}{\sqrt{\theta_{CO}}} \tag{4.3}$$

On the lower panel of Fig. 4.2, $r_{\rm ad}$ is depicted as a function of the CO–coverage and values of $\rho_{\rm Hupper}=0.8$ and $\rho_{\rm Hlower}=1.1$ serve as error bars. The solid line denotes the CO–CO distances in an ordered ($\sqrt{3}\times\sqrt{3}$)R30° adlayer ($r_{\rm ad}\approx4.69$ Å). The plot clearly shows that the average CO–CO or CO–H distances must be larger than the CO-CO distance on a CO saturated surface over the whole range ($r_{\rm CO-CO}[\theta_{\rm CO}=0.67]$ =3.27 Å). This confirms that the overlayer of the CO and H coadsorbates are not closely packed. Due to the repulsive H–CO interaction, $r_{\rm ad}/2$ can be considered as a H exclusion radius for CO ($r_{\rm ex}$) in the low $\theta_{\rm CO}$ regime. CO occupies laterally almost the same area as in a ($\sqrt{3}\times\sqrt{3}$)R30° superstructure over a broad coverage range (0.1 < $\theta_{\rm CO}$ < 0.33). Considering the upper and the lower limit, all radii seem to have a small offset towards lower values. At CO coverages above 0.30 ML, $r_{\rm ad}$ starts to decline until it reaches 3.44 Å at saturation coverage.

Mak et al. [46] have determined the H exclusion radii for CO on the Ru(0001) surface as function of CO coverage ($\theta_{\rm H} \approx 0.25-0.30$ and $\theta_{\rm CO} \approx 0.06-0.28$). They found that $r_{\rm ex}$ decreases, with increasing CO coverage, to a value which is slightly smaller than the CO separation distance in an ordered ($\sqrt{3} \times \sqrt{3}$)R30° adlayer with a CO coverage of 0.28 ML. In particular, their value for the highest CO coverage is very close to ours for $0 < \theta_{\rm CO} < 0.3$. The relatively loose packing, in the coadsorbed overlayer, supports the proposition that CO adsorbs preferentially in the vicinity of adsorbed carbon monoxide, which accounts for the experimentally observed sticking enhancement. This interpretation is further supported by the considerably high CO sticking coefficient on a CO ($\sqrt{3} \times \sqrt{3}$)R30° adlayer of approximately 0.3 at 250 K [59].

4.3.2 Thermal energy He–atom scattering

In the previous section we have demonstrated that due to lateral repulsive interactions, CO is able to completely displace the H form a hydrogenated Ru(0001) surface. The analysis of the TDS measurements, indicate that up to a CO coverage of $\theta_{CO} \approx 0.33$, the adlayer is relatively loosely packed with respect to the CO saturation coverage. Since the two coadsorbates repel each other the interesting question arises of how the two adsorbates rearrange during the displacement reaction. To study this dynamic process, we have chosen thermal energy He–atom scattering (TEAS), which has proven to be a very sensitive and non-destructive technique to investigate order and disorder phenomena [109].

Island formation

Fig. 4.3 shows the logarithm of the normalized He–reflectivity, scattered along the closed packed $<11\bar{2}0>$ azimuth under specular scattering conditions ($\theta_i=\theta_f=60^\circ$) for the clean and H

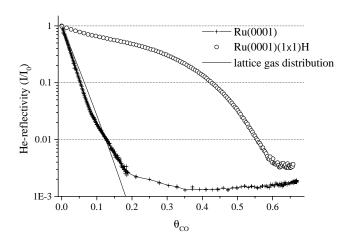


Figure 4.3: Normalized specular He–reflectivity from clean and H saturated Ru(0001) plotted as a function of CO–coverage at 250 K ($\theta_i = \theta_f = 60^\circ$). The solid line shows the He–reflectivity trend of lattice gas behavior for the clean surface. The He–cross section was determined from the initial slope of the curve.

covered surface at 250 K. The He–reflectivity data, measured as a function of CO exposure $(2 \times 10^{-8} \text{ mbar})$, has been converted to CO coverage using the two CO–uptake curves for the different surfaces. On the clean surface the reflected helium signal drops roughly linearly about two orders of magnitude within the first tenth of a monolayer. The first 'kink' around $\theta_{CO} = 0.08$ ML is due to an overlap of cross sections of individual CO molecules and the second kink at $\theta_{CO} = 0.18$ ML can be attributed to the onset of a $\sqrt{3}$ –island formation [76, 77]. From the initial slope of the reflectivity curve, one can calculate the cross section for diffuse scattering, Σ_{CO}^{He} , to be 211 ± 10 Å². Σ_{CO}^{He} can be considered as the area per adsorbed molecule that is no longer reflective for He, due to the adsorption of one CO molecule. It is many times larger than a single unit cell, which leads to an immense decrease of He–reflectivity with coverage and makes it ideally suitable for the investigation of small CO coverages. The value of Σ_{CO}^{He} for our experimental conditions is reasonable considering the large incident angle ($\theta_i = 60^{\circ}$), the translational energy of the He beam ($E_{\text{He}} = 65 \text{ meV}$) and comparable to CO cross sections on Pt(111) [110, 111].

In the context of this paper, we will treat the cross section for diffuse scattering as a qualitative measure for the arrangement of the CO–H adlayer because the large scattering cross section of adsorbed CO molecules can lead, even at small coverages, to substantial overlap of the individual scatterers along the surface. Clearly, the degree of overlap is determined by the actual distribution of scatters on the surface. This allows to distinguish between ordered and disordered systems, and provides qualitative information about the lateral CO–CO interaction as for e.g. repulsion, attraction or non–interaction [109].

To illustrate this, we have simulated the backscattered helium intensity for a non-interacting system. This system is also known as lattice gas where molecules are distributed randomly on

adsorption sites. It can be shown that the intensity is given by:

$$\frac{I}{I_0} = (1 - \theta_{CO})^{\sum_{CO}^{He} n_s} \tag{4.4}$$

where n_s^{-1} is the size of the unit cell [109].

The result of the model with Σ_{CO}^{He} is depicted in Fig. 4.3 as a solid line. The agreement with the data is satisfactory. The slight deviation can be attributed to lateral repulsion, which is not taken into account in the simple model. This assumption is reasonable because of the known repulsive nearest neighbor interaction [34,73]. Note that due to the large cross section the model is only valid up to $\theta_{CO} \approx 0.1$.

In contrast to the measurement on the clean Ru(0001) surface, the behavior of the TEAS signal on the H covered surface is strikingly different. The scattered intensity decreases very slowly with CO coverage. At $\theta_{CO} \approx 0.33$, $\frac{I}{I_0}$ is about 200 times larger than on the clean surface. To interpret the measurement, one has to discuss the influence of the adsorbed H first. As already mentioned above, the He–intensities are normalized with respect to the clean or H covered surface. Saturating the surface with H leads to a reduction of the scattered flux compared to the clean surface. Consequently, the normalization of the intensity leads to two different reflectivity values at CO saturation coverage. The overall observed higher intensity, compared to CO _{ads}, is due to H being an adsorbate with a non–negligible reflectivity [112].

During the adsorption of H on a bare Ru(0001) surface, the He–reflectivity drops to approximately 30% of its initial value but recovers with increasing H coverage to about 80% of its initial value. This decrease and increase can be explained in terms of two different scattering cross sections. In the low H coverage regime, diffuse scattering occurs from single adsorbed hyrdogen atoms whilst in the high coverage regime, H vacancies are responsible for reduced reflectivity. Fully hydrogenated Ru(0001) acts as an atomic mirror for helium atoms. The contribution to diffuse scattering of adsorbed hydrogen or hydrogen vacancies is much smaller compared to that of CO. Therefore, the observed changes in He–reflectivity can be predominately attributed to CO–coverages and CO–arrangements on the surface.

The adsorption of CO on hydrogenated Ru(0001) reveals a combination of both scattering features, a very slow decrease of backscattered He–intensity, which is typical for adsorbed H, as well as very weak reflectivities for CO coverages above 0.4 ML, which is a property of a perfectly diffuse scatterer. These observations suggest either a strong variation in cross section for CO surrounded by adsorbed H, or a different lateral arrangement compared to the H–free surface. The first assertion seems very unlikely because it has been shown for CO and H on Pt(111) that the CO cross section in the H environment matches the one of the clean surface [113, 114]. Consequently, the change in reflectivity behavior has to be attributed to different lateral distributions. The high reflectivity suggests segregation of CO and H into islands even at CO coverages below 0.01 ML and $T_{\rm s}=250$ K. To verify this, one can make a crude estimate of the expected backscattered He–flux assuming all molecules are located in islands. We have chosen $\theta_{\rm CO}=0.33$ because, on a bare Ru(0001), an ordered $\sqrt{3}\times\sqrt{3}$)R30° structure is observed and, due to the fact that at 0.33 ML CO, the backscattered He–intensity is virtually zero. From the lower panel of Fig. 4.2 one can deduce a relative value for the density in a CO island which is proportional to $r_{\rm ad}^2$. The fraction ξ of surface area not occupied by CO, is given by:

$$\xi = 1 - \frac{r_{ad}^2 [\theta_{CO} = 0.33]}{r_{\sqrt{3}}^2} \tag{4.5}$$

where $r_{\sqrt{3}}$ is the CO–CO distance in an ordered $\sqrt{3} \times \sqrt{3}$)R30° superstructure. Using the appropriate value for $r_{\rm ad}$ at 0.33 ML, ξ =0.23 \pm 0.02. If one assumes that the remaining H patches on the surface reflect the helium perfectly, and that island shadow effects are neglected, the reflectivity $\frac{I}{I_0}$ at $\theta_{\rm CO}=0.33$ can be approximated to be ξ , which is in excellent agreement with the measured intensity of $\frac{I}{I_0}=0.22$. It is quite surprising that this simple model predicts the measured intensity so well, since it neglects the presence of CO molecules. One can estimate the detection limit of single scatterers surrounded by CO–islands to be lower than 0.001 ML. This fractional coverage would lead to an additional reduction of the computed helium intensity of 5% which should be noticeable. The absence, or the low amount of isolated CO molecules, suggests that stable clusters are formed.

In conclusion, the behavior of the TEAS curve is consistent with a model where CO and H are segregated on the surface. While CO displaces H, there is also a structural rearrangement on the surface. The repulsive CO-H interaction forces the adsorbates to form islands. CO-H island formation has been seen on various metal surfaces, for e.g. Pt(111) [115], Ni(111) [115], Rh(111) [104], Pd(111) [105] and Rh(100) [116]. For Ru(0001), contradictory interpretations of experimental results have been published. Peebles et al. [45] have studied the CO and H coadsorption at 100 K by work function changes, UPS, XPS and TPD. By direct comparison of their results with those from Rh(111), they propose the formation of a segregated overlayer. Some evidence for overlayer segregation was found by Mak et al. [46]. Their LEED experiments revealed that coadsorption of CO, to a relative small H coverage (0.3 ML) at temperatures above 260 K, does not disturb the onset of CO island formation. In contrast, Braun et al. [79] infer from high resolution helium atom scattering, that CO is surrounded by H and not by CO molecules at low coverages ($\theta_{\rm CO} \approx 0.09$, $T_{\rm s} = 100$ K). Their argumentation is based on the differences in the frequency of frustrated translational modes for isolated CO molecules and CO molecules in ordered CO superstructures. The frequency observed for CO coadsorbed with H turns out to be even higher than for the isolated molecules which rules out CO island formation. This is at odds with our experimental observations. It should be noted, however, that our experiments have been conducted at a higher surface temperature, which enhances adsorbate diffusion. The increased mobility on the surface certainly aids in overcoming a metastable state, and favors thermodynamic equilibrium being reached.

Island size and island density

It has been shown that He–scattering offers the possibility to determine an average size of islands per unit cell [109]. In the limit of island sizes which are much smaller than the transfer width of the instrument, $\frac{I}{I_0}$ can be approximated to

$$\frac{I}{I_0} \approx (1 - n_s \cdot U \cdot \theta)^2 \tag{4.6}$$

where U denotes the area of the unit cell of the adlayer. The model predicts a parabolic decay of $\frac{I}{I_0}$. This is clearly not the case, as can be seen from Fig. 4.3. Due to the fact that the model (equation 4.6) does not account for island edge effects, which are relevant when dealing with small islands, we have refined the model by implementing a shadow around the islands.

In the absence of isolated CO molecules, θ_{CO} equals $\theta_{CO} = \tilde{n} \cdot \tilde{n}_i$ where \tilde{n} is the mean number of molecules per island and \tilde{n}_i the island density per unit cell. $U \cdot \theta_{CO}$ can then be rewritten as

 $\sum_{i}^{He}[\tilde{n}] \cdot \tilde{n_{i}}$. The cross section of an island with \tilde{n} molecules $\sum_{i}^{He}[\tilde{n}]$ has to be calculated. Therefore, the following approximations have been made.

- 1. The presence of adsorbed H does not affect the CO cross section [113, 114].
- 2. All CO molecules are situated in islands, so that $\theta_{CO} = \tilde{n} \cdot \tilde{n}_i$.
- 3. The area A_i occupied by an island can be described by a circle with radius $r_i = \sqrt{\frac{A_i}{\pi}}$.
- 4. The mean number of molecules per island is given by $\tilde{n} = \rho_{CO}^A \cdot A_i$ where ρ_{CO}^A is the CO density inside an island ($\rho_{CO}^A = \rho_{CO} \cdot n_s$, see also equation 4.2). ρ_{CO} is assumed to be constant over the fitted coverage range and is set to 0.36, which corresponds to $r_{ad} = 4.5 \text{ Å(see Fig. 4.2)}$; r_i can be written as $r_i = \sqrt{\frac{\tilde{n}}{\pi \cdot \rho_{CO}^A}}$.
- 5. Island edge molecules superimpose a shadow around the island; r_i is increased by $\Delta r_{\Sigma_{\text{CO}}^{\text{He}}} = \sqrt{\frac{\Sigma_{\text{CO}}^{\text{He}}}{\pi}}$.
- 6. $\tilde{n_i}$ is constant over the chosen coverage range. Note, that a constant island density requires a growth process, where the probability for a diffusing molecule to collide with an existing island is higher than for nucleation to a new island. This should be the case for higher CO coverages.

With those assumptions and $\theta_{CO} = \tilde{n} \cdot \tilde{n_i}$, $\sum_{i=1}^{He} [\tilde{n}]$ can be written as:

$$\sum_{i}^{He} \left[\frac{\theta_{CO}}{\tilde{n}_{i}} \right] = \pi \left(r_{i} \left[\frac{\theta_{CO}}{\tilde{n}_{i}} \right] + \Delta r_{\sum_{CO}^{He}} \right)^{2}$$

$$(4.7)$$

Substitution into equation (4.6) leads to the desired fit function with the only fit parameter being the island density. We have tried to fit the curve for $0.01 < \theta_{CO} < 0.3$, knowing that the choice of the lower limit might violate approximation 6. The upper limit of 0.3 ML is determined by condition 4 and by the coverage where islands start to coalesce or cross sections overlap. The results of the fit are depicted in Fig. 4.4 (upper curve (o)). Despite the simplicity of the model, an excellent agreement between experimental data and the model, even at very low coverages is found. The fit yields a value for the island density of $\tilde{n}_i = 8 \times 10^{12} \text{ cm}^{-2}$. The corresponding number for the average island size has been calculated and plotted as a function of coverage. It ranges from 50 molecules at $\theta_{CO} = 0.01$ to about 1000 molecules at $\theta_{CO} = 0.3$. These values are somehow surprising. Since the CO diffusion does not seem to be rate limiting, one would expect to obtain larger islands accompanied by smaller densities. Note that the island size determined in our study has to be considered as an upper limit because the model does not account for an island size distribution. As has already been pointed out by Williams et al. [117], the average value of an island size distribution can substantially differ from an experimentally determined mean size if data are fitted to a fixed size. Nevertheless, the fit to the experimental data supports the idea of an early-stage nucleation process which then leads to a constant island density. Growth proceeds by the incorporation of CO molecules into existing islands, by either CO diffusion or direct impingement. Consequently, nucleation of CO molecules to growth centers should determine the outcome of the cluster size as a function of coverage. Clearly, the more growth centers which are initially built, the higher the island density and the smaller the island size will be.

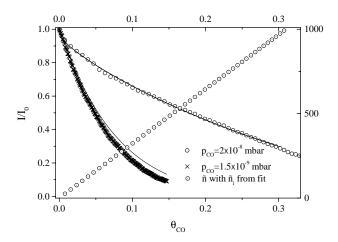


Figure 4.4: He–reflectivity measurements for the highest $(2 \times 10^{-8} \text{ mbar})$ and lowest $(1.5 \times 10^{-9} \text{ mbar})$ exposure pressure. Solid lines represent fits for two different models. In the case of the higher exposure pressure, the model is based on a growth process which assumes a constant island density (\tilde{n}_i) . With the fitted value for \tilde{n}_i , the number of molecules per island $\tilde{n}(\odot)$ is plotted versus CO–coverage. For the lower exposure pressure, the model assumes lattice gas behavior of 'magic' islands containing 7 molecules.

Flux dependency of the island size

Theoretically, island growth has been described by mean—field rate equation theory [101], which assumes a lattice gas and small clusters in local equilibrium. If a small cluster exceeds a critical size, it does not dissolve anymore and is considered as a growth center. Usually one observes that the interplay between the flux of the impinging molecules or atoms and the rate of surface diffusion determines island densities. A high flux leads to small islands and large densities and vice versa. This model has been proven to work well for e.g. metal on metal deposition or condensation of rare gas atoms on surfaces, where strong attractive forces rule the adsorbate—adsorbate interaction. Due to the discrepancy between obviously high CO mobility and the small island sizes, it is especially interesting to investigate the flux—dependency of island formation to unravel the underlying mechanism. In addition, the theory based on attractive adsorbate—adsorbate interactions can be tested for a system where island formation is mostly driven by repulsive forces.

As was already mentioned in Section. 4.3.1, the CO-uptake is flux-independent. Therefore, the CO-uptake, depicted in Fig. 4.1, was utilized for coverage calibration. The results of the flux-dependent measurements are depicted in Fig. 4.5. Normalized He-reflectivity is plotted versus CO coverage. The exposure pressure was varied between 1.5×10^{-9} mbar and 2×10^{-8} mbar. The lower the exposure pressure, the quicker the helium reflectivity drops with coverage. Comparing the He-reflectivities at, for e.g. $\theta_{CO} = 0.14$, a change in intensity of almost an order of magnitude between the lowest and the highest pressure is observed. The results clearly indicate that the distribution of CO molecules on the surface is flux-dependent. Applying the mean-field

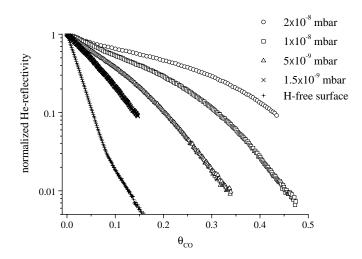


Figure 4.5: Flux dependency of the He–reflectivity. The experimental data were taken for exposure pressure between 1.5×10^{-9} mbar and 2×10^{-8} mbar keeping the Ru(0001) or the hydrogenated Ru(0001) surface at 250 K. Scattering conditions are identical to those described in Fig. 4.3

rate equation theory, one would expect fewer but larger islands at constant coverage for the lower flux. The results are very counterintuitive because one would expect more smaller islands at high flux in combination with more isolated CO molecules. The opposite is observed. At a constant coverage, smaller islands imply a higher island density. Due to the cross-section of island edge atoms, the actual island size 'seen' by He atoms increases. With decreasing island size, the total amount of island edge atoms increases, which leads to a lowering of the He-intensity. This only holds if the reduction in He-reflectivity can be strictly linked to island sizes and densities. Another possibility, for the lower intensity, could be the presence of lattice gas in the case of the low exposure. However, it is obvious from the high exposure experiment that diffusion limitations are out of question. In contrast, a lower CO pressure would substantially increase the time available for diffusion. A higher cross-section of large islands, compared to closed-packed ones, could also account for a lower intensity, which could be caused e.g. dendritic islands. This growth type occurs if the aggregation process is diffusion limited [118, 119]. This would require a flux-dependency of the island shape, which seems unreasonable because, if so, more compact or well ordered islands would be formed if there is less time to achieve the energetically lowest configuration. One could possibly imagine that the change in He-reflectivity is due to disorder in the H overlayer. This seems, however, also impossible because of the small H cross section which cannot possibly account for such an immense change. In addition, the amount of 'visible' H vacancies is very low because the formation of such vacancies would require a reduction of the H exclusion radius. This does not seem to be the case, also with respect to the results from Mak et al. [46]. In summary, we believe that the CO-H system on Ru(0001) follows the opposite of what mean-field rate equation theory suggests.

Interestingly, the curvature of the individual TEAS measurements changes drastically (see

Fig. 4.5). For the lowest pressure applied, the TEAS-intensity follows the trend expected of a lattice gas behavior, whereas for the higher pressure, the He-reflectivity is consistent with the growth of islands. The measurements at medium pressures exhibit both features and these curves cannot be described by the fit function. The lattice gas type behavior is very surprising, since the cross section derived from this measurement is more than 3 times smaller than the one for a individual CO molecule. The smaller cross section, combined with the lattice gas behavior, suggests a high density of small ensembles of molecules with a distinct size distributed over the surface. This behavior is striking because it implies that island growth is inhibited. An average island size can be estimated as described later. In contrast to the model above, we allow \tilde{n}_i to vary and keep \tilde{n} fixed. Consequently, the small islands can be treated as individual, isolated scatterers which allows one to determine a cross section. The computation of the island cross section can be conducted as mentioned above. Instead of a circular arrangement, we have chosen a hexagonal symmetry due to the known $(\sqrt{3} \times \sqrt{3})$ R30° island formation [46,72,73] and computed only islands with relevant sizes as, e.g. $\tilde{n} = 7, 12, 19$. Due to the nature of the plot, the initial slope of He-reflectivity yields a value for the island cross section which is proportional to $1/\tilde{n}$. A comparison of the computed cross section $(\sum_{\text{theo}}^{\text{He}})$, with the experimental $(\sum_{\text{exp}}^{\text{He}})$, reveals that the mean size must be in the order of 7 molecules for $r_{\text{CO-CO}}$ =4.5 Å ($\frac{\sum_{\text{exp}}^{\text{He}}}{\tilde{a}} \approx 78.1$ Å and $\frac{\Sigma_{theo}^{He}}{\pi} \approx 78.8 \text{ Å}$).

With the theoretical cross section, we have computed a lattice gas function for a comparison to the experimental data (see Fig. 4.4). The model works quite well, especially in the low coverage regime. The excellent agreement between model and experimental data supports the growth inhibition of the small islands which was proposed above. The actual size of 7 molecules is reminiscent of a typical stable hexagonal configuration. Rosenfeld et. al [120] have studied the initial stages of growth of Pt on Pt(111). While, at temperatures below 500 K the island size increases with exposure, at higher temperatures small 'magic' clusters ($\tilde{n} = 7$) are formed which do not grow. The results are interpreted in terms of the metal-metal bond stability varying with size. While in 'magic' clusters all edge-atoms form three bonds with their neighbours, an additional 8th atom, colliding with a 'magic' cluster, can only form two bonds. At a sufficiently high temperature, the entropy will dominate and prevent clusters to reach larger sizes. As was already shown in Fig. 4.3, CO on Ru(0001) is completely disordered at coverage below 0.18. This strongly suggests that the repulsive forces between H_{ads} and CO_{ads} are well balanced, and the stability of the 'magic' size is a consequence of the high symmetry. Adding CO molecules to a 'magic' island disturbs the symmetry, which leads to an energetically less favorable configuration. The low exposure allows the system to reach thermodynamic equilibrium.

In summary, it seems that for the low exposure, small islands with a magic size of 7 molecules are formed. In contrast, the high exposure results in large islands growing with a constant island density over a broad range. The observation that small islands are already formed at very low coverage and measured at all pressures demands a very high CO mobility. Hence, CO molecules have to travel long distances to nucleate. This implies another diffusion limited process to account for the observed flux dependency.

In the limit of the 'magic' size observation, we conclude that 'magic' islands can only grow if within a time interval, the critical size is exceeded and the next larger stable configuration is achieved. This can be a process, where subsequent several single CO molecules are captured by an island, through coalescence of mobile islands of 'magic' size or by direct impingement. The first two mechanisms are unreasonable. To overcome the size regime of metastable clusters

one needs an almost simultaneous attack with several CO_{ads} upon a 'magic' cluster. Due to the low CO_{ads} concentration, this mechanism is rather unlikely and should also apply for the low–exposure experiment. A cluster coalescence mechanism has been already experimentally ruled out from the result of the low exposure experiment since there is even more time for clusters to coalesce than in the case of the high flux. The only possibility for island growth, which is in accordance with the thermodynamic considerations mentioned above, is island growth via direct impingement. Note that adsorption in the H overlayer is energetically highly improbable, as was discussed in Section 4.3.1. In this case, the slow time constant inevitably required to explain the behaviour can be related to cluster evaporation. If a 'magic' island captures a gas–phase molecule, it turns unstable and a CO molecules diffuses away. Nevertheless, this process has a certain life time because a single CO has to be dissolved into the H overlayer. Unstable islands can grow if the rate of direct impingement exceeds the rate of evaporation.

In order to check whether the time scales of the model are consistent with the uptake data, we made the following crude estimate. Starting with a surface having $\tilde{n}_i = 8 \times 10^{12} \text{cm}^{-2}$ magic clusters which act as growth initiators, the exposure time t_e to increase the cluster size by one molecule can be written as:

$$t_e = \frac{\tilde{n_i}}{S_{\tilde{n}} \cdot R} \tag{4.8}$$

where R is the flux and $S_{\tilde{n}}$ the sticking coefficient which is dependent on island size. With the simplest approximation, $S_{\bar{n}}$ is proportional to the area covered by the island if one assumes an average sticking probability S_A over the whole island. Note that island edges are more reactive, since the repulsive CO-H interaction creates an adsorbate depletion zone along the island borders which increases the attractive radius of the island by $r_{\rm ad}/2$. With $S_{\rm A}$, the average sticking probability varying between (0.3-1) (S $\sqrt{3} \approx 0.3$ [59]), $S_{\tilde{n}}$ yields 0.005–0.015 which turns out to be too low compared to the experimentally determined $S_{\text{exp}} = 0.05 \pm 0.02$. However, the CO coverage is so low (0.002 ML), that an accurate determination from Fig. 4.1 of the sticking coefficient is virtually impossible. Due to the increasing sticking coefficient with island size, the value reaches the right order of magnitude at about 0.01 ML ($\tilde{n} = 37$) which is in good agreement with the experimentally determined one. The calculation shows, that within 0.5–1.5 s, the average island size is increased by one molecule. If we assume 12 to be the first stable cluster size after 7, and account for the sticking enhancement due to increasing island sizes, it takes approximately 1.5-4.5 s to reach the second stable cluster size. If we take 2 s as a lower stability limit, with a preexponential factor ranging from 10^{-10} to 10^{-13} s, one receives a evaporation energy of 0.48-0.61 eV for CO from unstable clusters.

In the preceding paragraphs, we presented a model which is qualitatively in agreement with the experimental observation. Unfortunately, it leaves some questions of the island formation process unanswered. Firstly, we do not understand how nucleation proceeds or how growth centers initially form in an highly passivated environment. Secondly, from the data, we cannot deduce whether there is a size limit for the island stability or whether larger islands ($\tilde{n} \gg 7$) at higher coverages constantly exchange CO molecules with each other. Our model tries to explain the major observations of the anomalous behavior of island growth, but there might be other mechanisms driving the process as well. Therefore, it would be interesting to conduct other experiments like scanning tunneling microscopy (STM) and Monte Carlo simulations in combination with density functional theory (DFT) calculations to provide the final answer to the unexpected behavior of this model system.

4.4 Conclusion and summary

For the CO and H interaction on Ru(0001) we have deduced the following picture. At 250 K CO slowly displaces H. Up to 0.33 ML CO, one carbon monoxide displaces 2 H_{ads} . Above that coverage, displacement is less efficient. During displacement, CO and H form a segregate overlayer. Depending on the exposure pressure, either small islands with an average size of 7 molecules are formed, accompanied by an increase in island density at low pressure or islands grow at a constant island density over a broad coverage range. This behavior suggests that there is a growth inhibition due to strong variation in island size stability which is caused by the differences in the repulsive CO–H and CO–CO interactions. Therefore, we propose a model where initially, islands can only grow by direct impingement. In the critical regime of small clusters which are slightly larger than 7 molecules, slow evaporation of islands takes place down to a size of 7 molecules per island. This process is diffusion limited.

CHAPTER FIVE

Chapter 5

A compact molecular beam line

A new supersonic molecular beam line has been attached to an existing UHV-apparatus. Three different nozzles mounted on a rotatable manipulator allows for independent gas feeds. In this way, dosing sequences with different reactive gases can be carried out within a few minutes. Due to the compact design of the beam line, the apparatus does not forfeit its original flexibility and mobility. Apart from standard techniques like thermal desorption spectroscopy (TDS), low energy electron diffraction (LEED), reflection absorption infrared spectroscopy (RAIRS) and X-ray photoelectron/ Auger electron spectroscopy (XPS/AES), a quadrupole mass spectrometer (QMS) mounted on a linear drive and viewports allows for photochemical experiments or other laser applications.

5.1 Introduction

Molecular beam techniques are widely applied to study the dynamics of molecule— or atom-surface interactions. These experiments contribute to the understanding of reaction mechanisms occurring on surfaces. The final aim of all these studies is to unravel the precise nature of the potential energy surface on which atoms or molecules move. Once fully understood, reaction paths and rates can be predicted. Due to the multitude and complexity of the interactions between many surface atoms and the probe molecule or atom, this problem is not solvable by one experimental approach alone. In general, the information gained from scattering molecules from surfaces is a convolution of interactions with different parts of the unit cell and the different initial states of the molecule. Quantum mechanical calculations illustrate this complexity. Presently, even super—computers are still not sufficiently powerful to consider all physical quantities. However, these quantum calculations provide detailed understanding of mechanistic aspects because one is able to study -in contrast to experiments- a single set of impact conditions. Note that experimentally, even if a molecule is prepared in a single state, still the whole unit cell is probed. Nevertheless, molecular beam experiments are extremely conducive because they allow one to judge the quality of theoretical models or provide starting conditions for calculations.

To probe the dynamics of surface—molecule interactions, different experimental approaches have been applied which are well documented in literature. One attempt is for e.g. to study the behavior of the backscattered molecules or atoms. Angular distribution, energy transfer or rotational or vibrational state distributions give indirect information on the interaction potential [54,121–124]. An extension of these techniques is to investigate the interaction of molecules prepared in specific quantum states. This has been successfully accomplished for the two diatomics NO [125–128] and H₂ [129]. By means of an electrostatic hexapole, NO molecules can be oriented and one can study the reactivity of the N–end and O–end of the molecule independently [125, 126]. Further progress has been accomplished recently by McCabe et al. [130], which succeeded in the first eigenstate—resolved gas—surface studies of methane [131, 132].

Molecular beam techniques have also been used to study the thermodynamics of adsorption. By combining a molecular beam with a single crystal adsorption microcalorimeter, Borroni–Bird et al. [133] developed a technique to measure the heat of adsorption of molecules as a function of coverage.

Very often, molecular beams are also used as a 'clean' method to prepare overlayers in a very well-defined way. This is particularly advantageous when dealing with vacuum pollutive gases such as e.g. water. By means of molecular beams, the molecules impinge exclusively on the sample. This results in an instantaneous recovery of the base pressure even after long exposures. In addition when following gas-surface reactions, one can be certain that the products are formed by the sample and do not appear due to side reactions induced by e.g. hot filaments or other active metals of the UHV-apparatus.

Furthermore, by means of molecular beams adsorption states can be prepared which are inaccessible by thermal energy because of e.g. an activation barriers to adsorption. These states and their corresponding activation barriers are of particular interest, because of their relevance to heterogeneous catalysis. The knowledge of surface intermediates and their chemistry is the key to the understanding of reaction mechanisms. For this purpose, several apparatus have been designed over the past decades to combine molecular beams with standard surface techniques such as thermal desorption spectroscopy (TDS) [134–139], Auger electron spectroscopy (AES) [134–136], reflection absorption infrared spectroscopy (RAIRS) [139], low energy electron diffraction (LEED) [134–138], scanning tunneling microscopy (STM) [140] and/or electron energy loss spectroscopy (EELS) [134].

The ultimate aim of catalytic research is to understand the elementary steps of a reaction. The knowledge of the gas—surface interaction covers an important part of the catalytic process, namely adsorption and/or dissociation. However, adsorbed surface species have to react with each other before the desired product is formed. Following these surface processes in time can only be established by ultrafast pulsed lasers because these reactions usually occur in the femtosecond regime [141]. This technique is unique because one can follow the evolution of a product or the disappearance of a reactant during the reaction.

To be fully capable to study both processes, a molecular beam apparatus is required which provides both techniques and is capable to operate in a laser–laboratory. We therefore designed a compact molecular beam line and attached it to an existing UHV–apparatus that was originally constructed to study the interaction of surface adsorbates with light [142]. To retain optimal flexibility for the future our most important requirement was to be able to operate the beam–line with a combination of reactive and/or corrosive gases. Especially, fast dosing sequences with different gases should be possible with a minimum time delay between different exposures.

5.2 Design criteria

In this section we discuss criteria for the design of a molecular beam line which had to be attached to an existing UHV-apparatus described in detail elsewhere [142]. The attentive reader might ask: why modifying instead of building a whole new system?

In the first place, space limitations in the laser–laboratory do not allow the simultaneous use of two experimental setups, which logically implies that the old apparatus would have to be disassembled. The reuse of all valuable components would be logical and economic. Consequently, major parts of the new UHV–chamber might not differ substantially from the old apparatus. Furthermore, the existing design has proven to perform reasonably well which implies that the basics of the existing design would be taken over anyway. Modifying, to our opinion, is also advantageous because it requires less time for construction and manufacturing. However, a disadvantage of modifying is that the geometry of the existing experiment restricts the new design. In order to attach a molecular beam line to the UHV–chamber, the following design criteria were formulated:

- 1. Resistance against corrosive and/or aggressive gases.
- 2. A flux in the order of 1 ML/s should be achieved.
- 3. The design should allow for dosing sequences with different gases and/or gas mixtures with the least possible time delay ($\Delta t \approx 2-5$ min).
- 4. The translational energy of the beam should be variable and exhibit a narrow distribution, which should be experimentally measurable.
- 5. The design should allow for the implementation of the technique developed by King and Wells (K&W [56, 57]) to measure sticking probabilities of molecules or atoms can be implemented.

6. The molecular beam line has to fit on the existing frame of the experiment and should not substantially increase the compact size of the original experiment to retain the transportability.

- The new beam-line should not interfere with other experimental techniques like XPS/AES, RAIRS and LEED.
- 8. Furthermore, the existing TDS–setup should be replaced by a new one with higher sensitivity.
- 9. All major interior components of the molecular beam line should be accessible without breaking the vacuum of the main chamber.

In the following paragraphs, we discuss the design criteria and elucidate the problems and consequences evolving from our requirements. Relevant solutions will be presented and the practical realization will be described in the following section.

Our first and most important requirement was resistance against various aggressive gases, especially if they are used consecutively. The use of special materials, in particular corrosion resistant steels for the expansion chamber and gas lines are vital. As aggressive or corrosive gases are pollutive and a hazard to human health, its consumption should be minimized to the largest possible extent. A low gas inlet, however, is in conflict with requirement 2. This problem can be circumvented by choosing a very compact design with a short nozzle to sample surface distance, because the beam flux decreases quadratically with distance. The consequential need of a compact design imposes restrictions on the choice of pumping equipment. Generally, diffusion pumps are superior to turbo molecular pumps (TMP) because of their larger pumping speed. This is essential for a large gas inlet, required for a high-flux beam. Robustness and easy servicing also belong to their advantages. However, due to their operation principle, they can only be mounted vertically, which restricts the design geometry substantially. Furthermore, an unwanted accompaniment of diffusion pumps is needless heat production, which might perturb the homogeneity of the temperature in the laboratory, which is essential for laser stability. In contrast, turbo molecular pumps do not suffer from these disadvantages but at the expense of reliability and lower pumping efficiencies, especially for light gases. The given frame geometry combined with the limited mounting possibilities of diffusion pumps make the use of turbo molecular pumps inevitable.

Special safety cautions have to be taken to protect pump bearings and pump oil from corrosive gases. This can be realized with chemically resistant pumps, which operate with special oil and under a continuous small flow of nitrogen into the drag stage of the turbo molecular pump.

Additional complications occur if exposure procedures are carried out consecutively with different gases, that usually react with each other. To prevent chemical reactions before expansion e.g. in the gas line or nozzle, spatial separation of potential reactants is a necessity. This can be realized by either additional gas inlet systems with a separate nozzle for expansion or by spatially separated additional molecular beam lines. The latter can be dismissed because several molecular beams operating simultaneously increases the size of the whole construction as additional beams intersecting at the surface of the sample require a minimal angle in between. Nozzle design, beam shutters and chopper facilities determine the size of the solid angles, which leads to a large construction. It is more space efficient to construct multiple gas inlet systems with

several nozzles, which share the same flight path, although this enlarges the size of the expansion chamber to some extent, this seems to be the best solution for our purpose.

The implementation of the K&W-technique requires at least one inert shutter blocking the molecular beam in front of the sample surface. However, there must be an alternative possibility to hinder the beam to enter the main chamber. This would be a movable nozzle or -even better- a 2nd shutter which blocks the beam right after expansion. It is known from literature, that sticking probabilities can be extremely sensitive to surface coverage. Especially when dealing with gases with a high sticking coefficient, there should be no pre-adsorption of gas before the important part of the data has been collected. Uncertainties occur if the effusive component of the beam is large, because firstly the effusive beam unnecessarily increases the pressure in the main chamber which enhances background adsorption and secondly, the effusive component represents an unknown quantity which imposes an offset to the flux of the supersonic component. Due to different seeding and expansion conditions, the ratio between the effusive and supersonic component might not be constant. Consequently, an expendable and difficult calibration procedure has to be applied. Furthermore, the quality of the main vacuum can be affected by beams containing molecules with long vacuum time constants such as water or ammonia, because the majority of the effusive molecules/atoms miss the target surface and poison the walls of the main chamber. This problem can be reduced by an additional differentially pumped stage which in turn elongates the length of the beam line.

As can be seen from the previous discussion, one has to compromise between optimum flux and effusive beam reduction. Therefore, we have chosen for three differentially pumped stages to be able to fully exploit the power of the K&W-technique and to prevent any eventual vacuum problems. In this design, the implementation of a $2^{\rm nd}$ beam shutter within the beam line has no consequences on the flux-performance and offers the possibility to fully computer-control a K&W-measurement sequence.

Narrow translational energy distributions are mostly obtained by continuum expansion from a high–pressure gas source (nozzle) into a low ambient pressure regime. Seeding and anti–seeding techniques in combination with nozzle heating allow for variations of the translational energy of molecules/atoms between some meV and a few eV. These techniques have been proven to work reliably. In surface or gas–phase applications, pulsed valves or continuous–flow (CW) nozzles are used. Pulsed valves usually provide more beam–flux within a gas pulse but are more difficult to operate, especially at higher temperatures. Therefore, we have chosen for the more convenient and robust CW–nozzles.

Translational energy distributions can be accessed indirectly by time of flight measurements (TOF). For this purpose, a chopper wheel is required to create short gas pulses. The starting trigger for the time measurement is given by an optical sensor that registers the passing chopper slit. Dealing with neutrals the detector is consequently a quadrupole mass spectrometer (QMS) operating in pulsed counting mode. The finite spatial extent of the ionizer in combination with the quadrupole ion–optics causes additional pulse broadening. Therefore, a quadrupole mass spectrometer with a cross beam ionizer and a channeltron detector in combination with a multi–channel scaler is required and suits our design considerations best. Generally, the time resolution increases with the length of the flight path. However, the length of the flight path is limited by the size of the frame. This results in complications inherent in this type of design like a non-negligible triggering time delay ($\Delta t_{\rm trig}$), which is mainly due to the spatial separation of the optical sensor and the location where the beam passes. Furthermore, the flight time through

the ion optics adds an additional offset to the measured time. In an attempt to minimize these problems one can incorporate the chopper and trigger electronics into the beam line to elongate the length of the flight path at first instance. This has the advantageous side effect that non UHV-compatible components can be chosen, which are in general cheaper and less fragile. The geometry of the whole beam line has been chosen such, that it is possibile to have clear view to the sample along the flight path of the molecules/atoms. Consequently, triggering delays can be determined by optical means such as lasers and also sample alignment is facilitated enormously. The time delay due to the flight time (Δt_{OMS}) through the QMS causes a calibration problem. This time difference imposes a constant offset dependent on molecule/atom mass-to-charge ratio to the total flight time. $\Delta t_{\rm OMS}$ can be deduced from ions-optics simulations. Knowing $\Delta t_{\rm trig}$, $\Delta t_{\rm OMS}$ can also be determined experimentally by varying the length of the flight path. Therefore, we have chosen to mount the QMS on a linear drive to keep both possibilities. This choice permits us to employ the same QMS for TDS. To achieve maximum surface sensitivity in TDSstudies, the detector-surface distance has to be small. Furthermore, to ensure that the desorbing flux can be exclusively attributed to desorption from the surface, the ionizer has to be shielded against molecule/atom impinging from directions other than the surface. This can be realized by employing the enclosure method developed by Feulner et al. [143] in which the ionizer of the QMS is mounted in a gas enclosure with a small aperture. This method can be extended by differentially pumping the whole QMS-assembly which is advantageous if the QMS operates in the TOF-mode because no stagnation pressure in the ionizer can develop. Because the same QMS is used for TOF and TDS, the we have chosen for the extended method. The last demand on our list, can be realized by incorporating a UHV-valve between beam line and main chamber. Due to the lack of commercially available valves which would suit our purposes, we have chosen to design a mini-valve.

In the following sections we will discuss the design of the molecular beam line (section 5.3.1), TOF-techniques (section 5.3.2) and the TDS-setup (section 5.3.3). In section 5.3.4, the performance of the K&W-technique and the TDS-setup will be tested.

5.3 Implementation and Performance

5.3.1 Molecular beam line

Fig. 5.1 shows a 3–D–illustration of the molecular beam line and its facilities where the main UHV–vessel and the sample manipulator are depicted schematically. The main vacuum chamber is a cylinder which is horizontally mounted onto a frame. For simplicity, surface–sensitive techniques such as RAIRS, XPS or LEED are not depicted. They are located at the prolongation of the cylindrical chamber. The sample manipulator is represented schematically by a rod, situated in a bellow, which is mounted on an XY–stage. Because of the geometry of the existing experiment, the molecular beam has to cross the vacuum chamber perpendicular to the translation motion of the sample, with the mass spectrometer on the opposite site. To meet chemical resistance, all metal parts are made of corrosion resistant steel (SS316). The requirement of a short distance between sample and nozzle in combination with three differentially pumped stages demands that the beam line is incorporated into the main vacuum system. A prefabricated part of the beam line consisting of two stages had to be implemented into the main vacuum system. Those two stages, referred to as buffer– and chopper–stage, are separated by a mini–valve with a

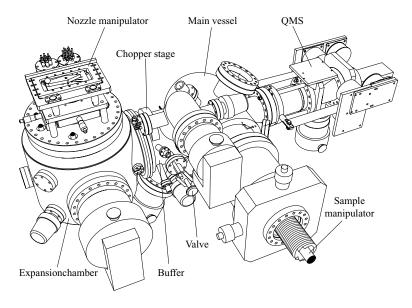


Figure 5.1: A 3–D–illustration of molecular beam line, main vessel and QMS–facility. The main vessel and sample manipulator are only drawn schematically.

slide mechanism. The buffer–stage represents a pure pumping stage, the sole aim of which is to suppress the effusive component of the beam. A connection to the main chamber is made via a small circular aperture. The chopper–stage contains a beam shutter, chopper–wheel and related electronics. The molecular beam originates from a free–jet expansion through a small orifice into vacuum. This takes place in the expansion chamber which is equipped with a multi–functional nozzle manipulator. Expansion and chopper chambers are connected by a flange which allows for easy access to all interior facilities of the beam–line. With the mini–valve shut, repairments and/or servicing of all crucial components can be conducted without breaking the vacuum of the main chamber. In line of sight with the molecular beam, a differentially pumped QMS mass spectrometer is mounted on a linear drive. The precise description of the QMS–setup is given in the following section.

The expansion chamber is pumped by a corrosion–resistant Pfeiffer TMU 520–C turbo–drag pump in combination with a Alcatel rotary vane pump (type 2063C2). Both pumps require special lubricant (Fomblin type) to properly operate under aggressive chemical conditions. Due to the high gas load into the expansion chamber, a combination of high capacity pumps has to be chosen to achieve a large flow rate through the nozzle without exceeding the critical pressure above which either the molecular beam or the pump collapse. Furthermore, optimum geometry has to be chosen to exploit the full capacity of the pumps. Therefore, the turbo–drag pump with a constant capacity of 520 ls⁻¹ (for N_2) at pressure below 5×10^{-3} mbar is mounted directly, horizontally to the expansion vessel. The pump operates reliably at a maximum pressure of 5×10^{-3} mbar for hours. As a consequence of these inconvenient operation conditions, efficient water cooling is essential due to heat evolution. The capacity of the rotary vane pump (35 m 3 h⁻¹) was chosen such that the maximum fore pressure (1 mbar) of the turbo drag pump is an order

of magnitude lower than the maximum pressure specified by the supplier. This is to minimize the power consumption and to extend the lifetimes of pump and supply. The chopper–stage is pumped by a similar combination of pumps. A low pressure is achieved by a chemically resistant Pfeiffer TMU 260C turbo–drag pump with a capacity of 190 ls $^{-1}$ backed by an additional rotary vane pump (Alcatel 2015C2, $15 \text{ m}^3\text{h}^{-1}$). For the sake of a short nozzle to surface distance, the pump could not be directly attached to the chopper stage. A 90° –elbow had to be introduced to meet spatial requirements which results in a less favorable geometry in terms of pumping efficiency. Nevertheless, with maximum gas load, the pressure does not rise above 1×10^{-5} mbar. The resulting effusive beam can be easily absorbed by the buffer chamber, which is pumped by a Pfeiffer TPU 180H turbo drag pump (180 ls $^{-1}$). Due to the low volume flow rate into this stage, the turbo–drag pump is attached to the fore-vacuum of the main chamber [142]. Under operational conditions, the pressure rises to 1×10^{-7} mbar at maximum. This is low enough to perform accurate K&W–measurements without difficult corrections, because the contribution of the effusive component to the total pressure rise in the main chamber amounts to less than 1% (see also following section).

The upper part of Fig. 5.2 shows a 2-D top view of the beam line, main vacuum chamber and QMS-assembly. The solid line (labeled with A) indicates the position of the molecular beam. In the middle panel of Fig. 5.2, a cross-section cut vertically through the beam path is plotted to illustrate interior components. A viewport, mounted perpendicularly to the molecular beam direction, provides clear view on to the sample surface. This facilitates sample and skimmer alignment and has the advantage that chopper and beam shutter performance can be checked by eye.

Working with aggressive gases demands certain safety precautions not only for man and environment, but also for the equipment. Even though all components are specified to be chemically resistant, there are always certain upper concentration limits which should not be exceeded. Therefore, simultaneous pressure monitoring of all stages is essential, in combination with a well–controlled gas inlet system. The large pressure gradient over the operating beam line demands different pressure gauges for the stages. Due to the high pressure in the expansion chamber, a Pfeiffer compact process ion gauge, with a pressure range of 10^{-6} to 1000 mbar, is mounted to the expansion stage (see Fig. 5.2). This enables one to keep track of the pressure even during an accidental pressure irruption. The pressures of buffer– and chopper–stages are measured by Pfeiffer cold cathode gauges. Decisive for this choice was the lower pressure limit of 5×10^{-11} mbar which allows to accurately judge the quality of the vacuum in the beam line with respect to the main chamber when the beam is not operated. All gauges can be controlled by a single unit. For every channel of the controller, pressure thresholds can be set, which are linked to a relay output. These outputs actuate electro–pneumatic valves placed between gas mixing cabinet and nozzles, which safeguard the maximum gas load in the individual stages.

In the lower part of Fig. 5.2, a section of the molecular beam design containing crucial components is magnified. On the left hand side, one of the nozzles situated in a radiation shield housing, is depicted schematically. Expansion and chopper chambers are separated by a stainless steel plate bolted to the flange connecting the chopper chamber. The metal–to–metal connection serves as a seal. On top of this plate, an XY–stage is mounted which carries the $1^{\rm st}$ skimmer (Beam dynamics, model 1, \emptyset = 0.5 mm) which is made of Ni. With two opposing micrometer–screws, the position of the skimmer can be aligned accurately with respect to the beam path. Presently, it is not possible to move the skimmer under vacuum but the design is such

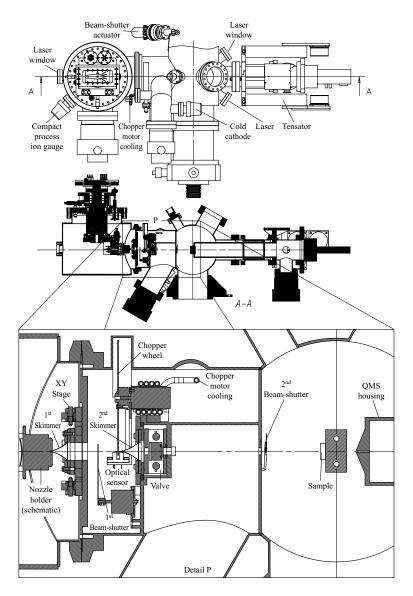


Figure 5.2: The upper part of the panel shows a top view of the molecular beam, the middle part a cross section of the side view. The cut has been made along line A. In the lower part a zoom—in of the side view is depicted. All crucial internal components of the beam line are magnified.

that skimmer manipulation from outside can be implemented quite easily. However, it turned out that due to the rigid construction the precision of the alignment was not affected by vacuum forces which rendered any efforts in this regard unnecessary. The 2^{nd} skimmer (\emptyset = 1.3 mm) is clamped between two metal rings which are bolted to the front of the mini–valve. This, together with the aperture connecting to the main chamber, determines the axis of the beam line. The positions of skimmers and nozzle determine the size of the beam spot dependent on the nozzle sample–surface distance. If the sample surface is aligned with respect to the axis of the main chamber, the nozzle to sample surface yields a distance of 330.5 mm. With these default values, a circular spot of 6 mm in diameter can be projected onto the sample surface (typically 10 mm in diameter) and allows a maximum angle between beam axis and sample normal of 55 ° with the total beam–flux still on the sample surface.

The molecular beam can be blocked by a beam shutter made of stainless steel which is actuated by a commercially available rotary soleniod. To achieve chemical resistance and to reduce degasing, minor modifications were necessary. The copper wire was substituted by one with a polyimid coating which is highly inert and does not contain unwanted plasticizer. For the body of the coil, the properties of Kapton suited the purpose. The selenoid can be switched by a external DC-voltage which allows to block or unblock the beam within less than 1 ms. Small gas pulses are provided by chopping the beam with a spinning aluminium wheel containing two slits placed opposite to each other. A large diameter was chosen to attain stable vibration-free revolutions. Therefore, the elbow-shaped chopper-chamber had to be equipped with a convexity to fit the size of the wheel. Loss in time resolution due to the finite initial pulse duration are suppressed by a 0.5% duty cycle. With a typical chopper frequency of 250 Hz, a pulse duration of 10 μ s can be achieved. The copper-wheel is driven by a three-phase brushless DC-servomotor purchased from Minimotor SA. To prevent overheating, the motor is wedged into a copper pipe surrounded by copper tubings, which is connected to a coiling water circuit (see also upper part of Fig. 5.2). The trigger for the instrument of the TOF measurement is supplied by a transmissive optical sensor (TCSS1100/2100) mounted under a 10° angle with respect to the beam axis. The internal Schmitt-trigger of the component leads to an acceptable rise time of 50 ns, which is much faster than the time resolution of the TOF-measurement.

A small additional compartment behind the 2^{nd} skimmer contains the mini-valve. The internal vacuum seal is made by pressing a metal plate onto a Teflon-based O-ring. Metal springs provide the necessary sealing pressure enforced by the ambient pressure when the chopper-stage is pressurized. The valve can be opened and shut by a push/pull actuator with a position lock.

The 2nd beam shutter, located in the main chamber, consists of an inert, transparent mica plate clamped on a steel holder connected to a metal cantilever arm, which can be actuated from outside the vacuum by a rotary drive (see also upper part of Fig. 5.2). The motion of the beam shutter is automatized by a rotary selenoid attached to the rotary drive. Short opening and closing times are achieved by applying a pulsed electrical current.

The nozzle-manipulator represents the heart of the new beam line (Fig. 5.3). It unifies three individually functioning nozzles-assemblies, equipped with heating facilities and separate gas supplies. A massive stainless steel block, mounted on a rotary drive, serves as a carrier for the three nozzle-assemblies. A rotary drive is situated in a bellow which is mounted into a wide bore XY-translation stage. Two cross roller-bearing slides on top of the XY-stage are mounted to compensate for torque forces induced by the long bellow. The Z-motion can be manipulated by a spindle nut. A travel range of 25 mm for all motions is sufficient to position the nozzle

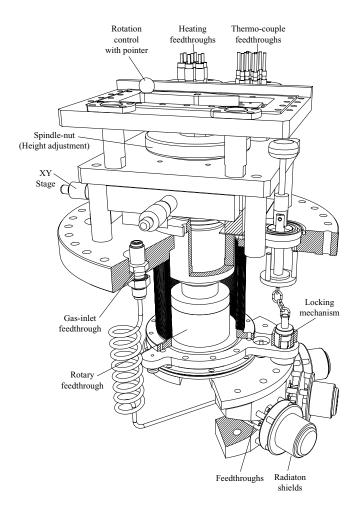


Figure 5.3: Drawing of the nozzle manipulator. Nozzles and nozzle-heating facilities are hidden under the radiation shields.

in front of the skimmer with high precision. Individual settings for different nozzles can be reproduced reliably.

The rotational movement is restricted to 5 fixed positions by a locking mechanism. A pointer on top of the manipulator indicates which nozzle is in front of the skimmer. The bisecting lines of the angles between two nozzle–assemblies define two special positions with a clear view on to the sample along the beam axis through bores drilled into the steel block (see also Fig. 5.4).

A center–pin, kept in position by a metal spring, locks the rotational motion. To rotate the manipulator, the center–pin, connected by a chain to a push/pull–drive has to be retracted. The fragile skimmer is protected against mechanical damage which might occur during rotation. To prevent the push/pull–drive to be actuated while the X–drive is not in its maximum outer position, an aluminium plate is mounted on the bottom of the XY–stage .

Spatial limitations on the steel block constrict the design of the nozzle-assembly. Heating filaments, thermocouples, electrical connections, gas feed and radiation shields have to be realized within a few cubic centimeters. As determined by the geometry, electrical connections and gas-lines have to be made from the backside of the steel block. Consequently, a straight in-line nozzle was chosen to meet these spatial requirements. Nozzles consist of a W-tips joint to Mo-tubes. A gas-leak-tight junction is realized by e -beam welding. The tips made from a tungsten rod are hollowed out from one side by spark-erosion. For the different nozzles, orifice diameters between 50 and 80 µm are chosen and fabricated by a commercial workshop. The Motube have been brazed into a stainless steel cup connected to the gas line which also serves as a nozzle-holder. This holder is bolted to the back of the stainless-steel block (see Fig. 5.4) in such a way that the nozzle extends to the opposite side through a bore. Four feedthroughs centered around the nozzle serve as mounts for filaments and electron bombardement targets. Nozzles are heated indirectly by thermal radiation from a hot tantalum tube which is bombarded by electrons provided by two thoriated-tungsten filaments placed perpendicular to the tube. Small cups of thin tantalum foils surround all hot parts and serve as radiation shields. C-type thermocouples, spot-welded on each tip of the nozzles, form the basis for electronic temperature control. Under maximum gas load, nozzle temperatures up to 2000 K can be easily achieved by a filament current of 9 A and a bias voltage of 600 V on the Ta-tube.

In most molecular beams studies, seeding techniques are used to vary the translational energy of the beam. This requires mixing of different gases with well–defined ratios. By chemically resistant mass–flow controllers (Bronkhorst F-201C-FA-11-Z), located in a separate gas cabinet, total volume–flow rates and mixing ratios can be adjusted, which guarantees reproducible beam–energies and –fluxes. Stagnation pressures behind nozzles are monitored by single–ended pressure transducers (MKS-700-series). A 15 μ m particle filter placed on the gas–line vacuum connector protects the nozzles from clogging. The gas–feed can be interrupted by three electro–pneumatic valves, placed outside vacuum and close to the nozzles. Additional manual toggle valves connecting gas–lines and a rotary vane pump form individual by–passes for each nozzle. A by–pass is used to pump the remaining gas behind the nozzle after the gas–feed has been stopped. Afterwards, a different nozzle can be operated. Typically within a few minutes, the new beam has stabilized and the experiment can proceed. This is fast enough to expose the sample to different gas mixtures in a controlled and reproducible manner and fulfills requirement 3 satisfyingly.

Let us focus on the beam performance. A crucial quality feature of a molecular beam line is the maximum achievable flux. With the current setup, the flux can not be directly measured

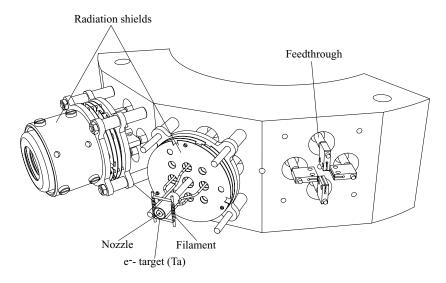


Figure 5.4: Drawing of the nozzle holder. The left nozzle–assembly is complete. From the middle nozzle, the radiation shields are taken off to illustrate heating devices. The right assembly shows the copper supports for the filaments and the electron beam target.

but it can be estimated. This quality check was carried out using a beam consisting of 2% O₂ seeded in He with O₂ as a test gas. The number of molecules can be computed assuming ideal gas behavior. The flux $\frac{dn}{dt}$ is given by

$$\frac{dn}{dt} \approx \frac{\Delta pS}{k_B T} \tag{5.1}$$

with S the pumping speed for oxygen, T the temperature of the system, k_B Boltzmann's constant and Δp the pressure rise induced by oxygen. The partial oxygen pressure can be determined by calibrating the QMS–reading against the ionization gauge of the main chamber which has to be corrected for the O_2 –ionization probability (supplied by the manufacturer). For the pumping speed S, we took 450 ls⁻¹ as specified by the supplier of the TMP of the main chamber. The corrected oxygen–induced pressure rise yielded 7×10^{-9} mbar. This results in a flux of approximately 0.18 ML s⁻¹, which is acceptable with respect to the chosen seeding ratio.

5.3.2 Beam detection and TOF-techniques

In the line—of—sight of the molecular beam, a quadrupole mass spectrometer (QMS) mounted on a linear drive serves as a time of flight detector. This could only be realized by removing the sample exchange mechanism of the old design. Consequently, sample exchange without breaking the vacuum is no longer possible. To turn a disadvantage into an advantage, we therefore modified the relatively complicated sample—holder. Refinements and resulting advantages are described in the following section. The mass spectrometer was especially manufactured for our purposes. Its design is based on the Balzers QMA400—model but possesses, instead of a 90 ° off—axis detector, an inline arrangement for detection. Molecules or atoms are ionized by a cross—beam ionizer.

The mass filter consisting of 200 mm long Mo-rods and 8 mm in diameter, combined with a 2.25 Mhz radio-frequency generator, allows for a mass range up to 511 AMU. Ion optics, emission and extraction voltages are computer-controlled. Thereby, optimum settings for TOF measurements can be found easily. A channeltron (Burle-type 4870V) provides sharp pulses with a typical duration of 5 ns which allows for single ion counting. The pulses are amplified and height-selected by a home-built pulse shape amplifier and fed to a multi-channel scaler (MCS), purchased from EG&G (Turbo MCS). The quadrupole mass analyzer is situated in a stainless steel housing, which is differentially pumped by a Pfeiffer turbo-drag pump (TPU062H, 56 ls⁻¹). To improve pumping speed and reduce back diffusion of especially hydrogen into the QMS-housing vacuum, the turbo-drag pump is connected in series with a second pump of the same type which is backed by a Balzers MD4TC diaphragm pump. A performance test revealed that the pumping speed quintuples (measured for Ar). A stainless steel cup with a small orifice $(\emptyset = 3.5 \text{ mm})$, bolted to the QMS-housing, shields the cross-beam ionizer from molecules/atoms which do not impinge into the ionization volume along the beam axis. The upper and the middle parts of Fig. 5.2 show the top and side view of the OMS-assembly, which is suspended from the main frame via a YZ-stage (not depicted). Thereby, the QMS can be aligned with respect to the beam axis. A bellow provides the necessary flexibility and a translation range of 200 mm. To move the QMS along the beam axis, a linear drive is mounted to the YZ-stage which supports the QMS-assembly and the bellow connecting to the main chamber. The linear motion is driven by a worm shaft mechanism and guided by cross-roller bearing slides. By this means, reproducible positioning of the QMS with high precision is guaranteed. TOF measurements can be conducted with a variable flight path ranging from 266 to 466 mm. Note that the flight path is determined by the distance between chopper wheel and QMS-ionizer. For laser desorption or photodissociation experiments two quartz viewports are mounted to the left and right hand side of the QMSassembly. Under specular conditions, laser-light impinges under an 37.5 o angle with respect to the surface normal. Desorbing molecules can be detected under any angle by rotating the crystal. The orifice of the differentially pumped QMS-housing allows for angular resolutions between 1 and 4° dependent on the flight length. For time resolved measurements, the length of the flight path can be adjusted between 55 and 200 mm, where the limits are determined by the size of the OMS-housing and the translation range of the linear drive.

5.3.3 Thermal desorption facilities

As can be seen from the lower part of Fig. 5.2, the QMS-assembly can easily reach the center of the main chamber which also represents the rotation axis of the sample when performing angular-dependent molecular beam experiments. This allows one to utilize the QMS for TDS-studies. Furthermore, due to the differential pumping, angular-dependent thermal desorption studies become possible. Because of the long translation range of the QMS-assembly, a very small sample-surface to detector distance can be achieved, which provides a very high surface sensitivity because the majority of the desorbing flux is detected. Due to the fact that molecular beam and QMS-motion are aligned on one axis, measurement sequences are extremely straightforward. Overlayers prepared with the molecular beam can rapidly be investigated by TDS, simply by rotating the sample by 180° and inserting the QMS. The high precision of the QMS-translation motion and sample rotation leads to reliable and reproducible measurements.

With the original design of the sample manipulator, three samples could be used simultaneously. Individual sample holders could be transferred from a storage system to the target head.

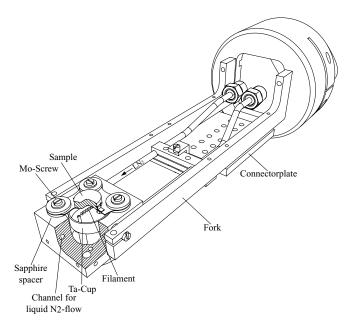


Figure 5.5: 3–D–illustration of the sample holder. The sample is clamped onto a Ta–plate isolated by sapphire spacers. The copper block serves as a heat exchanger and support. The heating filament situated in a Ta–cup is visualized by a cut through sample and copper block.

The rod of the manipulator served as a support for both storage holders and target head. As a consequence, a fairly bulky construction had to be moved through vacuum with high risk to crash into analytical tools. Due to spatial limitations, the magnetic transfer arm providing sample exchange had to be replaced by the QMS-assembly, which offered the opportunity to design a new sample holder, which meets lower requirements but features more robust properties.

A 3D-assembly drawing of the newly designed sample holder is depicted in Fig. 5.5. A copper block with a 25 mm bore in the center forms the base for sample and filament support. It is suspended by a stainless steel fork, which is bolted to the rod of the manipulator (only schematically drawn). All electrical connections are guided through this rod to feedthroughs located at the end of the manipulator. A ceramic plate placed between the two prongs serves as a connector socket for thermocouple, high voltage and filament wiring and provides the necessary strain-relief. The copper-block possesses a U-shaped channel around the center-bore which is extended on both sides by copper tubes. By this means, the copper-block acts as a heatexchanger. The liquid nitrogen is supplied to the heat exchanger through stainless steel tubes which run from the end of the manipulator through the center of the rod. To maintain flexibility and easy servicing, a metal gasket face seal fitting (cajon) located above the ceramic plate socket forms the connection between copper-block and stainless steel tubes. A junction, leak-tight at cryogenic temperatures, between copper and steel (fitting) is established by brazing (silver). During experiments, a continuous liquid nitrogen flow is applied, which results in a minimum temperature of 78 K. The samples, usually cylindrical with a typical diameter of 10 mm and thickness of 3 mm, is fixed to a Ta-plate (thickness 0.4 mm) by Ta-clamps. Plate and sample

holder are electrically insulated by sapphire spacers and are bolted together with four Mo-screws. Sapphire has been chosen as insulating material because of its thermal conductivity properties. Sapphire, also known as a thermal diode, conducts heat at low temperatures very well whereas at high temperatures the thermal conductivity is low. Sample heating is provided from the back by a thoriated W-filament. Radiative heating as well as electron bombardement is possible.

A Ta-cup containing the filament serves as a heat screen and prevents electron bombardement of the copper block. The filament is supported by two Ti-pins, which extend through a ceramic plate. By this means, the filament assembly is enclosed into the cold copper-block. Therefore, radiative heat losses from the filament are absorbed by the cryostat, which prevents unnecessary heating of the environment accompanied by degasing. Filaments, produced by wrapping a thoriated W-wire (1% Th, $\emptyset = 0.2$ mm) around an unfolded paper-clip, are spot-welded to the Ti-pins. For electron bombardement, a high-voltage (600-1000 V) can be applied to the Ta-plate containing the sample. Maximum emission currents of more than 80 mA (U > 600 V) can be achieved easily. Corresponding filament currents typically range between 3 and 5 A, dependent on the degree of degradation of the Th-content of the filament. This leads to a heating power in the order of 120 W. Sample temperatures are measured by either C- or K-type thermocouples which are spot-welded or glued to one side of the sample. In the case of conductive samples, the thermocouple signal has to be decoupled from the bias-voltage applied to the Ta-plate before being analyzed. Even though special integrated circuits are available to process small thermo-voltages, they only function with a single thermocouple-type. Consequently, changing the thermocouple type requires another type of circuit. Another option are standard PID-controllers which usually operate with many thermocouple types. Unfortunately, they are usually not equipped with isolated inputs which allow high offset voltages. Our solution to this problem is to pre-amplify the thermocouple voltage by an operational amplifier (op-amp, type BB OPA627AM), followed by an isolation amplifier (AD 210). Offset and gain can be adjusted manually by potentiometers. Long-term-stability and linearity of the electronic circuit was tested carefully. To our surprise, over months of operation, no measurable drift of offset or gain could be detected. To measure absolute temperatures, cold junction compensation is required, which is realized by an ordinary ice bath. The reference thermocouple is embedded into a ceramic which provides the necessary electric insulation required for safety during operation. The output of the isolation amplifier is connected to a Eurotherm 905S temperature controller, which regulates the sample-temperature by adjusting the filament current. A two point temperature calibration against liquid nitrogen and boiling water was carried out to ensure the right T-readout of the Euroterm.

Fig. 5.6 illustrates the performance of the new sample holder. The plot shows a heating—cooling cycle of a Pt(533) crystal with a K–type thermocouple serving as a temperature probe. To reach cryogenic temperatures, liquid nitrogen is flown continuously through the manipulator and sample holder. By this means, a minimum temperature of approximately 78 K can be reached. After 35 s, the crystal is heated to 1273 K with maximum output power (\approx 120 W) and subsequently cooled down. Within 25 s the desired temperature is reached which leads to an average temperature rise of 40 Ks⁻¹. The shape of the heating curve clearly indicates that there is heating power in excess and much higher temperatures can be attained. A crucial quality feature of a sample holder is to allow for high sample–temperatures at low pressures which guarantees clean conditions for experiments. During the heating of the Pt(533) crystal, the base–pressure of the chamber remained below 3×10^{-10} mbar at maximum temperature and

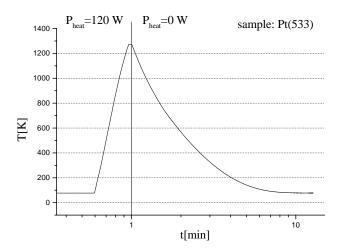


Figure 5.6: Performance test of the cryostatic properties of the sample holder. A Pt(533) crystal was heated with ≈ 120 W to 1273 K and subsequently cooled down to liquid nitrogen temperature. The crystal temperature measured with a K-type thermocouple spot—welded to the side of the crystal was monitored with time.

recovered to 1×10^{-10} mbar instantaneously after the filament was switched off. Due to the finite base–pressure, the experimental temperature should be reached within some minutes to prevent background adsorption from the residual gas. The cooling characteristics of the Pt(533) crystal proves that the target head of the sample–manipulator also meets this requirement. Cooling from maximum to minimum temperature takes only 8 min.

Clearly, when cooling or heating, Ta-plate and sample have the same temperature. This might lead to experimental problems if one studies physisorbed overlayers by TDS, because desorbing molecules/atoms can not be attributed exclusively to desorption from the sample surface alone. However, surface sensitivity is guaranteed because of the small orifice of the differentially pumped QMS-housing. With an appropriate surface-detector distance, desorption from the Ta-plate should not contribute to the signal.

5.3.4 Performance test of K&W and TDS-facilities

The performance of the TDS-setup was tested by desorbing CO and H_2 from a Pt(533) single crystal. Hydrogen and carbon monoxide were our candidates of choice because of their occurrence in connection with hot metals. Overlayers were prepared by backfilling the vacuum chamber with a constant H_2/CO -pressure instead of applying molecular beam techniques to ensure that the back of the crystal and sample mount are heavily contaminated with CO or H_2 . This procedure allows to judge the quality of the differential pumping and the surface-sensitivity of the setup. The results of the two TDS-experiments are depicted in Fig. 5.7. In both experiments, the Pt(533)-crystal was saturated with the respective gas and ramped with 7 Ks⁻¹. To maximize

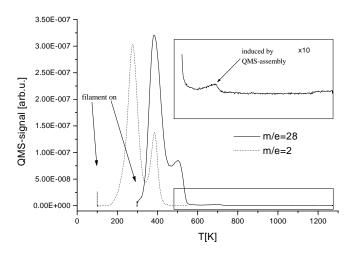


Figure 5.7: Quality check of the TDS–setup. Desorption from the stepped Pt(533) surface results in two desorption states for Ptaure H(1) (dotted line) and Ptaure H(1) (solid line). Overlayers have been prepared by saturating the surface with either Ptaure H(1) at 78 K or CO at 300 K. The small CO peak at 680 K is due to degasing induced by radiative heating of the Ptaure H(1) (solid line).

the signal and to fully exploit the effect of differential pumping, the distance between the orifice of the QMS-housing and crystal was set to 2 mm. Despite these optimum settings, the pressure rise, induced by the hot filament, is still visible in the spectrum. However, these spikes are very small compared to the actual signal. Both curves exhibit a double peak structure, which can be explained in terms of two different desorption states. While the peak at higher temperature can be attributed to desorption from step edges, the lower one originates from terrace sites. Both results are in accordance with literature [144, 145]. In the case of CO, the low intensity of the hightemperature species might be indicative for some contaminated step sites. Nevertheless, high surface quality is not indispensable for these kind of quality checks. From the measurements, an average signal-to-noise ratio can be determined which is in the order of 2000. This ratio guarantees the detection of very small fractional coverages of adsorbed species. In the CO-TDS, an additional very weak feature occurs at 700 K. A zoom-in is plotted in the inset to illustrate the contribution of the small peak with respect to the total signal and the noise level. Further tests revealed that the appearance of this small desorption signal is induced by the setup itself. The precise nature of this measurement artefact is not yet fully understood. Possibly, small amounts of CO adsorbed on the QMS-cup and/or its surroundings desorb due to radiative heating induced by the crystal. The usage of a quartz instead of metal QMS-housing might solve this problem. However, the contribution of the small signal to the total desorbing flux is so small (<0.5%) that a modification is not necessary. The detection of such a small desorption peak illustrates the excellent performance and high sensitivity of the setup.

A performance test of the K&W technique is depicted in Fig. 5.8. Here, the initial sticking probability of O_2 on a Pt(533) surface(T_s =295 K) is measured at normal incidence. A mixture of

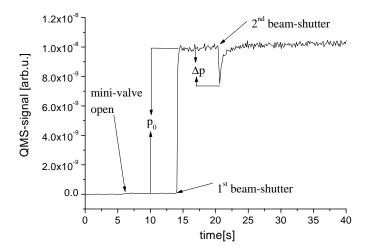


Figure 5.8: K&W-performance test. A Pt(533)-crystal (T_s =295 K) serves as a target for an oxygen beam. The oxygen QMS-signal is plotted versus time. The small effusive component of the beam becomes visible after opening of the mini-valve. Opening the 1st beam shutter allows the beam to enter the main chamber indicated by the pressure rise p_0 . Δp is a consequence of the dissociative adsorption of oxygen on the surface.

2% O₂ in He was expanded into the vacuum of the expansion chamber with mini-valve and both beam-shutters closed. With the nozzle kept at room temperature, this results in a translational energy of E_i =0.43 eV. In the main chamber, the partial oxygen–pressure is monitored by a QMS different from the differentially pumped. As can be seen from Fig. 5.8, opening the mini-valve leads to a very small increase in O_2 -pressure. After opening the 1st beam shutter, the O_2 -beam is allowed to enter the main chamber, but it does not impinge on the sample. Actuating the 1st beam-shutter also influences the pressure in the buffer chamber. A small increase can be observed as a result of the not perfect point-shape like acting nozzle. Note that for geometrical reasons, the beam spread changes with nozzle-skimmer distance and the size of the nozzle. Depending on the experimental conditions, the aperture limits the edges of the beam which results in a small pressure increase in the buffer chamber. The partial oxygen pressure in the buffer chamber determines the magnitude of the effusive component of the molecular beam. This small effusive background can be rescaled to the situation where the beam enters the main chamber and compared to the total pressure rise induced by the beam. A value of less than 1% for the effusive component is found. This is small enough to determine sticking probabilities accurately. When the 2nd shutter is opened, the Pt(533) crystal acts as a virtual pump which can be seen by the instantaneous O₂ pressure drop. After a couple of seconds, the surface is saturated with oxygen. The initial sticking probability S_0 can be computed to be

$$S_0 = \frac{\Delta p}{p_0} \tag{5.2}$$

with the explanations of Δp and p_0 given in Fig. 5.8.

In the case of the Pt(533) crystal, a value for the initial sticking probability of energetic oxygen ($E_i \approx 0.4 \text{ eV}$) of 0.25 is found. This value is slightly higher than on the Pt(111) surface [146]. Note that the structure of the (111) surface resembles the structure of terraces of the stepped Pt(533).

5.3.5 TOF calibration and beam energies

To determine the mean energy of a molecular beam expanded from a CW-nozzle, the beam has to be chopped into pulses by a chopper wheel with a short duty cycle. Creating short pulses is advantageous because measured TOF-distributions are convoluted with the chopper slit function. Clearly, if long duty cycles are applied, the chopper function dominates the TOF-spectrum and only the rising and falling edge of the measured gas pulse contains the shape of the TOFdistribution. To measure the shape of the TOF-distribution accurately and to facilitate the fitting procedure the broadening of the TOF-distribution induced by the chopper can be reduced by small slits and by operating the chopper at high velocities. In our case, the beam is therefore modulated by a chopper with a 0.5% duty cycle at 250 Hz. The mechanical modulation of the beam in combination with the QMS-detection method causes some calibration problems because the point of time at which the beam passes the chopper slit is unknown on the measured time scale. This is caused by the fact that the trigger pulse generated by the optical sensor does not coincide with the pulse of molecules/atoms produced by the chopper wheel. In addition, the detection method of the molecules or atoms by a QMS adds an additional offset to the total flight time because the ionizer and not the multiplier of the QMS represents the arrival point of the flight distance of the neutral species. The total mean flight time t_{total} therefore composes of the following contributions:

$$t_{\text{total}} = t_{\text{TOF}} + \Delta t_{\text{trig}} + \Delta t_{\text{elec}} + \Delta t_{\text{OMS}}$$
 (5.3)

where t_{TOF} is the mean flight time; this is the sought value from which one can compute the mean translational energy. $\Delta t_{\rm trig}$ and $\Delta t_{\rm OMS}$ are offsets caused by the way of triggering ($\Delta t_{\rm trig}$) and the time delay in the QMS ($\Delta t_{\rm OMS}$). For the sake of accuracy, we assume an additional offset $\Delta t_{\rm elec}$ which might be caused by electronic delays of the optical sensor or the MCS. Since the QMS-detector can be moved along the beam axis, the flight distance s from chopper to detector can be varied from 266 to 466 mm. Therefore, t_{total} can be measured as a function of s. By linear extrapolation of t_{total} to s=0 mm, the sum of all time delays $\Delta t_{\text{trig}} + \Delta t_{\text{elec}} + \Delta t_{\text{OMS}}$ can be derived. This method has been applied to an oxygen beam (2% O₂/He) for various chopper frequencies. The results are depicted in Fig. 5.9 (left panel). Different chopper velocities are given in terms of the time between two consecutive slit passages $\frac{1}{2}\tau_{chopper}$. Clearly, all lines have to be parallel because the slopes of the linear fits are equivalent to the reciprocal value of the mean velocity. Note that knowing the total delay is already sufficient to fit TOF-spectra. However, it is important to determine all contributions separately, especially their dependencies on chopper frequency, molecular/atomic mass and QMS-settings, to be able to judge the quality and reproducibility of the measurement. Furthermore, the knowledge of Δt_{OMS} is important for calibrating the absolute time axis of photo–dissociation experiments.

As is evident from the plot (Fig. 5.9 (left panel)) the direction of rotation of the chopper with respect to the position of the optical sensor is such that the trigger event precedes the intersection of the chopper slit with the molecular beam. This is because the total mean flight time increases

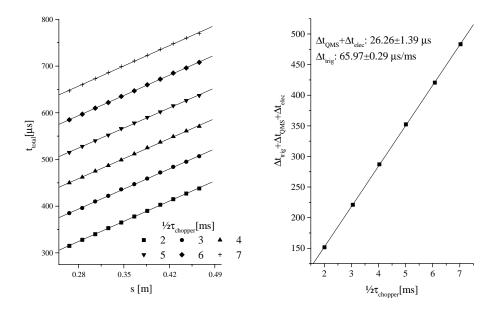


Figure 5.9: Left panel: The total mean flight time of an O_2 -beam seeded in He, plotted as a function of the chopper-QMS distance s. Data has been taken at various chopper frequencies. $\frac{1}{2}\tau_{\text{chopper}}$ denotes the time difference between two consecutive slit passages. Solid lines are linear fits through the data points. The intercepts with the y-axis yield the sums of trigger, QMS and electronic time delay denoted as Δt_{trig} , Δt_{QMS} and Δt_{elec} , respectively. Right panel: Sum of time delays plotted as a function of $\frac{1}{2}\tau_{\text{chopper}}$. The solid line is a linear fit through the data points. The intercept with the y-axis denotes the sum of Δt_{elec} and Δt_{QMS} ; the slope multiplied by $\frac{1}{2}\tau_{\text{chopper}}$ equals the trigger time delay Δt_{trig} .

with decreasing chopper velocity. The time delays at s=0 mm for the different chopper periods can be plotted as a function of $\frac{1}{2}\tau_{\text{chopper}}$ (see Fig. 5.9 right panel). As the trigger delay is proportional to the trigger period, the intercept of a linear fit yields the sum of the flight time through the QMS for oxygen and the electronic delay. The slope yields the trigger delay divided by the chopper period. Consequently, the contribution of Δt_{trig} can be separated from $\Delta t_{\text{QMS}} + \Delta t_{\text{elec}}$. If this procedure is repeated for molecules/atoms with large differences in molecular/atomic mass, one can distinguish between Δt_{QMS} and Δt_{elec} because the flight time through the QMS is m/e–dependent. In an ideal in–line QMS, ionized molecules or atoms are extracted from the ionizer volume by a DC voltage. This acceleration results in a constant ion velocity. After having passed the mass filter the ion hits the detector, resulting in a current pulse which is electronically modified and fed to the MCS board. Neglecting all accelerating and decelerating effects induced by the ion optics of the QMS, it can be easily shown that Δt_{QMS} is proportional to the square root of the mass—to—charge ratio ($(\frac{m}{e})^{\frac{1}{2}}$). To determine the flight time through the QMS, time delays for singly— and doubly—charged ions of Xe, Ar, O₂, He and CH₄ have been measured. Results are

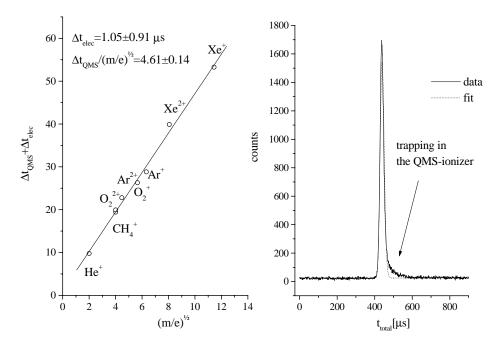


Figure 5.10: Left panel: Sum of electronic and QMS time delay are plotted against the $(m/e)^{\frac{1}{2}}$ for various ions. A linear fit yields the electronic time delays $\Delta t_{\rm elec}$ and the flight time through the QMS. Right panel: Time of flight distribution of an O_2 beam seeded in He (solid line). The x-axis denotes the total flight time in μ s, the y-axis the number of counted ions (m/e=32). A shifted Maxwell–Boltzmann distribution convoluted over the finite chopper width is fitted to the data points and shown as a dotted line. The deviation between fit and data points is probably due to trapping of molecules in the QMS-ionizer.

depicted in Fig. 5.10 (left panel). A linear fit through the data points yields a value for the intercept equivalent to $\Delta t_{\rm elec}$ of approximated $1.05\pm0.91~\mu s$. Note that the scatter in the data points is not due to statistical noise: the error bars on the data points are smaller than the size of the data points. The deviation from the linear behavior is a consequence of the ad hoc assumption that the QMS acts as a linear accelerator. The scatter and especially the linearity of the data strongly depends on the settings of the ion optics. In our study, optimum settings have been chosen to minimize $\Delta t_{\rm OMS}$ while retaining mass resolution and high transmission.

With the time delays determined, one can now fit the TOF-distribution to a shifted Maxwell-Boltzmann distribution (see Equation 1.2) convoluted over the finite slit width [81] of the chopper. An example of an TOF-measurement performed with an O₂ beam (2% O₂ in He, T_n =300 K) is given in Fig. 5.10 (right panel). Raw data are represented as a solid line. The corresponding fit, indicated as a dotted line, yields a mean energy of 0.43 eV with an energy dispersion of $\frac{\Delta \Delta E}{E} \approx 16\%$. This is sufficiently low to conduct energy resolved measurements. The deviation between fit and data at the high t_{TOF} -edge of the distribution is most probably due to trapping of molecules in the ionizer of the QMS which causes a pump tail. To judge the quality and accuracy

of the TOF–setup, the experimental value of the mean energy can be compared to the theoretical which can be computed assuming ideal behavior. The theoretical energy E_{theo} is given by [19]:

$$E_{\text{theo}} = \frac{5}{2} \left(\frac{m_{\text{O}_2}}{X_{\text{O}_2} m_{\text{O}_2} + X_{\text{He}} m_{\text{He}}} \right) k_{\text{B}} T_{\text{n}}$$
 (5.4)

where T_n is the nozzle temperature, k_B is the Boltzmann constant, X is the mole fraction and m is the molecular/atomic mass. The computation yields a value for E_{theo} of 0.45 eV, which is about 4.6% higher than the measured one. To illustrate the origin of this deviation, it is instructive to focus on the velocities instead of the energies. In the ideal case, He atoms and O₂ molecules travel with an identical mean velocity v_{theo} of 1653 ms⁻¹. This value compares well to the He velocity $(v_{He}=1650~{\rm ms}^{-1})$ determined experimentally for the same beam. However, O₂ molecules are slightly slower (Δv =-29 ms⁻¹) than the He atoms. This effect is also known as the velocity slip which is due to non–ideal behavior of the expansion mixture [19], and accounts for the energy reduction of 4.6%. In essence, the results indicate that the calibration procedure yields the correct mean energies.

5.4 Conclusion and summary

In summary, we have designed a compact corrosion—resistant supersonic molecular beam line, which has been attached to an existing UHV apparatus. Supersonic molecular beams are created by gas expansion from one of three independently operating nozzles. This allows us to perform dosing sequences with different reactive gases within short time intervals. Due to the compact size of the molecular beam line, the size of the setup could remain limited so that the flexibility and mobility of the existing setup could be retained. A movable QMS provides sensitive TDS—measurements and determination of the beam energy. Two viewports provide the necessary optical access for laser light enabling future photochemical and/or other laser experiments.

88 Chapter six

Chapter 6

Dissociative adsorption of methane on Pt(533)

The influence of well-defined steps on the dynamics of dissociative chemisorption of methane on Pt(533) has been investigated using molecular beam techniques. The initial dissociative chemisorption probability S_0 has been determined as a function of incident energy E_i , angle of incidence θ_i and surface temperature T_s . A simple geometric model has been employed to discriminate between the chemisorption probabilities at the (100)-steps and at the (111)-terraces. Steps appear to be more reactive in cleaving the C–H bond. In the measured energy range (100 $< E_i < 1450$ meV) the reaction channel associated with steps can be considered as a direct mechanism whereby molecules dissociate immediately upon impact with the surface .

90 Chapter six

6.1 Introduction

Stepped surface are particularly interesting to study, because compared to flat surfaces, they offer adsorption and reaction sites with less coordinated metal atoms. For these reasons, it is generally assumed that reactants and products are more strongly bound to the surface which results in a lower activation barrier and possibly a higher reactivity. The relationship between the binding energy of the products and the activation energy is also known as the Brønsted–Polanyi relation.

The validity of this empirical rule has been verified on a microscopic basis by quantum calculations for some systems. A good qualitative agreement was found for e.g. NO dissociation on Pd(211) [147]. In accordance with the Brønsted–Polanyi relation (see e.g. [148]), the lower barrier calculated at the step edge could be attributed to the stronger binding of N_{ads} and O_{ads} to the step. Similar observations have been made for NO dissociation on a stepped Ru(0001) surface. It was concluded that the stronger binding energies are due to the lower coordination number of the step atoms which causes energetically high local d-band centers responsible for the locally higher reactivity. In addition, the step–bound transition state configuration is more stable compared to the terraces–bound configuration because more surface atoms are involved in the transition state at the step which reduces the surface–mediated repulsion caused by the evolving products [149].

Even though this ad hoc argumentation appears to be in agreement with many surface reaction, the instructive model often fails on a microscopic basis. For instance, the assumption that less coordinated metal atoms occuring at steps or defects exhibit a stronger chemical potential is not always valid. For instance, the presence of steps on a Rh(100) surface has very little influence on the NH₃ heat of adsorption [150]. Moreover, the NO adsorption and dissociation on a stepped Rh(533) surface was found to proceed mainly on terrace sites at low coverages ($\theta < 0.25$) [151].

A good example for the short–comings of the Brønsted–Polanyi relation is the dissociation of nitrogen on stepped Ru(0001). The activation energy for the N–N bond cleavage at steps is in the order of 0.4 eV which is substantially lower compared to 1.3 eV on the terraces. However, the adsorption energies of the product N_{ads} do not reflect this strong reduction in barrier height. The lowering of the barrier height was attributed to differences in transition state geometries and electronic effects [152].

As shown above, the presence of steps enriches surface reactions by offering reactants new and additional reaction paths. The relevance of these paths is determined by the dynamics of molecule—surface interactions. Even though theory (density functional theory (DFT)) might predict a minimum energy path it might not be accessible because the process is dynamic and the coupling efficiency of the available energy into the reaction coordinate determines the probability whether a certain reaction path is traversed or not.

For instance, the (100)–steps of Pt(533) surface offer a low energetic route to dissociation of hydrogen which is only accessed by molecules with a low translational energy. At high incident energy hydrogen is dissociated on terraces via a direct reaction mechanism [145]. In contrast, oxygen on the same surface dissociates via a step–mediated reaction mechanism over the whole energy range [153].

A strong dependency of the reaction mechanism upon reaction conditions has also been observed for CO oxidation on Pt(113) [154]. While at low CO pressures the oxidation primarily occurs on terraces, above a critical pressure CO_2 formation switches from terrace sites to step sites. In this case, the switching could be attributed to a change in the rate limiting reaction step.

With this in mind we have studied the influence of steps on the dissociative chemisorption

PROBING BOND BREAKING 91

of methane on Pt(533) by molecular beam techniques. The surface structure of Pt(533) consists of four atom long (111)–terraces and a one atom long (100)–step (schematically illustrated in Fig. 6.1).

This system is particularly interesting because cleavage of the first C-H bond of the methane molecule is known to require high energies. All metal surfaces studied so far have one reaction channel in common. At high incident energy methane dissociation is direct, which means that the C-H bond is cleaved upon impact with the surface. Even though one might expect for this simple picture a straightforward reaction mechanism, the dynamic interaction of gas-phase methane with metal surfaces was found to be extremely complex as many degrees of freedom are involved in surmounting the activation barrier. The dissociation probability is therefore enhanced by the incident translational and vibrational energy of impinging molecules and often by surface temperature [134, 155–159]. Interestingly, apart from the direct mechanism, additional reaction channels have been observed on Ir(110) [160] or Pt(110) [161] accessible for CH $_4$ molecules with low translational energy. Whereas for the direct channels, maximum chemisorption probabilities in the order of 0.2 to 0.3 were found, the low energy channels exhibit maximum probabilities in the order of defect concentrations typical for single crystalline surfaces prepared under UHV–conditions ($\approx 10^{-3}$).

6.2 Experimental

The experimental facilities for this study were provided by the Department of Chemistry, The University of Southampton, United Kingdom. The setup has been described in more detail elsewhere [137, 138, 162].

Briefly, it consists of a UHV–chamber connected to a two–stage differentially pumped molecular beam line. The main chamber is pumped by a turbomolecular pump and is equipped with low electron energy diffraction (LEED), an ion sputter gun and two quadrupole mass spectrometers (QMS). One mass spectrometer is differentially pumped and can be rotated around the chamber axis. This is used to measure angular distributions of particles scattered from the surface and to determine the velocity distribution of the beam. The other serves for thermal desorption spectroscopy (TDS), reaction and sticking measurements. Crystals are heated by a DC–current and the crystal temperature is measured by a thermocouple. The Pt–crystal was cut and polished to within 0.5^{o} of the (533)–plane and surface structure was confirmed by LEED. High surface purity was accomplished by several cycles of Ar–ion bombardement at 300 and 600 K. Remaining carbon was removed by repetitively exposing the crystal to oxygen at T s <300 K followed by heating to 1300 K. By annealing the crystal at 1300 K for 10 to 20 min silicon impurities which are believed to agglomerate at the surface during the oxygen treatment were dissolved into the bulk. Surface quality was checked by LEED and by a comparison of the oxygen TDS with previous measurements [163].

The molecular beam was generated by expansion of gas mixtures through a glass nozzle which could be resistively heated. Beam energies were varied by seeding methane in He, H₂, Ne, and Ar at nozzle temperatures between 300 and 900 K. Unfortunately, due to technical problems not all of the energies could be verified by TOF–measurements. Therefore, for the undetermined beams ideal behavior was assumed and the energy computed in analogy to equation 5.4.

Sticking probabilities higher than 5% were measured by the method developed by King and Wells (K&W) [56, 57]. Smaller sticking probabilities were determined by measuring the carbon

92 Chapter six

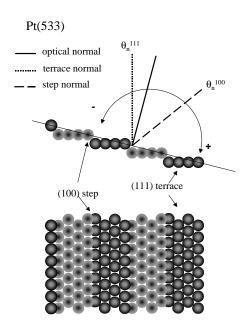


Figure 6.1: Schematic illustration of the Pt(533) surface.

uptake versus CH₄ exposure as the initial slope of such an uptake curve is proportional to the initial dissociative chemisorption probability. Relative values for the CH₄ flux were determined by following the CH₄ exposure with the QMS. As the amount of dissociatively adsorbed methane is proportional to the amount of adsorbed carbon Cads produced by thermal decomposition of the initially formed CH_x fragment, C_{ads} was determined by an isothermal oxidation reaction. This could be realized by first increasing the surface temperature to 600 K to decompose the CH_xfragments and to desorb the formed hydrogen. Note that associative desorption of CH₄ or the formation of other $C_x H_y$ product was never observed. Afterwards, the surface was exposed to an oxygen beam (2% O₂ in He) at the same temperature and the CO and CO₂ formation was followed with the QMS (see Fig. 6.2). The signals are corrected for the differences in detection sensitivities, accomplished by calibrating the corrected reading of the ion gauge against the detector output of the QMS for CO and CO₂. Consequently, the sum of the corrected time integrals of the CO and CO₂ desorption signals was proportional to the amount of surface carbon deposited. This 'titration' method is known to be very sensitive for measuring accurately and reliably small amounts of surface carbon and has been successfully applied in slightly different ways in the past [157, 161, 164]. Clearly, as neither the flux nor the amount of carbon was determined on an absolute scale, the initial slope of the carbon uptake curves yields a relative value for the initial sticking probability. Absolute sticking coefficients can be achieved by measuring an uptake curve at an incident energy where an accurate value for the initial dissociative chemisorption probability could be measured by the K&W method. The right panel of Fig. 6.2 shows a carbon uptake curve at 700 meV incident energy. Methane molecules impinged normal to the terraces of the stepped surface. The x-axis denotes the methane exposure in QMS-detector charge

PROBING BOND BREAKING 93

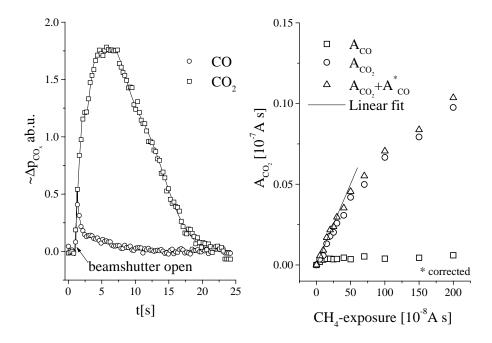


Figure 6.2: Left panel: CO and CO_2 formation during the reaction of adsorbed carbon deposited by dissociative adsorption of methane with oxygen. The surface was kept at T_s =600 K. Opening the beam shutter results in an instantaneous response. Right panel: Carbon uptake curve constructed from titration experiments at different exposures. Differences between QMS-sensitivities of CO and CO_2 have been taken in account. The initial slope of the uptake curve is proportional to the initial dissociative chemisorption probability.

units, the y-axis the time integrals of desorbing CO and CO₂ flux. Simultaneously to the titration measurements, for every data point the initial sticking probability was determined by the K&W method. Thereby, the initial slope of the uptake curve could be linked to the average value (5%) of the K&W-measurements and a correction factor for other measurements could be derived. For all experiments presented here, the azimuth of the scattering plane was set to be normal to the direction of the steps. Positive angles are defined as scattering into the steps. The crystal was aligned with respect to the optical surface normal. θ_n^{111} and θ_n^{100} denote the surface normals of the (111)-terraces and the (100)-steps. The experimental geometry is depicted schematically in Fig. 6.1.

6.3 Results and discussion

Fig. 6.3 shows the initial dissociative sticking probability S_0 of methane as a function of incident energy E_i at a surface temperature of 600 K. The impact conditions are chosen such that the beam impinges normal to the (111)–terraces of the Pt(533) surface. On the left panel of Fig. 6.3 data are plotted on a logarithmic scale. As typical for methane dissociative chemisorption, the initial

94 Chapter six

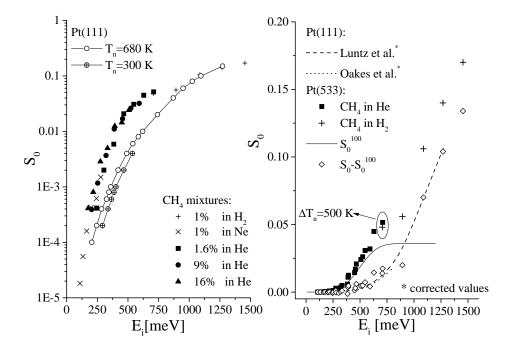


Figure 6.3: Left panel: The initial dissociative chemisorption probability S_0 of methane on Pt(533) at T_s =600 K plotted on a logarithmic scale as a function of translational energy. The S_0 versus energy dependencies on a Pt(111) surface at T_s =800 K and two different nozzle temperatures (T_n =300 and 680 K) are plotted for comparison. Pt(111)—data is taken from Ref. [155]. Right panel: The data of the left panel is replotted on a linear scale. Results from the Pt(111)—surface taken from Ref. [139, 155] are flux and temperature corrected. The solid line indicates the fitted (100)—step contribution $S_0^{100}[E_i]$. Open diamonds represent the values received by subtracting S_0^{100} from S_0 .

methane sticking probability is dramatically enhanced by translational energy, as also observed on Ru(0001) [157], Ni(100) [134], Ni(111) [156], Pd(110) [165] or W(110) [158]. S_0 increases more than two orders of magnitude upon increasing the translation energy of the beam from 100 to 300 meV. In agreement with other experiments, the sticking versus energy curves show at energies up to 600 meV a curvature typical for methane activation on Pt(111) [155,164,166,167]. Surprisingly, the curvature of S_0 versus E_i flattens around 750 meV indicating an energy regime where translational energy appears to couple less efficiently into the reaction coordinate. Another change in reactivity is observed at energies above 860 meV, S_0 starts to increase again until a value of 0.16 is observed at 1452 meV. To be able to judge the influence of the (100)—steps on the methane activation, data obtained by Luntz et al. obtained for a Pt(111) surface are depicted in Fig. 6.3 for comparison [155, 166]. Note that these measurements have been performed at a higher surface temperature (T_s =800 K) and the incident energy has been controlled by keeping the nozzle temperatures T_n constant and varying the seeding ratio. The results for two different nozzle temperatures T_n =300 K and T_n =680 K are depicted. The higher sticking coefficient observed for

PROBING BOND BREAKING 95

the higher nozzle temperature is a consequence of enhanced sticking of vibrationally excited molecules which is indicative for activation barriers with saddle points close to the exit channels.

In our measurement, a different method for varying the translational energy was applied so that the contribution of vibrationally excited molecules to S₀ is difficult to establish. However some indication is given by the large scatter between the measuring-series for different gas mixtures on the Pt(533) surface. At higher translational energies the scatter of the data points decreases. The reason for this behavior is evident, as the vibrational temperature of the molecular beam is controlled by the nozzle, the fraction of excited molecules is constant and generally very small, especially for the nozzle temperatures applied in this study. As the combination of vibrational and translational energy promotes dissociation, vibrationally excited molecules usually require less translational energy. As a result, above a certain threshold translational energy all vibrationally excited molecules will dissociate. Consequently, the contribution of the vibrationally excited molecules to S_0 is roughly proportional to the number of vibrationally excited molecules which is very small. Note that this is not entirely true because the coupling of the vibrational energy into the reaction coordinate can be less efficient at higher translational energies as observed by Juurlink et al. [132]. Clearly, if the dissociation probability reaches values in the order of several percent the tendency of S_0 versus E_i curves will be dominated by the translationally activated molecules. At 700 meV translational energy, S_0 is independent of nozzle temperature for different seeding gases. Due to the lighter H₂ mass CH₄ is much more efficiently accelerated which allows T_n to be decreased by 500 K with respect to the He-seeded beam at a constant energy. As both data points measured by the K&W technique almost coincide the contribution of the vibrationally excited molecules can be neglected in this energy regime. Since all data points follow a general trend with a relativly small scatter, we conclude that the observed enhancement of dissociative sticking can be mainly attributed to activation by translational energy. This is in fair agreement with the results on the Pt(111) surface. Note that for the following discussion we will disregard the small changes induces by vibrationally excited molecules.

The most obvious difference between the stepped (533) and the (111) surface is that, in the low energy regime ($E_i \leq 600 \text{ meV}$), the Pt(533) appears to be approximately an order of magnitude more active than the Pt(111) surface. In contrast, at incident energies above 900 meV the same activity is found. On the right part of Fig. 6.3 the Pt(533) data from the left panel is replotted on a linear scale. For a quantitative comparison between the two surfaces, the Pt(111) results have been corrected for different experimental conditions applied. Since it is known that S_0 increases with T_s on Pt surfaces, the results obtained for the Pt(111) (T_s =800 K) have to be corrected for the different surface temperatures. Unfortunately, $S_0[E_i]$ is not independent on T_s . It has been found that at low energy ($E_i \approx 420 \text{ meV}$), S_0 follows an Arrhenius expression whereas at high incident energy ($E_i \approx 1270 \text{ meV}$) S_0 scales linearly with E_i [155, 166].

Consequently, upon increasing the surface temperature not only the absolute values of S_0 change but also the curvature of the $S_0[E_i]$ dependency. For the correction the linear dependency has been taken which implies a distortion of the curvature in the low energy regime. To give an estimate of the error induced by this procedure, the results of Oakes et al. [139] measured at T_s =550 K are depicted in Fig. 6.3 (right panel) as a dotted line for comparison. Note that the correction procedure is in good agreement with the experimental results at 550 K which even underestimate our experimental conditions(T_s =600 K).

Both Pt(111) results require a further correction as the catalytic (111)–activity of the Pt(533) surface is reduced with respect to the Pt(111) surface. The fraction of the (111) surface area

96 Chapter six

of the Pt(533) probed by the molecular beam can be computed from the scattering geometry. Note that this reasoning only holds if the catalytic area is strictly proportional to what geometry predicts. Problems arising from this simplification will be discussed below. In order to be able to compare the two surfaces, both Pt(111) results are multiplied by this geometric correction factor. The $S_0[E_i]$ —curve of the Pt(533) can now be constructed from the (111)—dependency and a fit function for the step contribution. The best fit results are obtained for a function of the following type:

$$S_0^{100}[E_i] = \frac{A}{2} (1 + \operatorname{erf}(\frac{E_i - E_t}{w}))$$
(6.1)

where $S_0^{100}[E_i]$ is the step contribution of the sticking versus energy function and A, E_t and w are parameters. Note that the choice of such a fit function implies a Gaussian distribution of barrier heights. This concept has been introduced by Michelsen et al. [168]. $S_0^{100}[E_i]$ for A=0.036, w=189 meV and $E_t=495$ meV is depicted in Fig. 6.3 (right panel) as a solid line. The quality of the fit can be judged by comparing the corrected Pt(111) (dashed line) results with the subtraction of the fit-function from the data points (open diamonds). The value of A can be corrected for the catalytically active surface area which yields a maximum sticking coefficient of $S_0^{100}[\theta_i = \theta_n^{111}] = 0.20$ for the (100) step. Note that the chosen fit function (Equation 6.1) is the simplest function which is able to yield a reasonable fit for the 'step' contribution. Due to the correction procedures of the Pt(111) results the curvature and the absolute sticking coefficient of the corrected data might be overestimated especially due to the strictly geometric correction. Consequently, S_0^{100} might not be constant for $E_i \gg E_t$ and increase with E_i . Such a behavior has been observed for CH₄ dissociation on Pt(110)(1 \times 2). On the other hand, the observation that at high incident energies the dissociation probability reaches a saturation value smaller than unity is not very surprising and has been observed for other systems such as H₂ on Cu [168]. Moreover, theoretical work has shown that with increasing degrees of freedom considered in the computations, the saturation value of the dissociation probability decreases [169, 170].

Nevertheless, the results of the fit suggest that steps offer a low energetic bypass to dissociative chemisorption with a reduction of the barrier height of roughly 250-280 meV as estimated from Fig. 6.3 (left panel). This channel most likely saturates and at incident energies above 700 meV the observed increase in activity can be attributed to dissociation on the (111) terraces. If this is true, at high energies the angular dependency of S_0 should show a sharp $\cos^{n-1}\theta_i$ distribution which peaks around the terrace surface normal. Such a behavior is expected because of the following: Applying detailed balance, the sticking process can be related to the recombinative desorption of $CH_3 + H \longrightarrow CH_4$ [171]. The adsorption-desorption equilibrium yields a similar angular dependency for the desorbing flux f_d where f_d is proportional to $\cos^n \theta_i$. A sharp angular distribution of the product distribution along the surface normal is observed if the recombination occurs over an activation barrier [172]. Evidence that the dissociation efficiency at high energies is dominated by the terrace contribution is given by the results depicted in Fig. 6.4 where S_0 is plotted as a function of the angle of incidence θ_i at E_i =1450 meV. The results clearly show that the angular dependency of the sticking coefficient peaks around the terrace normal. The non- $\cos^{n-1}\theta_i$ tendency observable at positive angles indicates the contribution of the steps. If one assumes that terraces and steps act as two independent active surfaces one should be able to decompose the data into the sum of two $\cos^{n-1} \theta_i$ distributions as described by the following:

$$S_0^{533}[\theta_i] = A_{111} S_{0.0}^{111} \cos^{n_{111}-1}(\theta_i + \theta_n^{111}) + A_{100} S_{0.0}^{100} \cos^{n_{100}-1}(\theta_i - \theta_n^{100*})$$

$$(6.2)$$

PROBING BOND BREAKING 97

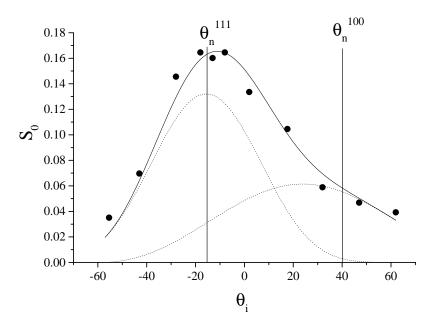


Figure 6.4: Angular dependency of S_0 at E_i =1450 meV and T_s =600 K. θ_n^{111} and θ_n^{100} denote the surface normals of terraces and steps. The contributions of the terraces and steps to S_0 are indicated by dotted lines and a model which assumes two different catalytically active surfaces (see equation 6.2)

where A_{111} and A_{100} are geometric correction factors for the catalytic active area seen by the molecular beam dependent on θ_i , $S_{0,0}^{111}$ and $S_{0,0}^{100}$ are maximum sticking coefficients of terraces and steps with respect to the local surface normals θ_n^{111} and θ_n^{100*} . θ_n^{100*} is used as a fit parameter because due to the short length of the step edge a strict geometrically determined surface normal might not exist. To reduce the amount of fit parameters the angular dependency of the terraces has been obtained from the Pt(111) data since it has been shown that S_0 on Pt(111) scales with normal energy ($E_n = E_i \cos^2 \theta_i$). By this means, $S_{0,0}^{111}$ and n_{111} can be independently determined from a $\cos^{n-1}\theta_i$ fit to the Pt(111) data. Note that $S_{0,0}^{111}$ has to be flux and temperature corrected. Factors $A_{111}[\theta_i]$ and $A_{100}[\theta_i]$ can be computed from geometric considerations and can therefore also be independently determined. Inserting these known parameters into equation 6.2, the parameters for the (100) steps can be obtained from a fit to the data of Fig. 6.4. Note that $S_{0,0}^{100*}$, θ_n^{100*} and n_{100} are the only fit parameters. The fit yields a maximum value for the (100) step sticking coefficient of $S_{0,0}^{100}$ of 0.22 with a corresponding surface normal θ_n^{100*} of T_0^{0*} and for $T_{0,0}^{0*}$ a value of 3.5 is found. Note that the fitted angular contributions to T_0^{100*} dependent active (100) area. Therefore, the maximum of the step contribution is shifted to a more grazing angle and the highest value for step dissociation is 0.06 instead of 0.22.

The smaller value of n_{100} of the fit is in good agreement with the lower barrier height observed at the steps. However, the position of the corresponding surface normal $\theta_n^{100*}=7^{\circ}$ is unexpected

98 Chapter six

as this behavior is in contradiction with the observation on the (111) surface. Therefore, it is very likely that the dissociation site with the lowest barrier is not the fourfold site located in the step surface plane. Surprisingly, the value of θ_n^{100*} derived from the fit is very close to half of the angle defined by the (100)– and (111)–planes ($\theta_p=180^{\circ}$ -($\theta_n^{100}+\theta_n^{111}$)) which indicates that dissociation is most efficient for molecules which impinge along the bisecting line of θ_p . This behavior suggests that step dissociation proceeds via a concerted interaction with two surface planes. For such an interaction one would expect a smaller barrier height because the surface provides instead of a flat an angular dissociation site which might be advantageous to attack the tetrahedral symmetry of the molecule. This picture is in agreement with the 'splat'-model introduced by Lee et al. [156] which assumes that the dissociation of methane requires the deformation of the C–H bonds to allow the carbon atom to reach close contact to the surface.

This geometric reasoning is in agreement with recent quantum calculations of nitrogen dissociation on Ru(0001) [152]. Rather different symmetries for the transition states at steps and terraces are found and the barrier height reduces by 900 meV! The authors attributed the decrease in barrier height at the step partly to the fact that the configuration of the transition state at the step comprises of an additional Ru–atom. This lowers repulsive adsorbate—adsorbate interactions caused by the two nitrogen atoms which compete for the surface atoms.

The concept of enhanced catalytic activity at defects has also been discussed in terms of the Brønsted–Polanyi relation (see e.g. [148]). Within this concept, the lowering of the barrier height is associated with a stronger bonding of reactants and products to the surface. Generally, due to the lower coordination numbers of step atoms, reactants and products are more strongly adsorbed.

The frequently observed rate enhancement associated with defects or steps has also been observed for the methane on different Pd-surfaces [173]. The rate of dissociation increases in the order Pd(111) < Pd(311) < Pd(679) [174, 175]. However, no attempt was made to link the reaction to a specific site. In contrast to these observation, increasing the defect character of a Pt(111) surface by Ar-ion bombardement seems not to effect the dissociation probability at all [167]. The interpretation of this observation is difficult because defects induced by sputtering are very ill-defined and as experiments are performed at elevated temperatures reactive structures might disappear before they interact with methane molecules. Unfortunately, no molecular beam study of CH₄ dissociation on Pt(100) is available to our knowledge which rules out a direct comparison between the activity of a (100)-surface and of a (100)-step. Measurements on a Ni(111) [156] and Ni(100) [134] surface revealed that the more open (100)-structure substantially enhances the initially dissociative chemisorption probability. The sticking versus energy curve measured at similar conditions shifts ≈ 250 meV to lower energy for the more open surface. A smaller shift ($\approx 150 \text{ meV}$) is observed between the direct dissociation channels on Ir(110) [160] and Ir(111) [159]. The energy differences, especially the one for Ni, are in the order of the energy difference observed in our study. For these reasons, it is difficult to judge whether Pt(533)–steps offer a new low energetic route to dissociation because the total reactivity could also consist of the Pt(111)- and Pt(100)-activities weighted by the ratio of the catalytically available surface areas.

The left panel of Fig. 6.5 shows the variation of S_0 with incident energy for two different surface temperatures (T_s =600 K and T_s =110 K). The impact conditions are identical to those of Fig. 6.3 and the translational energy of the beam is controlled by varying the nozzle temperature and keeping the ratio in the gas mixture constant. It is evident from the plot that the dissociative

PROBING BOND BREAKING 99

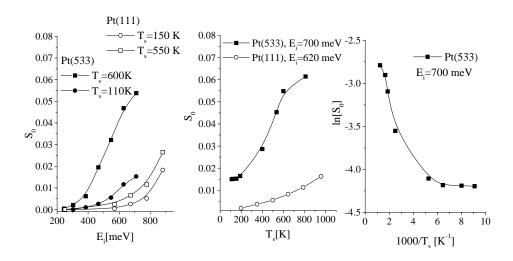


Figure 6.5: Left panel: S_0 versus E_i for two different surface temperatures (solid symbols). The results on the Pt(111) [139] surface for similar conditions are plotted for comparison (open symbols). Middle panel: S_0 versus T_s at a constant incident energy (700 meV) (solid squares). Results from a Pt(111) [176] surface for similar experimental conditions are depicted as open circles. Right panel: Data of the middle panel are replotted to illustrate the non–Arrhenius behavior of the surface temperature dependency.

adsorption is enhanced at elevated surface temperatures. The threshold energy is clearly shifted to lower energy.

Also, a modest surface temperature effect (T_s =550 K and T_s =150 K) has been observed on the Pt(111) surface [139]. For a comparison, results for both surface temperatures are depicted in Fig. 6.5 (left panel). Because of the limited overlap between the energy scales of our measurements and those on the Pt(111) surface, no attempt was made to quantitatively determine the step contribution to S_0 . However, a comparison of the two curves by eye indicates a significant effect associated by (100)-steps: The effect of thermal activation on the (100)-steps is distinctly higher than on the (111)-terraces. In the middle panel of Fig. 6.5, the influence of surface temperature is studied at a fixed incident energy E_i =700 meV. For a comparison the results of a Pt(111) taken from Ref. [176] are depicted as open circles. Whereas at temperatures below 150 K S₀ appears to be temperature independent, between 200 and 600 K S₀ increases substantially. In contrast, the thermal activation on the Pt(111) surface is clearly lower. Moreover, the surface temperature dependency on Pt(111) has been measured at a lower incident energy. Consequently, in comparison to the Pt(533) the influence of T_s on S_0 is overestimated and should be even lower at 700 meV. Note that the slow disappearance of the surface temperature effect with increasing energy can be attributed to a surface 'recoil' effect [177] which means that collision energy is adsorbed by lattice. Consequently less energy is available to surmount the barrier. The right panel of Fig. 6.5 illustrates the non-Arrhenius behavior of S₀ which is not an unexpected observation for CH₄ dissociation.

The influence of surface temperature on dissociative chemisorption of methane has been

100 Chapter six

treated theoretically by various models [166, 178–180]. One of the most recent models is the quantum dynamic model [176, 180–182] which was preceded by the thermally assisted tunneling model developed by Harris and Luntz [166]. In this model the surface temperature is introduced by treating the surface as a single oscillator. The increase in activity with surface temperature can be explained in terms of a 'kick' from the surface cube which assists the molecule in surmounting the barrier. This theoretical attempt models surface temperature effects occuring in dissociative chemisorption of methane on various metal surface reasonably well [181,182]. Such a model is basically consistent with the tendency of Fig. 6.5 (middle panel). Clearly the onset of thermal activation occurs at a temperature which is typically in the order of a Pt surface Debyetemperature, e.g. T_D =118 K for Pt(100) [183] and T_D =230 K for Pt(111) [184]. Therefore, the initial dissociation probability measured at 110 K reflects the efficiency of the (100)–step to introduce gas–phase energy into the reaction coordinate.

One striking observation of the surface temperature effect is that $T_{\rm s}$ has a considerably larger influence on the dissociative chemisorption probability at the (100)–steps than on the (111)–terraces (Fig. 6.5, left and middle panel). One possible explanation could be that because of the lower activation barrier at the (100)–step surface energy couples more efficiently into the reaction coordinate. Note that within the dynamical model, surface temperature induced enhancement is ascribed to the fact that the surface gives the molecule an additional 'kick' to surmount the barrier. Consequently, if the barrier is lower, the influence of surface temperature will be more pronounced.

Another explanation could be the quality of the surface structure. So far we have assumed that the Pt(533)–surface is perfectly ordered at any temperature. Clearly, at higher temperature surface roughening will substantially influence the steps and terraces of the surface. A less ordered structure might increase the effective catalytic surface area attributed to the steps which would lead to a higher dissociation probability. Unfortunately, on the basis of these experiments we cannot estimate the magnitude of this effect.

In summary, the dynamics of dissociative adsorption of methane at Pt (100)—steps strongly resembles the behavior on the (111)—terraces. The major differences are a substantially lower barrier height and a more pronounced surface temperature effect. In the energy and temperature range studied, no indication was found for a reaction mechanism other than the direct dissociation channel. The results suggest, that the higher surface corrugation in combination with the step geometry is responsible for the lowering of the activation barrier.

6.4 Conclusion

The dynamics of dissociative chemisorption of methane on Pt(533) have been studied using molecular beam techniques. A strong enhancement of dissociation with translational energy is seen. A comparison to the reactivity of Pt(111) reveals that dissociation of methane occurs already at lower translational energies. By correcting the data for the different catalytic areas 'seen' by the methane molecules, the energy dependence of the step associated dissociation probability has been determined. The dynamics of step enhanced dissociation indicates saturation. Dissociation is further activated by translational energy on the terraces. The influence of surface temperature is larger at the steps than on the terraces.

- [1] EIA, Annual Energy Outlook 1996, DOE/EIA-0383(96), Washington, DC, 1996.
- [2] American Methanol Institute, World Methanol Supply/Demand, source: DeWitt & Company, Inc., 2000.
- [3] I. Langmuir, The mechanism of the catalytic action of platinum in the reactions of $2CO + O_2 = 2CO_2$ and $2H_2 + O_2 = 2H_2O$, Trans. Faraday Soc. 17, 621 (1922).
- [4] C. N. Hinshelwood, Annual reports on the progress of chemistry, Ann. Res. London Chem. Soc. 27, 11 (1930).
- [5] D. D. Eley and E. K. Rideal, Parahydrogen Conversion on Tungsten, Nature (London) 146, 40 (1940).
- [6] D. D. Eley, The interchange of hydrogen in the adsorbed film on tungsten, Proc. Roy. Soc. London 178, 452 (1941).
- [7] E. W. Kuipers, A. Vardi, A. Danon, and A. Amirav, Surface–molecule proton transfer: a demonstration of the Eley-Rideal mechanism, Phys. Rev. Lett. 66, 116 (1991).
- [8] E. W. Kuipers, M. G. Tenner, M. E. M. Spruit, and A. W. Kleyn, *Differential trapping probabilities and desorption of physisorbed molecules: Application to NO/Ag(111)*, Surf. Sci. **205**, 241 (1988).
- [9] C. T. Rettner and D. J. Auerbach, Distinguishing the direct and indirect products of a gas-surface reaction, Science 263, 365 (1994).
- [10] M. Persson, J. Strömquist, L. Bengtsson, B. Jackson, D. V. Shalashilin, and B. Hammer, A first-principle potential energy surface for Eley-Rideal reaction dynamics of H atoms on Cu(111), J. Chem. Phys. 110, 2240 (1999).
- [11] J. Harris and B. Kasemo, On precursor mechanisms for surface reactions, Surf. Sci. 105, L281 (1981).
- [12] C. Stampfl and M. Scheffler, Anomalous behavior of Ru for catalytic oxidation: A theoretical study of the catalytic reaction $CO+\frac{1}{2}O_2 \rightarrow CO_2$, Phys. Rev. Lett. **78**, 1500 (1997).
- [13] W. H. Weinberg, Kinetics of Surface reactions, in Dynamics of gas-surface interactions edited by C. T. Rettner and M. N. R. Ashford, The Royal Society of Chemistry, 1991.
- [14] H. C. Kang, T. A. Jachimowski, and W. H. Weinberg, Role of local configurations in a Langmuir-Hinshelwood surface reaction: Kinetics and compensation, J. Chem. Phys. 93, 1418 (1990).
- [15] Holloway S., Quantum effects in gas-surface interactions, in Dynamics of gas-surface interactions edited by C. T. Rettner and M. N. R. Ashford, The Royal Society of Chemistry, 1991.
- [16] J. C. Polanyi, Some concepts in reaction dynamics, Acc. Chem. Res. 5, 161 (1972).
- [17] S. Holloway, A. Hodgson, and D. Halstead, Vibrationally assisted sticking at metal surfaces, Chem. Phys. Lett. 147, 425 (1988).

[18] G. Scoles, *Atomic and molecular beam methods II*, edited by G. Scoles, Oxford University Press, 1992.

- [19] G. Scoles, *Atomic and molecular beam methods I*, edited by G. Scoles, Oxford University Press, 1988.
- [20] H. Pauly and J. P. Toennies, Beam experiments at thermal energies, Meth. Exp. Phys. 7A, 227 (1968).
- [21] S. T. Ceyer, D. J. Gladstone, M. McGonigal, and M. T. Schulberg, Molecular beams: Probes of the dynamcis of reactions on surfaces, in Investigations of Surfaces and Interfaces - Part A edited by B. W. Rossiter and R. G. Baetzold, John Wiley & Son, Inc., 1993.
- [22] J. P. Anderson, Gas dynamics: 4. Molecular beam and low density gas dynamics, edited by P. P. Wenger, 1974.
- [23] H. Haberland, U. Buck, and M. Tolle, Velocity distribution of supersonic nozzle beams, Rev. Sci. Instrum. 56, 1712 (1985).
- [24] H. N. Storch, N. Golumbic, and R. B. Anderson, The Fischer-Tropsch and related synthesis, Whiley New York, 1951.
- [25] M. A. Vannice, The catalytic synthesis of hydrocarbons from H₂/CO mixtures over the group VIII metals, J. Catal. 50, 228 (1977).
- [26] P. Winslow and A. T. Bell, Studies of carbon- and hydrogen-containing adspecies present during CO hydrogenation over unsupported Ru, Ni, and Rh, J. Catal. 94, 385 (1985).
- [27] Y. K. Sun and W. H. Weinberg, Determination of the absolute saturation coverage of hydrogen on Ru(001), Surf. Sci. 214, L246 (1989).
- [28] H. Shi and K. Jacobi, Hydrogen vibrations on the Ru(001) surface revisted, Surf. Sci. 313, 289 (1994).
- [29] I. M. Ciobîcă, F. Frechard, R. A. van Santen, and Kleyn A. W., to be published.
- [30] J. C. Fuggle, T. E. Madey, M. Steinkilberg, and D. Menzel, *Photoelectron spectroscopic studies of adsorption of CO and oxygen on Ru*(001), Surf. Sci. **52**, 521 (1975).
- [31] H. Pfnür, D. Menzel, F. M. Hoffmann, A. Ortega, and A. M. Bradshaw, *High resolution vibrational spectroscopy of CO on Ru(001): the importance of lateral interactions*, Surf. Sci. **93**, 431 (1980).
- [32] J. C. Fuggle, T. E. Madey, M. Steinkilberg, and D. Menzel, *Angular dependence of UV photoemission spectra from clean Ru*(001) and from adsorbed oxygen and CO, Chem. Phys. 11, 307 (1975).
- [33] H. Pfnür and D. Menzel, The influence of adsorbate interactions on kinetics and equilibrium for CO on Ru(001).I. Adsorption kinetics, J. Chem. Phys. 79, 2400 (1983).
- [34] H. Pfnür and D. Menzel, The influence of adsorbate interactions on kinetics and equilibrium for CO on Ru(001). II. Desorption kinetics and equilibrium, J. Chem. Phys. 79, 4613 (1983).
- [35] F. Delbecq, B. Moraweck, and L. Vérité, Adsorption of CO and NO on (111) and (100) surfaces of Pd₃Mn compared with Pd: a theoretical approach, Surf. Sci. **396** (1998).
- [36] F. Delbecq and P. Sautet, Interplay between magnetism and chemisorption: a theoretical study of CO and NO adsorption on a Pd₃Mn alloy surface, Chem. Phys. Lett. **302**, 91 (1999).
- [37] F. Delbecq and P. Sautet, Density functional periodic study of CO adsorption on the Pd₃Mn(100) alloy surface: Comparison with Pd(100), Phys. Rev. B **59**, 5142 (1999).
- [38] A. Eichler and J. Hafner, Adsorption of CO on Rh(100) studied by ab initio local-density functional calculations, J. Chem. Phys. 109, 5585 (1998).

[39] Y. Morikawa, J. J. Mortensen, B. Hammer, and J. K. Nørskov, CO adsorption and dissociation on Pt(111) and Ni(111) surfaces, Surf. Sci. 386, 67 (1997).

- [40] B. Hammer, O. H. Nielsen, and J. K. Nørskov, Structure sensitivity in adsorption: CO interaction with stepped and reconstructed Pt surfaces, Cat. Lett. 46, 31 (1997).
- [41] D. Curulla, Clotet A., and J. M. Ricart, Ab-initio cluster model study of the chemisorption of CO on low-index platinum surfaces, J. Phys. Chem. B 103, 5246 (1999).
- [42] B. Hammer, Y. Morikawa, and J. K. Nørskov, CO chemisorption at metal surfaces and overlayers, Phys. Rev. Lett. 76, 2141 (1996).
- [43] C. Stampfl and M. Scheffler, Density-functional theory study of the catalytic oxidation of CO over transition metal surfaces, Surf. Sci. 433-435, 119 (1999).
- [44] R. L. C Wang, Kreuzer H. J., and D. Menzel, Interpretation of a co-adsorbate-induced tilt: $(2\times2)(CO+O)$ on Ru(001), Z. Phys. Chem. **202**, 205 (1997).
- [45] D. E. Peebles, J. A. Schreifels, and J. M. White, The interaction of coadsorbed hydrogen and carbon monoxide on Ru(001), Surf. Sci. 116, 117 (1982).
- [46] C. H. Mak, A. A. Deckert, and S. M. George, Effect of coadsorbed carbon monoxide on the surface diffusion of hydrogen on Ru(0001), J. Chem. Phys. 8, 5242 (1989).
- [47] G. Kresse and J. Furthmüller, Efficiency of ab-initio total energy calculations for metals and semi-conductors using a plane-wave basis set, Comp. Mat. Sci. 6, 15 (1996).
- [48] G. Kresse and J. Furthmüller, Efficient iterative schemes for ab initio total-energy calculations using a plane-wave basis set, Phys. Rev. B **54**, 11169 (1996).
- [49] Perdew J. P., Electronic Structure of Solids '91, Akademie Verlag, Berlin, 1991.
- [50] M. Methfessel and A. T. Paxton, High-precision sampling for Brillouin-zone integration in metals, Phys. Rev. B 40, 3616 (1989).
- [51] D. Vanderbilt, Soft self-consistent pseudopotentials in a generalized eigenvalue formalism, Phys. Rev. B 41, 7892 (1990).
- [52] G. Kresse and J. Hafner, Norm-conserving and ultrasoft pseudopotentials for first-row and transitionelements, J. Phys.: Condens. Matter 6, 8245 (1994).
- [53] I. M. Ciobîcă, F. Frechard, R. A. van Santen, A. W. Kleyn, and J. Hafner, *A theoretical study of CHx chemisorption on the Ru*(0001) *surface*, Chem. Phys. Lett. **311**, 185 (1999).
- [54] A. Raukema, R. J. Dirksen, and A. W. Kleyn, Probing the (dual) repulsive wall in the interaction of O₂, N₂ and Ar with the Ag(111) surface, J. Chem. Phys. 103, 6217 (1995).
- [55] A. Raukema, A. P. de Jongh, H. P. Alberda, R. Boddenberg, E. de Haas, A. W. Kleyn, H. Neerings, R. Schaafsma, and H. Veerman, A three-axis gonoiometer in an UHV molecular beam experiment, Meas. Sci. Technol. 8, 253 (1997).
- [56] D. A. King and M. G. Wells, Molecular beam investigation of adsorption kinetics on bulk metal targets: Nitrogen on tungsten, Surf. Sci. 29, 454 (1972).
- [57] D. A. King and M. G. Wells, Reaction mechanism in chemisorption kinetics: Nitrogen on the (100) plane of tungsten, Proc. Roy. Soc. 339, 245 (1974).
- [58] I. M. Ciobîcă, F. Frechard, R. A. van Santen, and Kleyn A. W., to be published.
- [59] H. Pfnür and D. Menzel, The influence of adsorbate interactions on kinetics and equilibrium for CO on Ru(001). I. Adsorption kinetics, J. Chem. Phys. 79, 2400 (1983).
- [60] B. Riedmüller, I. M. Ciobîcă, D. C. Papageorgopoulos, B. Berenbak, R. A. van Santen, and A. W. Kleyn, The dynamic interaction of CO with Ru(0001) in the presence of adsorbed CO and hydrogen, Surf. Sci. 465, 347 (2000).

[61] H. Jónsson, G. Mills, and W. Jacobsen, in: Classical and Quantum dynamics in Condensed Phase Simulations, edited by B. J. Berne, G. Ciccotti and D. F. Coker, World Scientific, Singapore, p. 385, 1998.

- [62] G. Mills and H. Jónsson, Quantum and thermal effects in H₂ dissociative adsorption: Evaluation of free energy barriers in multidimensional quantum systems, Phys. Rev. Lett. **72**, 1124 (1994).
- [63] G. Mills, H. Jónsson, and G. K. Schenter, Reversible work transition state theory: Application to dissociative adsorption of hydrogen, Surf. Sci. 324, 305 (1995).
- [64] J. Harris and A. C. Luntz, Sticking and scattering in the molecular chemisorption regime: CO on Pt(111), J. Chem. Phys. 91, 6421 (1989).
- [65] H. P. Steinrück and R. J. Madix, The interaction of CO and Ar molecular beams with Ir(110), Surf. Sci. 185, 36 (1987).
- [66] S. L. Tang, J. D. Beckerle, M. B. Lee, and S. T. Ceyer, Effect of translational energy on the molecular chemisorption of CO on Ni(111): Implications for the dynamics of the chemisorption process, J. Chem. Phys. 84, 6488 (1986).
- [67] S. Kneitz, J. Gemeinhardt, H. Koschel, G. Held, and H.-P. Steinrück, Energy and temperature dependent sticking coefficients of CO on ultrathin copper layers on Ru(001), Surf. Sci. 433-435, 27 (1999).
- [68] D. A. Butler, B. Berenbak, S. Stolte, and A. W. Kleyn, *Elastic scattering in a reactive environment:* NO on Ru(0001)(1×1)H, Phys. Rev. Lett. **78**, 4653 (1997).
- [69] R. M. Logan and R. E. Stickney, Simple classical model for the scattering of gas atoms from a solid surface, J. Chem. Phys. **44**, 195 (1966).
- [70] R. J. W. E. Lahaye, A. W. Kleyn, S. Stolte, and S. Holloway, The scattering of Ar from Ag(111) A molecular-dynamics study, Surf. Sci. 338, 169 (1995).
- [71] G. E. Thomas and W. H Weinberg, The vibrational spectrum and adsorption site of CO on the Ru(001), J. Chem. Phys. **70**, 1437 (1979).
- [72] J. T. Grant and T. W. Haas, A study of Ru(0001) and Rh(111) surfaces using LEED and Auger electron spectroscopy, Surf. Sci. 21, 76 (1970).
- [73] D. E. Williams and W. H. Weinberg, *The geometric structure of carbon monoxide chemisorbed on the ruthenium (001) surface at low temperatures*, Surf. Sci. **82**, 93 (1979).
- [74] G. Michalk, M. Moritz, H. Pfnür, and D. Menzel, A LEED determination of the structures of Ru(001) and of $Ru(001)(\sqrt{3} \times \sqrt{3})R30^{\circ}$ CO, Surf. Sci. **129**, 92 (1983).
- [75] H. Pfnür and D. Menzel, Lateral interactions for CO/Ru(001): Order-disorder transitions of the $\sqrt{3}$ -structure, Surf. Sci. **148**, 411 (1984).
- [76] D. E. Williams, W. H. Weinberg, and A. C. Sobrero, *CO on Ru(001): Island size and disordering*, J. Chem. Phys. **76**, 1150 (1982).
- [77] H. Pfnür and H. J. Heier, Order-disorder phenomena in the system CO/Ru(001), Ber. Bunsenges. Phys. Chem. 90, 272 (1986).
- [78] G. Held, H. Pfnür, and D. Menzel, A LEED-IV investigation of the Ru(001)-p(2×1)H structure, Surf. Sci. 271, 21 (1992).
- [79] J. Braun, K. L. Kostov, G. Witte, and Ch. Wöll, CO overlayers on Ru(0001) studied by helium atom scattering: Structure, dynamics, and the influence of coadsorbed H and O, J. Chem. Phys. 106, 8262 (1997).
- [80] R. L. C. Wang, H. J. Kreuzer, P. Jakob, and D. Menzel, Lateral interactions in coadsorbate layers: Vibrational frequency shifts, J. Chem. Phys. 111, 2115 (1999).

- [81] A. Raukema, Dynamics of chemisorption, PhD thesis, University of Amsterdam, 1995.
- [82] F. M. Hoffmann, The kinetics of CO dissociation on Ru(001) time-resolved vibrational spectroscopy at elevated pressures, J. Chem. Phys. 90, 2816 (1989).
- [83] M.P D'Evelyn, H. P. Steinrück, and Madix R. J., *Precursors and trapping in the molecular chemisorption of CO on Ni(100)*, Surf. Sci. **180**, 47 (1987).
- [84] R. J. W. E. Lahaye, S. Stolte, S. Holloway, and A. W. Kleyn, Orientation and energy dependence of NO scattering from Pt(111), J. Chem. Phys. 104, 8301 (1996).
- [85] R. J. W. E. Lahaye, S. Stolte, A. W. Kleyn, R. J. Smith, and S. Holloway, *Site dependent energy loss in Ar scattering from Pt(111)*, Surf. Sci. **307-309**, 187 (1994).
- [86] A. W. Kleyn, Non-reactive orientations of molecules at surfaces, Prog. Surf. Sci 54, 407 (1997).
- [87] A. E. Wiskerke and A. W. Kleyn, Angular and translational energy distributions of NO scattered from Pt(111), J. Phys.: Condens. Matter 7, 5195 (1995).
- [88] E. W. Kuipers, M. G. Tenner, M. E. M. Spruit, and A. W. Kleyn, Angular and energy distributions of NO scattered from Ag(111)-surface, Surf. Sci. 189/190, 669 (1987).
- [89] M. A. Hines and R. N. Zare, *The interaction of CO with Ni(111) rainbows and rotational trapping*, J. Chem. Phys. **98**, 9134 (1993).
- [90] A. E. Wiskerke, C. A. Taatjes, and A. W. Kleyn, Survival mechanism for rotational rainbows in highly attractive molecule-surface systems: NO scattering from Pt(111), Chem. Phys. Lett. 216, 93 (1993).
- [91] A. E. Wiskerke, C. A. Taatjes, A. W. Kleyn, R. J. W. E. Lahaye, S. Stolte, D. K. Bronnikov, and B. E. Hayden, *Rotational rainbows in NO scattering from Pt(111)*, Faraday Disscuss. **96**, 297 (1993).
- [92] T. F. Hanisco and A. C. Kummel, The effect of surface passivation on rotationally inelastic scattering: N_2 scattered from W(110), $W(110)(2\times2)N$, $W(110)(1\times1)H$ and Pt(111), J. Chem. Phys. **99**, 7076 (1993).
- [93] T. F. Hanisco, C. Yan, and A. C. Kummel, Energy and momentum distributions versus incident energy in the scattering of CO from Ag(111), J. Vac. Sci. Technol. A 11, 2090 (1993).
- [94] B. Riedmüller, I. M. Ciobîcă, D. C. Papageorgopoulos, F. Frechard, B. Berenbak, A. W. Kleyn, and R. A. van Santen, *CO adsorption on hydrogen saturated Ru*(0001), Chapter 2 of this thesis.
- [95] H. Schlichting and D. Menzel, PhD thesis, Technische Universität München, 1990.
- [96] D. Menzel, W. Brening, T. Brunner, W. Frieβ, and H. Schlichting, Sticking of rare-gas atoms in wetting and non-wetting systems, J. Electron. Spectrosc. Relat. Phemon. 64/65, 583 (1993).
- [97] A. W. Kleyn and T. C. M. Horn, Rainbow scattering from solid surfaces, Phys. Rep 199, 91 (1991).
- [98] B. Berenbak, A. T. Zboray, D. C. Papageorgopoulos, B. Riedmüller, S. Stolte, and A. W. Kleyn, *Ar on Ru*(0001), a comparison to the washboard model and trajectory calculations, to be published.
- [99] J. Braun, K. L. Kostov, G. Witte, L. Surnev, J. G. Skofronick, S. A. Safron, and Ch. Wöll, Surface phonon dispersion curves for a hexagonally close packed metal surface: Ru(0001), Surf. Sci. 372, 132 (1997).
- [100] H. Schlichting, D. Menzel, T. Brunner, and W. Brenig, Sticking of rare gas atoms on the clean Ru(001) surface, J. Chem. Phys. 76, 4453 (1992).
- [101] J. A. Venables, G. D. Spiller, and M. Hanbücken, Nucleation and growth of thin films, Rep. Prog. Phys 47, 399 (1984).
- [102] B. Berenbak, D. A. Butler, B. Riedmüller, D. C. Papageorgopoulos, S. Stolte, and A. W. Kleyn, Sticking probability measurements in a reactive system: NO on bare Ru(0001), Surf. Sci. 414, 271 (1998).

[103] J. M. White and S. Akther, Adsorbate-adsorbate interactions during coadsorption on metals, CRC Critic. Rev. Solid State Mat. Sci. 14, 131 (1988).

- [104] D. E. Williams, P. A. Thiel, W. H. Weinberg, and T. J. Yates Jr., Segregation of co-adsorbed species: Hydrogen and carbon monoxide on the (111) surface of rhodium, J. Chem. Phys. 72, 3496 (1980).
- [105] G.A. Kok, A. Noordermeer, and B.E. Nieuwenhuys, *Decomposition of methanol and the interaction of coadsorbed hydrogen and carbon monoxide on a Pd(111) surface*, Surf. Sci. **135**, 65 (1983).
- [106] Y. Kim, H. C. Peebles, D. N. Belton, and J. M. White, Adsorption of D₂, CO and the interaction of adsorbed D₂ and CO on Rh(100), ss 114, 363 (1982).
- [107] M. Mavrikakis, B. Hammer, and J. K. Nørskov, Effect of strain on the reactivity of metal surfaces, Phys. Rev. Lett. 81, 2819 (1988).
- [108] P. Feulner and D. Menzel, The adsorption of hydrogen on ruthenium (001): Adsorption states, dipole moments and kinetics of adsorption and desorption, Surf. Sci. 154, 465 (1985).
- [109] B. Poelsema and G. Comsa, Scattering of Thermal Energy Atoms from Disordered Surfaces, Springer Verlag, 1989.
- [110] B. Poelsema, S. T. de Zwart, and G. Comsa, Scattering cross section of low-coverage CO on Pt(111) for thermal He and H₂ beams, Phys. Rev. Lett. **49**, 578 (1982).
- [111] B. Poelsema, S. T. de Zwart, and G. Comsa, Errata: Scattering cross section of low-coverage CO on Pt(111) for thermal He and H_2 beams, Phys. Rev. Lett. **51**, 522 (1983).
- [112] J. Lee, J. P. Cowin, and L. Wharton, *He diffraction from clean Pt(111) and (1×1) H/Pt(111) surface*, Surf. Sci. **130**, 1 (1983).
- [113] L. Bernasek, K. Lenz, B. Poelsema, and G. Comsa, Formation of islands consisting of repelling adsorbates, Surf. Sci. 183, L319 (1987).
- [114] K. Lenz, B. Poelsema, L. Bernasek, and G. Comsa, Lateral distribution of coadsorbed H and CO on Pt(111) studied by TEAS, Surf. Sci. 189/190, 431 (1987).
- [115] D. E. Peebles, J. R. Creighton, D. N. Belton, and J. M. White, Coadsorption of Hydrogen and Carbon Monoxide on Nickel and Platinum, J. Catal. 80, 482 (1983).
- [116] L. J. Richter, B. A. Gurney, and W. Ho, *The influence of adsorbate-adsorbate interactions on surface structure: The coadsorption of CO and H*₂ on *Rh*(100), J. Chem. Phys. **86**, 477 (1987).
- [117] D. E. Williams and W. H. Weinberg, Computations of profiles of low-energy electron diffraction beams for arrays of ordered islands, Surf. Sci. 109, 574 (1981).
- [118] T. A. Witten Jr. and L. M. Sander, Diffusion-limited aggregation, a kinetic critical phenomenon, Phys. Rev. Lett. 47, 1400 (1981).
- [119] T. A. Witten Jr. and L. M. Sander, Diffusion-limited aggregation, Phys. Rev. B 27, 5686 (1983).
- [120] G. Rosenfeld, A. F. Becker, B. Poelsema, L. K. Verheij, and G. Comsa, Magic clusters in two dimensions, Phys. Rev. Lett. 69, 917 (1992).
- [121] E. Watts and G. O. Sitz, Surface temperature dependence of rotational excitation of H₂ scattered from Pd(111), J. Chem. Phys. 111, 9791 (1999).
- [122] M. J. Murphy, J. F. Skelly, A. Hodgson, and B. Hammer, Nitrogen recombination dynamics at Cu(111): Rotational energy release and product angular distribution, J. Chem. Phys. 109, 3619 (1998).
- [123] C. T. Rettner, L. A. DeLouise, and D. J. Auerbach, Effect of incidence kinetic energy and surface coverage on dissociative chemisorption of oxygen on W(110), J. Chem. Phys. 85, 1131 (1986).

[124] T. F. Hanisco, C. Yan, and A. C. Kummel, Energy and momentum distributions and projections in scattering of CO from Ag(111), J. Chem. Phys. 97, 1484 (1992).

- [125] F. H. Geuzebroek, M. G. Wiskerke A. E., Tenner, A. W. Kleyn, S. Stolte, and A. Namike, Rotational excitation of oriented molecules as a probe of molecule surface interaction, J. Phys. Chem. 95, 8409 (1991).
- [126] M. G. Tenner, F. H. Geuzebroek, E. W. Kuipers, A. E. Wiskerke, A. W. Kleyn, S. Stolte, and A. Namike, Orientation dependence of rotational excitation in NO scattering from Ag(111), Chem. Phys. Lett. 168, 45 (1990).
- [127] Y. H. Huang, C. T. Rettner, D. J. Auerbach, and A. M. Wodtke, Vibrational promotion of electron transfer, Science 290, 111 (2000).
- [128] H. Hou, Y. H. Huang, S. J. Gulding, C. T. Rettner, D.J. Auerbach, and A. M. Wodtke, Enhanced reactivity of highly vibrationally excited molecules on metal surfaces, Science 284, 1647 (1999).
- [129] M. Gostein and G. O. Sitz, Rotational state-resolved sticking coefficients for H₂ on Pd(111): Testing dynamical steering in dissociative adsorption, J. Phys. Chem. **106**, 7378 (1997).
- [130] P. R. McCabe, L. B. F. Juurlink, and A. L. Utz, A molecular beam apparatus for eigenstate-resolved studies of gas-surface reactivity, Rev. Sci. Instrum. 71, 42 (2000).
- [131] L. B. F. Juurlink, R. L. Smith, and A. L. Utz, Controlling surface chemistry with light: Spatially resolved deposition of rovibrational-state-selected molecules, J. Phys. Chem. B 104, 3327 (2000).
- [132] L. B. F. Juurlink, P. R. McCabe, R. L. Smith, C. L. DiCologero, and A. L. Utz, *Eigenstate-resolved studies of gas-surface reactivity: CH*₄ (*v*(*3*)) *dissociation on Ni*(100), Phys. Rev. Lett. **83**, 868 (1999).
- [133] C. E. Borroni-Bird and D. A. King, *An ultrahigh vacuum single crystal adsorption microcalorimeter*, Rev. Sci. Instrum. **62**, 2177 (1991).
- [134] P. M. Holmblad, J. Wambach, and I. Chorkendorff, Molecular beam study of dissociative sticking of methane on Ni(100), J. Chem. Phys. 102, 8255 (1995).
- [135] L. Romm, G. Katz, R. Kosloff, and M. Assher, Dissociative chemisorption of N₂ on Ru(0001) enhanced by vibrational and kinetic energy: Molecular beam experiments and quantum chemical calcualtions, J. Phys. Chem. B 101, 2213 (1997).
- [136] M. C. Wheeler, D. C. Seets, and C. B. Mullins, Trapping-mediated and direct dissociative chemisorption of methane on Ir(110): A comparison of molecular beam and bulb experiments, J. Chem. Phys. 105, 1572 (1996).
- [137] B. E. Hayden and C. L. A. Lamont, Vibrational and translational energy partition and the barrier to dissociative H₂ and D₂ adsorption on Cu(110), Surf. Sci. 243, 31 (1991).
- [138] B. E. Hayden and D. C. Godfrey, The mechanism of sticking, trapping and direct dissociation of carbon monoxide on Cu(110), Surf. Sci. 232, 24 (1990).
- [139] D. J. Oakes, Mc Coustra, and M. A. Chesters, *Dissociative Adsorption of methane on Pt(111) induced by hyperthermal collisions*, Faraday Disscuss. **96**, 325 (1993).
- [140] D. J. D. Sullivan and A. C. Kummel, Quick sample exchange manipulator for dual molecular-beam and scanning tunneling microscopy experiments, Rev. Sci. Instrum. 63, 4285 (1992).
- [141] M. Bonn, S. Funk, Ch. Hess, D. N. Denzler, C. Stampfl, M. Scheffler, M. Wolf, and G. Ertl, Phonon-versus electron-mediated desorption and oxidation of CO on Ru(0001), Science 285, 1024 (1999).
- [142] H. G. Jenniskens, A. Bot, P. W. F. Dorlandt, W. van Essenberg, E. de Haas, and A. W. Kleyn, An ultra-high vacuum (UHV) apparatus to study the interaction between adsorbates and photons, Meas. Sci. Technol. 8, 1313 (1997).

[143] P. Feulner and D. Menzel, Simple ways to improve 'flash desorption' measurements from single crystal surfaces, J. Vac. Sci. Technol. 17, 662 (1980).

- [144] B. E. Hayden, K. Kretzschmar, A. M. Bradshaw, and R. G. Greenler, An infrared study of the adsorption of CO on a stepped platinum surface, Surf. Sci. 149, 394 (1985).
- [145] A. T. Gee, B. E. Hayden, C. Mormiche, and T. S. Nunney, *The role of steps in the dynamics of hydrogen dissociation on Pt(533)*, J. Chem. Phys. **112**, 7660 (2000).
- [146] A. C. Luntz, M. D. Williams, and D. S. Bethune, *The sticking of O*₂ *on a Pt(111) surface*, J. Chem. Phys. **89**, 4381 (1988).
- [147] B. Hammer, Reactivity of a stepped surface: NO dissociation on Pd(211), Faraday Disscuss. 110, 323 (1998).
- [148] B. A. Averill, I. M. C. M. Rietjens, P. W. N. M. van Leeuwen, and R. A. van Santen, in: Catalysis: An Integrated Approach, edited by R. A. van Santen, P. W. N. M. van Leeuwen, J.A. Moulijn, B. A. Averill, Elsevier Science B.V., Amsterdam, 1999.
- [149] B. Hammer, Adsorption, diffusion, and dissociation of NO, N and O on flat and stepped Ru(0001), Surf. Sci. 459, 323 (2000).
- [150] F. Frechard, R. A. van Santen, A. Siokou, J. W. Niemantsverdriet, and J. Hafner, Adsorption of ammonia on the Rhodium (111), (100), and stepped (100) surfaces: An ab initio and experimental study, J. Chem. Phys. 111, 8124 (1999).
- [151] F. Esch, A. Baraldi, C. Comelli, S. Lizzit, M. Kiskinova, P. D. Cobden, and B. E. Nieuwenhuys, Atomic nitrogen on steps: A fast x-ray photoelectron spectroscopy study of the NO uptake on Rh(533), Rh(311), and Rh(111), J. Chem. Phys. 110, 4013 (1999).
- [152] S. Dahl, A. Logadottir, R. C. Egeberg, J. H. Larsen, I. Chorkendorff, E. Törnqvist, and J. K. Nørskov, Role of Steps in N₂ Activation on Ru(0001), Phys. Rev. Lett. 83, 1814 (1999).
- [153] A. T. Gee and B. E. Hayden, *The dynamics of O₂ adsorption on Pt(533): Step mediated molecular chemisorption and dissociation*, J. Chem. Phys. **113**, 10333 (2000).
- [154] G. Cao, Y. Seimiya, Y. Ohno, and T. Matsushima, *Reaction sites working in steady-state CO oxidation on a stepped Pt(113) surface*, Chem. Phys. Lett. **294**, 419 (1998).
- [155] A. C. Luntz and D. S. Bethune, Activation of methane dissocition on a Pt(111) surface, J. Chem. Phys. 90, 1274 (1989).
- [156] M. B. Lee, Q. Y. Yang, and S. T. Ceyer, Dynamics of the activated dissociative chemisorption of CH₄ and implication for the pressure gap in catalysis: A molecular beam-high resolution electron energy loss study, J. Chem. Phys. 87, 2724 (1987).
- [157] J. H. Larsen, P. M. Holmblad, and I. Chorkendorff, Dissociative sticking of CH₄ on Ru(0001), J. Chem. Phys. 110, 2637 (1999).
- [158] C. T. Rettner, H. E. Pfnür, and D. J. Auerbach, On the role of vibrational energy in the activated dissociative chemisorption of methane on tungsten and rhodium, Phys. Rev. Lett. 54, 2716 (1985).
- [159] D. C. Seets, C. T. Reeves, B. A. Ferguson, M. C. Wheeler, and C. B. Mullins, Dissociative chemisorption of methane on Ir(111): Evidence for direct and trapping-mediated mechanism, J. Chem. Phys. 107, 10229 (1997).
- [160] D. C. Seets, M. C. Wheeler, and C. B. Mullins, Trapping-mediated and direct dissociative chemisorption of methane on Ir(110): A comparison of molecular beam and bulb experiments, J. Chem. Phys. 107, 3986 (1997).
- [161] A. V. Walker and D. A. King, *Dynamics of the dissociative adsorption of methane on Pt(110)(1×2)*, J. Chem. Phys. **112**, 4739 (2000).

[162] D. A. Butler, B. E. Hayden, and J. D. Jones, Precursor dynamics in dissociative hydrogen adsorption on W(100), Chem. Phys. Lett. 217, 423 (1994).

- [163] A. Rar and T. Matsushima, Desorption and dissociation of oxygen ad-molecules on a stepped platinum (533) surface, J. Chem. Phys. 103, 6217 (1995).
- [164] M. Valden, N. Xiang, J. Pere, and M. Pessa, Dissociative chemisorption of methane on clean and oxygen precovered Pt(111), Appl. Surf. Sci. 99, 83 (1996).
- [165] M. Valden, N. Xiang, J. Pere, and M. Pessa, Influence of preadsorbed oxygen on activated chemisorption of methane on Pd(110), Chem. Phys. Lett. 257, 289 (1996).
- [166] J. Harris, J. Simon, A. C. Luntz, C. B. Mullins, and C. T. Rettner, *Thermally assisted tunneling: CH*₄ dissociation on Pt(111), Phys. Rev. Lett. 67, 652 (1991).
- [167] G. R. Schoofs, C. R. Arumainayagam, M. C. McMaster, and R. J. Madix, *Dissociative chemisorption of methane on Pt(111)*, Surf. Sci. **215**, 1 (1989).
- [168] H. A. Michelsen and D. J. Auerbach, A critical examination of data on the dissociative adsorption and associative desorption of hydrogen at copper surfaces, J. Chem. Phys. 94, 7502 (1991).
- [169] G. J. Kroes, E. J. Baerends, and R. C. Mowrey, Six-dimensional quantum dynamics of dissociative chemisorption of H₂ on Cu(100), J. Chem. Phys. 107, 3309 (1997).
- [170] G. J. Kroes, E. J. Baerends, and R. C. Mowrey, Six-dimensional quantum dynamics of dissociative chemisorption of (μ=0, j=0) H₂ on Cu(100), Phys. Rev. Lett. **78**, 3583 (1997).
- [171] K. D. Rendulic and A. Winkler, Adsorption and desorption dynamics as seen through molecular beam techniques, Surf. Sci. 299/300, 261 (1994).
- [172] W. Van Willigen, Angular distribution of hydrogen molecules desorbed from metal surfaces, Phys. Lett. A 28, 80 (1968).
- [173] K. Klier, S. H. Hess, and R. G. Herman, Structure sensitivity of methane dissociation on palladium single crystal surfaces, J. Chem. Phys. 107, 4033 (1997).
- [174] Y. N. Wang, R. McAllister, R. G. Herman, G. W. Simmons, and K. Klier, *Design and construction of a simple UHV-compatible high-pressure reaction cell*, Rev. Sci. Instrum. **63**, 5767 (1992).
- [175] Y. N. Wang, R. G. Herman, and K. Klier, Dissociative adsorption of methane on Pd(679) surface, Surf. Sci. 279, 33 (1992).
- [176] A. C. Luntz and J. Harris, *CH*₄ dissociation on metals: A quantum dynamics model, Surf. Sci. **258**, 397 (1991).
- [177] M. Hand and J. Harris, Recoil effects in surface dissociation, J. Chem. Phys. 92, 7610 (1992).
- [178] V.A. Ukraintsev and I. Harris, A statistical model for activated dissociative adsorption: Application to methane on Pt(111), J. Chem. Phys. 101, 1564 (1994).
- [179] A. T. Pasteur, St. J. Dixon-Warren, Q. Ge, and D. A. King, *Dynamics of hydrogen dissociation on Pt(100): Steering, screening and thermal roughening effects*, J. Chem. Phys. **106**, 8896 (1997).
- [180] A. C. Luntz and J. Harris, *C–H* bond activation on metals: A quantum dynamics model of direct and precursor mediated dissocation, J. Vac. Sci. Technol. **10**, 2292 (1992).
- [181] A. C. Luntz, CH₄ dissociation on Ni(100): Comparison of a direct dynamical model to molecular beam experiments, J. Chem. Phys. 102, 8264 (1995).
- [182] M.-N. Carré and B. Jackson, Dissociative chemisorption of CH₄ on Ni: The role of molecular orientation, J. Chem. Phys. 108, 3722 (1998).
- [183] H. B. Lyon and G. A. Somorjai, Surface Debye temperatures of the (100), (111) and (110) faces of platinum, J. Chem. Phys. 67, 3707 (1966).
- [184] R. Feder, H. Pleyer, P. Bauer, and N. Muller, *Spin polarization in low-energy electron diffraction:* Surface analysis of Pt(111), Surf. Sci. 109, 419 (1981).

Summary

Insight into the microscopic details of an elementary step of a surface reaction is extremely important for obtaining a complete understanding of a heterogeneous catalytic reaction. In order to describe the complete process, experimentalists as well as theoreticians are forced to simplify realistic reaction conditions to reduce the amount of relevant parameters due to the complexity of heterogeneous catalytic reactions. Consequently, both types of researchers are forced to work on idealized model systems which are single crystalline surfaces prepared in UHV in the case of experimental studies or metal slabs/clusters of limited dimensions for theoretical work.

Despite these simplifications the remaining model system still remains extremely complex because in a surface reaction many atoms are involved in the overall interaction. In addition, the reaction process requires a dynamic description because reactants move along the reaction coordinate to form the product. On a more abstract basis, surface reactions can be understood as movements of molecules or molecular fragments on the potential energy surface (PES), which describes all molecule–surface interactions and all inter–atomic interactions within the molecules. The knowledge of the PES is of extreme importance because a full understanding of the PES allows the prediction of surface reactions. Unfortunately, it is not always possible to reach such a detailed description because of the many degrees of freedom involved in the process. However, a less detailed but very instructive empirical PES can be constructed if certain dynamic interactions are known.

This thesis illustrates that from experimental results and 'static' theoretical calculations many properties of the PES can be derived which give insight into the microscopic details of reaction mechanisms.

To elucidate this a simple model system has been chosen, namely the CO interaction with a hydrogen saturated Ru(0001) surface of which the dynamics and thermodynamics have been studied. DFT calculation of this system reveal that CO adsorption within the $(1 \times 1)H$ overlayer is only possible on the atop position as evident from the computed adsorption energies. In contrast, on the bare Ru(0001) surface all available adsorption sites exhibit a strong attractive interaction leading to a deep chemisorption well over the whole unit cell. Experiments using molecular beam techniques show that CO adsorption on the hydrogen saturated surface is negligible at low incident energies (below 0.25 eV) and the surface is almost completely passivated for CO adsorption. However, increasing the translational energy of the CO molecules substantially enhances the initial chemisorption probability. The sticking versus energy curve is consistent with a direct activated process with a minimum activation energy of 0.25 eV. This barrier height could be confirmed theoretically by applying the 'nudged elastic band' method [61-63] to this system. By means of density of states calculations the origin of the barrier could be determined and at-

112 Summary

tributed to Pauli repulsion which initially prevails on the approach of the CO molecule to the surface. Contrary to theory, an experimentally prepared $Ru(0001)(1\times1)H$ surface exhibits an additional non–activated reaction channel which can be attributed to CO adsorption at defects or vacancies of the hydrogen overlayer. This is described in Chapter 2.

Applying molecular beam techniques to the $CO/Ru(0001)(1\times1)H$ system, important information on the properties of the PES can also be gained from the CO molecules which are scattered. These molecules represent the fraction of molecules where the repulsive part of the interaction prevails. On the bare Ru(0001) surface the attractive forces dominate which manifest themselves in the high sticking probability over the whole energy range. The adsorption is clearly non–activated. Energy transfer and angular distribution of CO scattered at grazing incidence suggest that the repulsive O–end interaction creates a reaction channel which allows the molecules to escape the strong attractive forces. The partial passivation of the unit cell of the $Ru(0001)(1\times1)H$ surface results in very narrow angular distributions with CO scattered mainly in the specular direction. Energy transfer measurements for various incident energies show that very little energy transfer is present, indicating trajectories with a classical turning point which lies far away from the surface plane. Together with the angular distribution the properties of the repulsive part of the PES resemble an almost perfect *molecular mirror*. This is described in Chapter 3.

Chapter 4 deals with the consequence of the surface passivation on the coadsorption process of CO on the hydrogen saturated Ru(0001) surface. Due to the stronger CO–Ru interaction, it is found that CO displaces hydrogen. Furthermore, the CO coverage build–up triggers an increase in the CO uptake efficiency. Thereby, small 'magic–size' islands are initially formed consisting of 7 molecules which act as precursors for gas–phase CO adsorption. Depending on the incident flux these islands grow rapidly to become stable, large islands or simply keep their size by detaching the energetically less favorable 8th molecule for the island and releasing it into the hydrogen overlayer. This process is slow compared to the CO diffusion indicating an activation barrier for CO detachment.

In Chapter 5 a new UHV-apparatus is introduced, which has been developed to investigate dynamic processes on surfaces within a broad scope of experimental techniques. For this purpose, an existing UHV-apparatus has been equipped with a three-stage molecular beam line which can operate under aggressive chemical conditions. By means of three individually operating nozzles, exposure sequences with different reactive gases can be accomplished within a short time interval. The design has been chosen such that the experiment is compatible with the requirements of a modern laser-laboratory. Besides standard UHV-techniques, the main chamber is equipped with viewports allowing the surface to be irradiated with laser light. The geometry of surface and viewports has been chosen such that the time of flight facilities of the molecular beam can be used for laser induced desorption or photochemcial experiments. In combination with the already existing surface techniques (TDS, XPS, LEED and RAIRS) detailed information on the dynamics of surface reactions can thus be gained in the future.

Chapter 6 reports about the dissociative adsorption of methane on a stepped platinum surface. The (100)–steps offer a low energetic route to dissociation. At translational energies above 800 meV the step activity appears to saturate indicated by a constant dissociation probability. However, the total activity of the Pt(533) surface increases with additional translational energy as the dissociation channel on the (111)–terraces starts to open up. The trends of both reaction channels are in agreement with a direct mechanism. The majority of the energy necessary to cleave the chemical bond has to be provided from the gas–phase.

Zusammenfassung

Detailliertes Wissen über die Mechanismen von Elementarreaktionen auf Oberflächen liefert einen wichtigen Beitrag zum allgemeinen Verständnis der heterogenen Katalyse. Da reale Prozesse äußerst kompliziert sind, wird in der Wissenschaft an Modellsystemen gearbeitet. Das können zum Beispiel einkristalline Oberflächen im Falle von experimentellen Studien oder Berechnungen an Clustern oder 'slabs' sein. Diese Vereinfachungen sind unumgänglich, um die große Anzahl der Freiheitsgrade eines realen Systems zu reduzieren. Trotz dieser weitreichenden Vereinfachungen bleiben die Modellsysteme meistens sehr kompliziert, da zu einer vollständigen Beschreibung einer Oberflächenreaktion die Wechselwirkungen aller Atome sowohl die der Oberfläche als auch die der Reaktanden und Produkte berücksichtigt werden müssen. Darüber hinaus muss der eigentliche Prozess der Reaktion als dynamisch angesehen werden, da sich die Moleküle oder Molekülfragmente entlang der Reaktionskoordinate bewegen.

Abstrahiert kann eine Oberflächenreaktion als eine Bewegung von Molekülen und Molekülfragmenten auf der Hyperfläche der potentiellen Energie (HPE) betrachtet werden, die alle Molekül–Oberflächenwechselwirkungen und interatomaren Wechselwirkungen der Adsorbatmoleküle beschreibt. Ist diese bekannt, kann man Reaktionen oder Prozesse an Oberflächen vorhersagen. Um einer bestimmten Reaktion einen Mechanismus zuordnen zu können, muss die Dynamik der Reaktion berücksichtigt werden. Die vielen Freiheitsgrade, die in einer Oberflächenreaktion involviert sind, führen dazu, dass selbst bei einem einfachen Elementarschritt einer Reaktion oft mehrere Mechanismen beteiligt sind. Die energetischen Ausgangszustände der Reaktanden und der Oberfläche bestimmen deshalb, welcher Mechanismus überwiegt.

Im Rahmen der vorliegenden Dissertation wurde gezeigt, dass man mit Hilfe von experimentellen Ergebnissen und quantenmechanischen Berechnungen viele Eigenschaften der Energie-Hyperfläche ableiten kann, die Einblicke in die mikroskopischen Vorgänge einer Oberflächenreaktion geben.

Dies wurde mithilfe eines einfachen Modellsystems verdeutlicht: der dynamischen Wechselwirkung von CO mit einer reinen und wasserstoffgesättigten Ru(0001)-Oberfläche. Mittels quantenmechanischer Berechnungen konnte anhand der Adsorptionsenergien gezeigt werden, dass CO innerhalb einer (1×1)H–Überstruktur nur in der on–top–Position adsorbieren kann. Im Gegensatz dazu variiert die Adsorptionsenergie auf der reinen Rutheniumoberfläche nur wenig mit dem CO–Adsorptionsplatz. Vergleicht man die Werte der Adsorptionsenergien der H-bedeckten und der reinen Ru–Oberflächen, zeigt sich, dass der koadsorbierte Wasserstoff die CO–Ru-Bindung drastisch schwächt. Dieser Effekt resultiert aus der Tatsache, dass im Falle des Koadsorptionssystems CO und H um die attraktive Wechselwirkung mit den Ru–Atomen konkurrieren.

114 Zusammenfassung

Die Dynamik des CO-Adsorptionsprozesses auf den beiden Oberflächen wurde experimentell untersucht. Mittels der Molekularstrahltechnik konnten CO-Moleküle mit einer definierten und variablen kinetischen Energie präpariert und unter einem bestimmten Winkel den Oberflächen ausgesetzt werden. Die Messungen zeigten, dass auf der reinen Ru(0001)-Oberfläche CO ohne Energieaufwand adsorbiert. Im Gegensatz dazu erfordert die Adsorption innerhalb der (1×1) H-Überstruktur eine minimale Translationsenergie von 0.25 eV. Mittels theoretischer Berechnungen konnte nachgewiesen werden, dass diese Energiebarriere auf Pauli-Repulsion zurückzuführen ist, die beim Annähern des CO-Moleküls an die Oberfläche zunächst überwiegt. Des Weiteren konnte auf einer experimentell präparierten Ru(0001)(1×1)H-Oberfläche ein weiterer nichtaktivierter Reaktionsmechanismus gefunden werden. Dieser Mechanismus ist auf CO Adsorption an strukturellen Defekten innerhalb der (1×1) H-Lage zurückzuführen.

Interessante Informationen über die Beschaffenheit der HPE sind aus den Eigenschaften der gestreuten CO-Moleküle zu entnehmen. Diese Moleküle repräsentieren den Anteil der CO-Moleküle, die sich der starken attraktiven Anziehung des Chemisorptionspotentials entziehen können. Während auf der reinen Oberfläche beinahe alle CO-Moleküle haften, wird auf der Hbedeckten der Hauptanteil der auftreffenden Moleküle reflektiert. Obwohl Berechnungen zeigten, dass die O-Wechselwirkung des CO-Moleküls mit den Ru-Atomen repulsiv ist, blieben auf der Ru(0001) bei niedrigen kinetischen Energien über 95% der CO-Moleküle haften. Die hohe Haftwahrscheinlichkeit hat ihre Ursache darin, dass die niederenergetischen Moleküle relativ einfach ihre Orientierung verändern können, da sie genügend Zeit innerhalb des attraktiven Potentials verbringen. Bei hohen Energien dagegen wird die Wechselwirkungszeit kürzer und ungefähr 20% der Moleküle werden reflektiert. Die Winkelverteilungen der gestreuten Teilchen und der gemessene Energieaustausch mit der Ru(0001)-Oberfläche legen nahe, dass diese gestreuten Moleküle auf dynamische Wechselwirkungen mit der O-Seite des Moleküls zurückzuführen sind. Die starke Anziehungskraft des Chemisorptionspotentials der Ru(0001)-Oberfläche führt dazu, dass der klassische Wendepunkt des CO-Moleküls dichter bei den Kernen der Metallatome liegt als bei Systemen ohne oder mit nur schwacher attraktiver Wechselwirkung. Dadurch erscheint die Oberfläche lateral geriffelt. Durch den adsorbierten Wasserstoff wird der Effekt der lateralen Riffelung ausgelöscht und die Oberfläche agiert nahezu wie ein molekularer Spiegel. Es ließ sich feststellen, dass dieser Effekt auf der Verlagerung des klassischen Wendepunkts, verursacht durch die Pauli-Repulsion, beruht.

Die repulsive H–CO-Wechselwirkung wirkt sich auch auf die laterale Ordnung der CO–H-Koadsorption aus. Bei höheren Oberflächentemperaturen (250 K) führt die CO Adsorption zu Wasserstoffdesorption. Gleichzeitig bilden sich innerhalb der H–Überstruktur kleine CO-Inseln, die aus sieben CO–Molekülen bestehen. Das Wachstum dieser Inseln kann allein über einen Zusammenstoß eines CO–Gasphasenmoleküls mit einer Insel erfolgen. Dieses zusätzliche CO–Molekül führt zu eine Destabilisation der Insel zur Folge, da die hexagonale Symmetrie gestört wird und ein langsamer 2D–Verdampfungsprozess einsetzt. Dadurch wird die Ordnung auf der Oberfläche abhängig vom CO–Teilchenstrom. Während bei niedrigem Teilchenstrom die Verdampfung überwiegt und die Anzahl der Inseln zunimmt, enstehen bei hohem Teilchenstrom große Inseln bei konstanter Inseldichte.

Die experimentelle Charakterisierung von Reaktionen an Oberflächen erfordert einen beträchtlichen technischen Aufwand. Die Kompliziertheit der dynamischen Prozesse auf Oberflächen macht eine genaue Charakterisierung der Ausgangs-, Zwischen- und Endzustände notwendig. Es ist daher sinnvoll, viele Oberflächenmethoden zu kombinieren, um interessante

ZUSAMMENFASSUNG 115

Reaktionen unter verschiedenen Aspekten untersuchen zu können. Deshalb wurde ein bereits bestehendes UHV-System mit einer Molekularstrahlapparatur ausgerüstet, die speziell entwickelt wurde, um unter aggressiven chemischen Bedingungen arbeiten zu können. Speziell dazu wurde ein Halter für drei Düsen mit individuellem Gaseinlasssystem entworfen. Dadurch können Oberflächen innerhalb kürzester Zeit verschiedenen, reaktiven Gasen ausgesetzt werden. Darüber hinaus wurde die Molekularstrahlapparatur so entworfen, dass sie den Anforderungen eines modernen Laserlabors genügt.

Während man mit der Molekularstrahltechnik ausgezeichnet die Dynamik einer Gasphasen-Oberflächenreaktion untersuchen und daraus indirekt Rückschlüsse auf den eigentlichen Reaktionsmechanismus ziehen kann, ist man mit modernen Femtosekundenlaser in der Lage, einer Oberflächenreaktion zeitaufgelöst zu folgen. Die Kombination von Femtosekundenlaser- und Molekularstrahltechnik eröffnet neue Möglichkeiten, die dynamischen Abläufe von Oberflächenreaktionen in der Zukunft noch detaillierter zu untersuchen.

Eine interessante Oberflächenreaktion ist die dissoziative Adsorption von Methan an Übergangsmetalloberflächen. Dieser Prozess ist kinetisch gehemmt, da zur Spaltung der ersten C-H-Bindungen eine hohe Aktivierungsenergie aufgewendet werden muss. Auf den meisten Übergangsmetalloberflächen überwiegt ein 'direkter' Reaktionsmechanismus, bei dem die C-H-Bindung beim Zusammenstoß des Moleküls mit der Oberfläche gespalten wird. Deshalb ist bei diesem Mechanismus hauptsächlich die Gasphasen-Energie (Translations- und Schwingungsenergie) des Moleküls für die dissoziative Adsorption verantwortlich.

In der vorliegenden Arbeit wurde der Einfluss von definierten Oberflächendefekten auf die Dissoziationswahrscheinlichkeit untersucht. Dazu wurde eine Pt(533) einkristalline Oberfläche verwendet. Diese Oberfläche besteht aus (111)-Terrassen (vier Atome lang) und (100)-Stufen (ein Atom lang). Es konnte anhand eines einfachen geometrischen Modells gezeigt werden, dass die Gesamtaktivität der Oberfläche als Summe von Terrassen- und Stufenaktivität beschrieben werden kann. Des Weiteren erfordert die Dissoziation an Stufen eine deutlich geringere Aktivierungsenergie. Die Energie- und Temperaturabhängigkeit der Dissoziationswahrscheinlichkeit der Stufen weist auf einen direkten Reaktionsmechanismus hin.

Nawoord

De resultaten die in dit proefschrift worden beschreven zouden niet tot stand zijn gekomen zonder de hulp van veel mensen.

Het doen van experimenteel onderzoek betekent worstelen met de apparatuur. De technische ondersteuning van François Giskes was onmisbaar bij het opbouwen en draaiend houden van de opstellingen. Bovendien dacht hij altijd actief mee over de technische problemen die onderweg opdoken. Het ontwerp van de moleculaire bundel heeft vorm gekregen tijdens uitvoerige discussies in de tekenkamers van AMOLF en NIKHEF. De vele ideeën zijn op uitstekende wijze uitgewerkt door Dick Glastra van Loon en Piet Lassing. Aan de hand van de ontwerpen uit de tekenkamer heeft de mechanische werkplaats de lastige onderdelen van de apparatuur gemaakt. Ik ben zeer onder de indruk van de vakkundigheid van de intrumentmakers, onder wie Wim Brouwer, Henk Neerings, Jan van der Linden, Christiaan Pen, Wim Barsingerhoorn, Ruud Boddenberg en Menno Borsboom. Als we plotseling weer iets wilden veranderen of laten repareren, stonden ze steeds voor ons klaar. Dit geldt ook voor de mensen bij de afdeling electronica en informatica. In het bijzonder Hans Alberda, Idsart Attema, Hans der Horst, Jan van der Elst, Richard Schaafsma en Ben Okhuysen. René Koper heeft de kristallen nodig voor dit onderzoek uitstekend geprepareerd.

Jürgen Chrost heeft mij er met zijn enorme kennis over UHV-apparatuuren en kritische houding meerdere keren toe aangezet om delen van het ontwerp nog maar eens te overdenken en vaak de goede tip voor de juiste oplossing van een experimenteel problem gegeven. Met Ionel Ciobîcă en de theorie groep uit Eindhoven heb ik zeer prettig mogen samenwerken. Zonder de groep verliest veel onderzoek zijn glans. Ik heb plezierig samengewerkt met: Bart Berenbak, Dimitrios Papageorgopoulos, Heiner Scheld, Mischa Bonn, Mike Gleeson, Martijn Verwoest, Silvie Roke en Sander Zaboray.

Voor de goede sfeer zowel binnen als buiten AMOLF wil ik ook graag noemen: Han, Ille, Wim, Astrid, Marcel, Katja, Andrea, Ricarda, Kai, Steven, Frederik, Arjan, Han Kwang, Michel, Martin, Rainer, Frank, Marco en Jenny.

Tenslotte wil ik Anja en mijn ouders bedanken voor hun onvoorwaardelijke steun tijdens mijn promitieonderzoek en het schrijven van dit proefschrift.

Curriculum Vitae

Op 19 januari 1971 ben ik geboren in de stad Laupheim in Duitsland. In 1990 heb ik het eindexamen behaald aan het Karl Lämmle Gymnasium in Laupheim. Tussen juli 1990 en juni 1991 deed ik mijn dienstplicht. Vervolgens ben ik begonnen aan de studie scheikunde aan de Universiteit van Ulm in Duitsland. Het afstudeerwerk is door mij uitgevoerd op het Shell Research and Technology Center in Amsterdam. Hier heb ik onder begleiding van Dr. Gert-Jan Kramer model katalysatoren bestudeerd met behulp van 'polarisation modulated reflection adsorption infrared spectroscopy'. In september 1996 ben ik op dit onderwerp afgestudeerd. In december 1996 ben ik als onderzoeker in opleiding (OIO) begonnen bij het FOM–Instituut voor Atoomen Molecuulfysica. In de groep Moleculaire bundels heb ik gewerkt onder supervisie van prof. dr. A. W. Kleyn. Het theoretische werk beschreven in dit proefschrift is tot stand gekomen onder supervisie van prof. dr. R. A. van Santen. De resultaten van het onderzoek staan beschreven in dit proefschrift.

120 Notes

